Project No. 13-4761

Off-Gas Treatment: Evaluation of Nano-structured Sorbents for Selective Removal of Contaminants

Fuel Cycle Research and Development

Vivek Utgikar
University of Idaho

Jim Bresee, Federal POC
Bob Jubin, Technical POC

Final Report

Project Title:	Off-Gas Treatment: Evaluation of Nano-structured Sorbents for Selective Removal of Contaminants
Date of Report:	March 30, 2018
Milestone Level:	2
Recipient:	University of Idaho Office of Sponsored Programs P.O. Box 443020 Moscow ID 83844
Award Number:	DE-NE0000660
Project Number:	13-4761
Project Period:	January 1, 2014 – December 31, 2017
Principal: Investigator	Utgikar, Vivek 208-885-6970 vutgikar@uidaho.edu
Collaborators:	D. Eric Aston (University of Idaho) 208-885-6953 aston@uidaho.edu Sabharwall, Piyush (Idaho National Laboratory) 208-526-6494 piyush.sabharwall@inl.gov
TPOC	Robert Jubin
Federal Manager	Jim Bresee
Workscope	FC-6.5

Executive Summary

Goals, Objectives, and Approach

The goal of the proposed research was to evaluate nanostructured sorbent materials for their effectiveness in removing and immobilizing the contaminants of interest for the off-gas treatment from the UNF recycling operations. Specific objectives defined for the research are:

1. To synthesize and characterize various nanosorbents for the removal of radioactive contaminants from the off-gas,
2. To determine the adsorption isotherms for contaminants of interest (I, Kr) on selected sorbents,
3. To investigate the immobilization of the contaminants in a durable form, and
4. To develop a process model that can be used for the design of the capture and immobilization system for the radionuclides in the off-gas.

Nanostructured sorbents were synthesized in the laboratory and their surface and structural characteristics determined by various instrumental and analytical techniques. Continuous column dynamic sorption experiments were conducted using surrogate off-gas streams containing single contaminant and multiple contaminant mixtures at various experimental conditions. Experimental work was conducted to develop matrix that would be suitable for entrapping the sorbed contaminants for immobilization and isolation from the environment. Comprehensive system model was developed by combining the sorption models with transport models through the contactor.

Accomplishments and Outcomes

The summary of these activities conducted and the resulting outcomes is as follows:

- Low temperature synthesis of hollow carbon nano-polyhedron was effected using $NiCl_2.6H_2O$ and CaC_2 as raw materials. Engelhard Titanosilicate number 10, known as ETS-10, was synthesized by a hydrothermal method. Two different titanium precursors – $TiCl_3$ and TiO_2 – were investigated. Hollow carbon nano-polyhedrons (HCNPHs) supported on Engelhard Titanosilicate-10, ETS-10 were synthesized by wet impregnation method using tetrahydrofluron (THF) as a solvent.

- Optimized 10 wt% C@ETS-10 (carbon immobilized on ETS-10 support matrix at loading of 10 wt%) sorbent for the removal of contaminates (Kr and I_2) and its components – HCNPHs and ETS-10 – were characterized by scanning electron microscopy (SEM) and transmission electron microscopy (TEM) to identify the morphology of the sorbents. Qualitative elemental analysis of sorbent was carried out by scanning electron microscopy-energy dispersive spectroscopy (SEM-EDS). The structures of the sorbents were determined by X-ray diffraction (XRD) and Raman spectroscopy. The surface area and pore size distribution of sorbent were determined using a Brunauer-Emmett-Teller (BET) analyzer. Used C@ETS-10 pellets loaded with iodine after the sorption experiments were also characterized using SEM-EDS, XRD and thermogravimetric analysis (TGA).
- Adsorption of individual components (Kr and I_2) was studied on newly developed sorbent C@ETS-10 through dynamic sorption experiments in a continuous column apparatus. The capacity of sorbent was separately investigated for krypton and elemental iodine using nonradioactive isotopes. Krypton removal was studied as a function of the carbon loading and the temperature of adsorption column. The capacities of the new sorbent for krypton were compared with the adsorption capacity of coconut-derived activated carbon. Iodine removal capacity of C@ETS sorbent was optimized as a function of the operating temperature, and sorbent bed height.
- The continuous column single component sorption experimental setup was modified for conducting experiments on multicomponent systems. Dynamic sorption experiments were conducted using the modified experimental apparatus to determine the sorption capacity of 10 wt% C@ETS-10 for multicomponent gas stream containing iodine and krypton at ambient temperature and pressure. The capacity of sorbent was examined varying different parameters such as inlet concentrations, temperatures and effect of iodine on Kr sorption and vice versa. Pristine and used 10 wt% C@ETS-10 sorbent were characterized by SEM-EDS, Raman spectra, and TGA.
- Moisture was added to a multicomponent (25 ppm iodine, 70 ppm krypton) gas stream at varying relative humidity values. Its effects of the sorption capacity of iodine and krypton were measured.

- Experimental investigations were conducted to entrap the contaminants captured through sorption in an inert matrix for immobilization and isolation from the environment. Initial attempts at developing the matrix were based on fashioning a ceramic sleeve of powdered celite material and coating it with pyrolytic carbon and silicon carbide. However, the resulting container was porous and lacking structural strength.
- Commercially available alumina tube with low porosity and rigidity were used in subsequent investigations. The base alumina material was first coated with carbon using a carbon source (tire shreds), and kaolin which functioned as a catalyst. The carbon-coated alumina tube was subjected to further coating of silicon carbide in a high temperature furnace. The coated substrates were characterized through electron microscopy.
- It was found that the alumina substrate could be coated rather easily with carbon. Subsequent coating with SiC requires a careful control over the processing conditions. It is possible to obtain an impervious double layered matrix that has structural strength and inertness. Such container can be used to hold the contaminant laden sorbent – nanostructured carbon supported on Engelhard Titanosilicate-10 used in our study – to isolate it from the environment. This approach holds much promise and merits further research due to its potential advantages over the metallic containers traditionally considered for isolation.
- The sorbate-sorbent equilibrium relationships were described using Langmuir and Freundlich adsorption isotherms.
- Two different approaches were used for describing the kinetics of the sorption process. First, three different literature-reported models were examined for their applicability to the system under consideration; secondly, a fundamental mass transport model was developed with a first-order sorption kinetics of the contaminant in the off-gas stream that has the flow characteristics of plug flow with dispersion.
- Model simulations were conducted by developing custom-coded MATLAB programs. Data obtained from the dynamic sorption experiments were used to obtain the model parameters and validate/verify the models.

- It was found that:
    - Langmuir adsorption isotherm was better suited for describing the equilibrium relationships of iodine and krypton on the sorbent nanostructured carbon supported on Engelhard Titanosilitcate-10.
    - Literature reported kinetic models – the Thomas model, the Yoon-Nelson model, and the Adams-Bohart model – could not explain the data entirely satisfactorily. The mass transport model based on fundamental principles has greater utility for the describing the process accurately.
- An approach for scale-up and design based on the mass transfer zone (MTZ) of fixed bed adsorbers was developed presented. A combination of the fundamental mass transport model and the MTZ approach will be valuable for the design of the integrated treatment system.
- Recommendations for future work to obtain the relevant parameters and validate the models by conducting experimental investigations on a larger-scale system are presented.

Refereed Journal Publications

A) Published

1. Nandanwar SU, Coldsnow K, Porter A, Sabharwall P, Aston DE, McIlroy DN, Utgikar V. 2017. Adsorption of radioactive iodine and krypton from off-gas stream using continuous flow adsorption column. *Chemical Engineering Journal*, 320: 222-231, DOI: 10.1016/j.cej.2017.03.020.
2. Nandanwar S, Coldsnow K, Utgikar V, Sabharwall P, Aston DE. 2016. Capture of harmful radioactive contaminants from off-gas stream using porous solid sorbents for clean environment – A review. *Chemical Engineering Journal*, 306: 369-381, DOI 10.1016/j.cej.2016.07.073.
3. Nandanwar SU, Coldsnow K, Green M, Utgikar V, Sabharwall P, Aston DE. 2016. Activity of nanostructured C@ETS-10 sorbent for capture of volatile radioactive iodine from gas stream. *Chemical Engineering Journal*, 287: 593-601. DOI 10.1016/j.cej.2015.11.091.
4. Nandanwar SU, Coldsnow K, Utgikar V, Sabharwall P, Aston DE, Zhang Y. 2016. Synthesis and characterization of ETS-10 - supported hollow carbon nano-polyhedrons

nanosorbent for adsorption of krypton at near ambient temperatures. *Adsorption*, 22: 129-137, DOI 10.1007/s10450-015-9702-8.

5. Nandanwar SU, Dantas J, Green M, Coldsnow K, Utgikar V, Sabharwall P, Aston DE. 2016. Porous microsphere magnesium oxide as an active sorbent for capture of volatile iodine. *Adsorption*, 22: 335-345, DOI 10.1007/s10450-016-9781-1.

B) In Progress

1. K Coldsnow, SU Nandanwar, V Utgikar, P Sabharwall. Modeling of Adsorption of Iodine and Krypton on Engelhard Titanosilicate-10 Supported Carbon Nano-Polyhedrons in a Continuous Column Adsorber. *(In preparation).*

Conference Papers and Presentations

1. "A Mass Transfer Model for the Adsorption of Iodine and Krypton on Engelhard Titanosilicate-10 Supported Carbon Nano-Polyhedrons," K Coldsnow, S Nandanwar, V Utgikar, P Saharwall, 2017 ANS Winter Meeting, October 29-November 2, 2017, Washington, DC, USA.
2. "Effect of Moisture on the Adsorption of Iodine and Krypton in Multicomponent Streams on the 10 wt% C@ETS-10 Sorbent," K Coldsnow, S Nandanwar, A Porter, V Utgikar, P Sabharwall, DE Aston, 2017 ANS Annual Meeting, June 11-15, 2017, San Francisco, CA, USA.
3. "Multicomponent Adsorption of Radioactive Iodine and Krypton using ETS-10 Supported Carbon Nano-Polyhedrons," K Coldsnow, SU Nandanwar, A Porter, V Utgikar, P Sabharwall, DE Aston, 2016 ANS Winter Meeting, November 6-10, 2016, Las Vegas, NV.
4. "Porous C@ETS-10 Sorbent for Capture of Krypton from Off-Gas Stream in Nuclear Power Plants," SU Nandanwar, K Coldsnow, VP Utgikar, P Sabharwall, DE Aston, 2016 International Congress on Advances in Nuclear Power Plants ICAPP 2016, April 2016, San Francisco, CA.
5. "Capacity of ETS-10 Supported Carbon Nanosorbent for Removal of Multicomponent from Off-Gas Stream," KM Coldsnow, SU Nandanwar, A Porter, VP Utgikar, P

Sabharwall, DE Aston, 2016 Annual meeting of the American Nuclear Society (ANS), June 2016, New Orleans, Louisiana.

6. "Adsorption of Volatile Iodine from Off-Gas Stream using ETS-10 Supported Hollow Carbon Nanosorbent," SU Nandanwar, K Coldsnow, M Green, V Utgikar, P Sabharwall, DE Aston, 2015 Winter meeting of the ANS, November 2015, Washington, DC.
7. "Krypton Removal from the Off-Gas Stream using the Hollow Carbon Based Nanosorbent," SU Nandanwar, V Utgikar, P Sabharwall, DE Aston, K Coldsnow, 2015 Annual Meeting of the ANS, June 2015, San Antonio, Texas.
8. "Off-Gas Treatment: Evaluation of Nano-structured Sorbents for Selective Removal of Contaminants," VP Utgikar, DE Aston, P Sabharwall, S Nandanwar, K Coldsnow, M Green, Materials Recovery and Waste Form Campaign Working Group Meeting, Savannah River National Laboratory, Aiken, South Carolina, February 2015.
9. "Treatment of Radioactive Contaminants in Off-Gases Using Carbon Supported ETS-10 Nanosorbent," SU Nandanwar, K Coldsnow, M Green, V Utgikar, P Sabharwall, E Aston, 2014 ANS Winter Meeting, November 2014, Anaheim, California.

Mentoring of Students/Researchers

1. Kai Coldsnow, M.S. (Major: Chemical Engineering), University of Idaho, Fall 2017. Thesis: *Capture of Radioactive Iodine and Krypton from Nuclear Off-Gas Streams with a Novel Sorbent*.
2. Sachin U. Nandanwar, Post-Doctoral Associate, May 2014 – December 2016.
3. Michael Green, B.S. (Major: Chemistry), University of Idaho, Spring 2016. Undergraduate research assistant.
4. Austin Porter, B.S. (Major: Chemical Engineering), Spring 2018 (Anticipated). Undergraduate research assistant.
5. Jarod Perko, B.S. (Major: Chemical Engineering), Spring 2019 (Anticipated). Undergraduate research assistant.
6. Saheed Adisa, M.S. (Major: Material Science and Engineering), Spring 2019 (Anticipated).
   Research Assistant

Table of Contents

List of Figures

List of Tables

ACRONYMS

C@ETS-10	Carbon immobilized on ETS-10 support matrix
CVD	Chemical vapor deposition
ETS-10	Engelhard titanosilicate-10
HCNPH	Hollow carbon nano-polyhedron
MFC	Mass flow controller
PyC	Pyrolytic carbon
RH	Relative humidity
UNF	Used nuclear fuel

Analytical Techniques

BET	Brunauer-Emmett-Teller surface area
EDS	Energy dispersive spectroscopy
FE-SEM	Field emission-scanning electron microscopy
SEM	Scanning electron microscopy
SEM-EDS	Scanning electron microscopy-Energy dispersive spectroscopy
TEM	Transmission electron microscopy
TGA	Thermogravimetric analysis
XPS	X-ray photoelectron spectroscopy
XRD	X-ray diffraction spectroscopy

REPORT NARRATIVE

1 Introduction

Nuclear energy has practically unlimited potential to satisfy world's energy needs for the foreseeable future. However, a comprehensive and reliable solution must be devised to address the key issues related to nuclear waste management in order to develop nuclear energy in a safe and responsible manner. Capture and immobilization of volatile radionuclides from nuclear operations is an essential component of an integrated nuclear waste management system. The majority of emissions occur during the treatment of the used nuclear fuel (UNF) as it is chopped and dissolved in the boiling nitric acid for subsequent extraction steps. The radionuclides contained in the off-gas include ^{129}I, ^{85}Kr, tritium (^{3}H) and ^{14}C.

Several alternative technologies have been investigated, with effective adsorption based processes holding the most potential for controlling these emissions, which is highly desirable for the development of the advanced fuel cycle. Proposed project is aimed at developing using a nanosorbent-based process for the capture and immobilization of the radionuclides of interest. The goals and specific objectives for the research are stated below.

1.1 Goals and Objectives

The goal of the proposed research is to evaluate nanostructured sorbent materials for their effectiveness in removing and immobilizing the contaminants of interest for the off-gas treatment from the UNF recycling operations. This evaluation will involve both laboratory sorption experiments and theoretical modeling of the processes. The specific objectives defined for the research are:

1. To synthesize and characterize various nanosorbents for the removal of radioactive contaminants from the off-gas,
2. To determine the adsorption isotherms for contaminants of interest (I, Kr) on selected sorbents,
3. To investigate the immobilization of the contaminants in a durable form, and
4. To develop a process model that can be used for the design of the capture and immobilization system for the radionuclides in the off-gas.

1.2 Research Approach and Methods

The objectives were accomplished through the execution of the tasks described below:

1. Synthesis and Characterization of the Sorbents: Nanostructured sorbents – primarily carbon and zeolite-based – were synthesized in the laboratory and the surface and structural characteristics of the sorbent determined by various instrumental and analytical techniques.
2. Determination of Adsorption Equilibria: The sorption characteristics of the sorbents were determined through continuous column experimentation. Experiments were conducted first with single contaminants and then with contaminant mixtures.
3. Development of Immobilization Strategy: Contaminants captured through sorption will be entrapped in the matrix for immobilization and isolation from the environment.
4. Development of Mathematical Models: Comprehensive system model was developed by combining the sorption models with transport models through the contactor.

The activities conducted and results obtained through the research are described in the following sections, with each section presenting details corresponding to each of the four tasks.

2 Synthesis and Characterization of Sorbents

2.1 Synthesis of Sorbent

2.1.1 Synthesis of hollow carbon nano-polyhedron

Low-temperature synthesis of hollow carbon nano-polyhedron was carried out following the procedure reported by Zhu et al. (2012). Precursors nickel dichloride hexahydrate (0.05 mol/6 g) and calcium carbide (0.218 mol/7 g) were autoclaved at 250 °C for 5 h. The autoclave was cooled naturally at atmospheric temperature. The product mixture separated into two immiscible layers that were separated. The lower layer was slightly hard and dark brown in color, and was washed with 0.1 N hydrochloric acid followed by deionized water. Mainly, it was contained the carbon and some amount of impurity. The upper layer was soft, light black, cotton-like in appearance and washed with deionized water only. Finally, the product (upper layer) was dried at 50 °C for 12 h and used for further processing. The schematic of the carbon synthesis procedure is shown in Figure 2.1.1.

2.1.2 Synthesis of ETS-10

Engelhard titanosilicate 10 (ETS-10) was synthesized by hydrothermal method by reaction between sodium silicate and a titanium source. Two different titanium sources were used: (1) $TiCl_3$ and (2) TiO_2.

Method 1 ($TiCl_3$ based): Following the procedure reported by Das et al. (1995), 63 g of sodium silicate solution (28.6% SiO_2, 8.82% Na_2O, 62.58% H_2O) was mixed with the 60 g of distilled water under vigorous stirring. NaOH solution (87 g of 11% solution) was added slowly into the above solution and the mixture stirred for 20 min. A 54.4 g of $TiCl_3$ (15% solution in HCl) was added drop wise into above mixture under stirring condition. The stirring was continued for 30 minutes and the color of the mixture turned from white to blackish. 9.4 g of $KF.2H_2O$ solution into a above mixture, which was further stirred for 60 min. Finally, 20 g of 21.5% NaCl solution was added slowly into the mixture. A homogeneous mixture having a pH of 11-11.3 was obtained upon further stirring vigorously for 60 minutes. The solution was autoclaved for 10 days at 200 °C. Crystallized solid product was removed from the mother liquor by filtration, washed twice with deionized water and dried overnight at 120 °C in oven.

Method 2 (TiO_2 based): Titanosilicate synthesis can also be effected by using TiO_2 as reported by Yang et al. (2001). 40 g of sodium silicate solution was diluted with the 70 g of distilled water, and a thick gel was obtained after the addition of 13.8 g NaCl and 2.6 g KCl to the solution. The gel was stirred vigorously for 20 min and 2.6 g of TiO_2 powder was added slowly to the mixture. After stirring the slurry for 45 minutes at room temperature. The mixture was autoclaved for static crystallization at 200 °C for 42 h. The product was washed with distilled water, filtered and dried at 120 °C in oven.

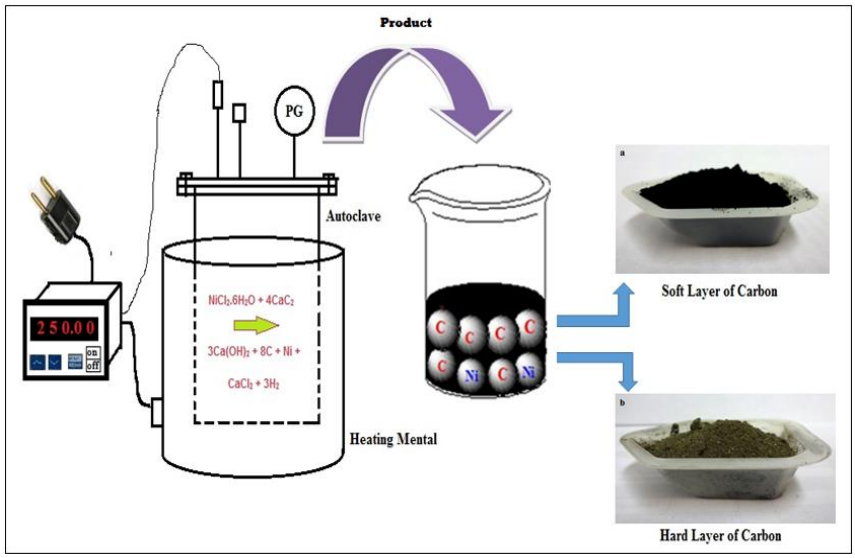

Figure 2.1.1: Schematic diagram for synthesis of carbon nanomaterials

2.1.3 Formulation of C@ETS-10 Nanosorbent by Wet Impregnation

C@ETS-10 nanosorbent (carbon immobilized on ETS-10 support matrix) was synthesized by transferring the carbon nanoparticles onto the ETS-10 support to maintain the homogeneous distribution. To increase the purity and introduces oxygenated functionalities of the surface, carbon nanomaterials were refluxed in concentrated nitric acid for 8 h under stirring. Then slurry was filtered; washed several times with distilled water and finally dried at 60 °C for 6 h in an oven. The wet impregnation method for preparing ETS-10 supported carbon involved adding 50 mg of carbon was added into 50 mL tetrahydrofloron (THF) and sonicating the mixture for 40 min to obtain a uniform dispersion. The effects of sonication can be seen from the before and after photos shown in Figure 2.1.2.

Appropriate quantity of the titaniumsilicate, ETS-10 was added under stirring into the dispersion to obtain the desired concentration of carbon (ranging from 3-20% wt% C) on ETS-10 nanosorbent. The mixture was mechanically stirred for 12 h; followed by vacuum filtration and

drying at room temperature. C@ETS-10 was pelletized with addition of 1.5 g of Ludox HS-40 colloidal silica into a 2 g powder sorbent. The mixture was homogenized, followed by compression in a pellet press for 5 min. The cake was crushed to make 3-10 mesh size pellets.

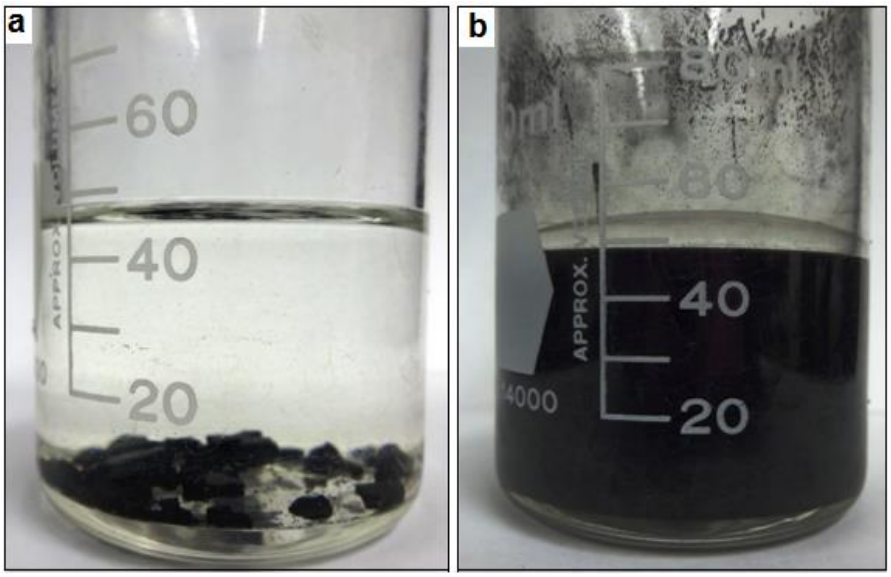

Figure 2.1.2: Carbon nanomaterials into the THF (a) before sonication (b) after 40 min sonication

2.2 Characterization of Virgin Sorbent

2.2.1 X-Ray Diffraction Analysis (XRD)

Figure 2.2.1a shows the powder X-ray diffraction patterns of the as-synthesized ETS-10, carbon and 10 wt% C@ETS-10 sorbent using a model Bruker D5000, Germany. ETS-10 was obtained by hydrothermal method under 200 °C for 42 h using TiO_2, as source of titanium. The resulting intensities of ten major peaks at 2θ = 5.9, 12.3, 20.1, 24.7, 25.8, 26.6, 29.9, 31.7, 35.6, and 45.5 matched well with reported literature (Anderson et al, 1994; Prasanth et al, 2010; Rocha et al, 1998; Yang et al, 2001). The two peaks of pure carbon was observed at 2θ = 25.3 and 43.5° represented the (002) and (101) planes of the hexagonal structure of the carbon (Zhu et al, 2012). For 10 wt % C@ETS-10 nanosorbent, a slight drop in intensity without formation of any new peak was observed which corresponded to the absence of any extensive formation of carbon over the ETS-10 framework. The carbon peak was not readily observed in the sample, possibly due to the low concentration of carbon (3wt%) on ETS-10, and the shielding of the main peak of carbon at 25.3º by the main peak of ETS-10. The characteristic peaks of carbon – at 2θ = 25.3 and 43.5º

of planes (002) and (101) for hexagonal carbon – were recovered by conducting the measurements at very slow scanning rate of carbon (Figure 2.2.1b).

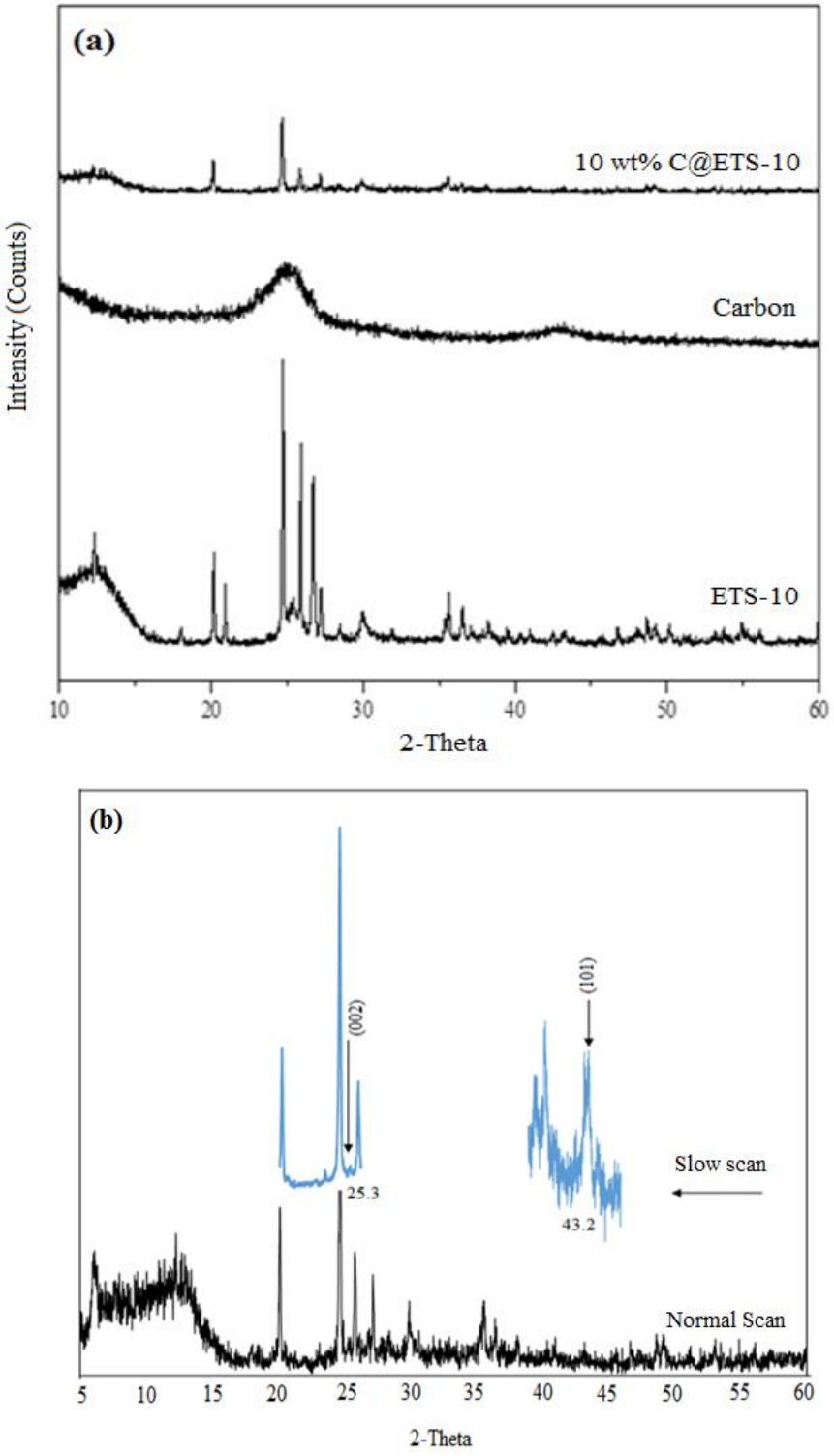

Figure 2.2.1: (a) XRD patterns of the samples of ETS-10, Carbon and 10 wt % C@ETS-10 nanosorbent (b) slow scan of 3 wt% C@ETS-10 sorbent

2.2.2 Raman spectra

Raman spectra of the products were measured by (WITec alpha300 Raman microscope, WITec, Ulm, Germany) to confirm the structure of the sorbent. Raman spectra of ETS-10 (synthesized using TiO_2), Carbon and 10 wt % C@ETS-10 nanosorbent are shown in Figure 2.2.2. The strongest band observed at 723 cm^{-1} in the spectrum could be attributed to the collective stretching vibration Ti-O-Ti of the TiO_6 structure group, which forms nanowires (Hong et al, 1996; Su et al, 2000). It was found that the occurrence of the peak at 723 cm^{-1} points to the degree of disorder in -Ti-O-Ti- chains. Weaker bands observed in the range of 300 – 400 cm^{-1} were slightly more difficult to interpret. Early literature attributes these to bending vibrations of the Si-O-Si, and Ti-O-Ti fragments near defects (Southon and Howe, 2002). One of the weak peaks observed at 636 cm^{-1}, might belong to the Ti-O-Ti stretching vibration in TiO_6 groups having a common face (Su et al, 2000). The structure of the carbon nanoparticles was confirmed by Raman spectra. Two sharp peaks were observed around at 1332 cm^{-1} and 1579 cm^{-1}. The peak at 1332 cm^{-1}, D band, was recognized as the defects and disorders in carbonaceous solid. The other peak centered at 1579 cm^{-1}, G band, was due to the stretching modes of C-C bonds of graphite (Robertson, 2002; Yang et al, 2001). Another intense peak was observed at 2690 cm^{-1}, which is known as the 2D, indicator for graphite (Dong et al, 2012). Raman spectra of 10 wt % C@ETS-10 confirmed that the hexagonal structure of carbon was supported on ETS-10 without any change in carbon and ETS-10 structure. The intensity of carbon and ETS-10 was very low due proper dispersion of carbon onto the surface of crystalline support, ETS-10.

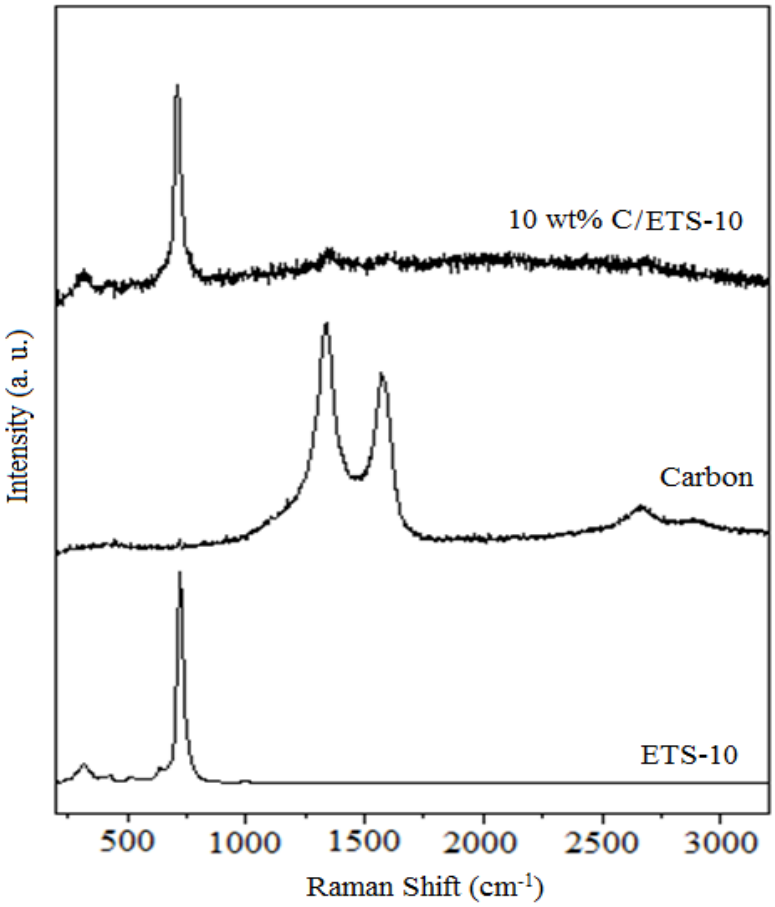

Figure 2.2.2: Raman spectra of samples of ETS-10, Carbon and 10 wt % C@ETS-10. The laser excitation wavelength was 532 nm

2.2.3 Scanning Electron Microscopy (SEM)

Figure 2.2.3 shows the surface morphology and size of the samples were analyzed using field emission-scanning electron microscopy (FE-SEM: LEO SUPRA 35VP). Hexagonal structured carbon particles were found to have a relatively uniform size in the range of 20-60 nm (Figure 2.2.3a). The morphology of ETS-10 (Figure 2.2.3b), indicates the formation of the typical truncated bipyramid crystals similar to those seen in earlier works (Rocha et al, 1998; Yang et al, 2001). Morphology of 10 wt% C@ETS-10 shows that hexagonal structure of carbon was well supported on to ETS-10 and covered maximum area of truncated bipyramid crystal (Figure 2.2.3c).

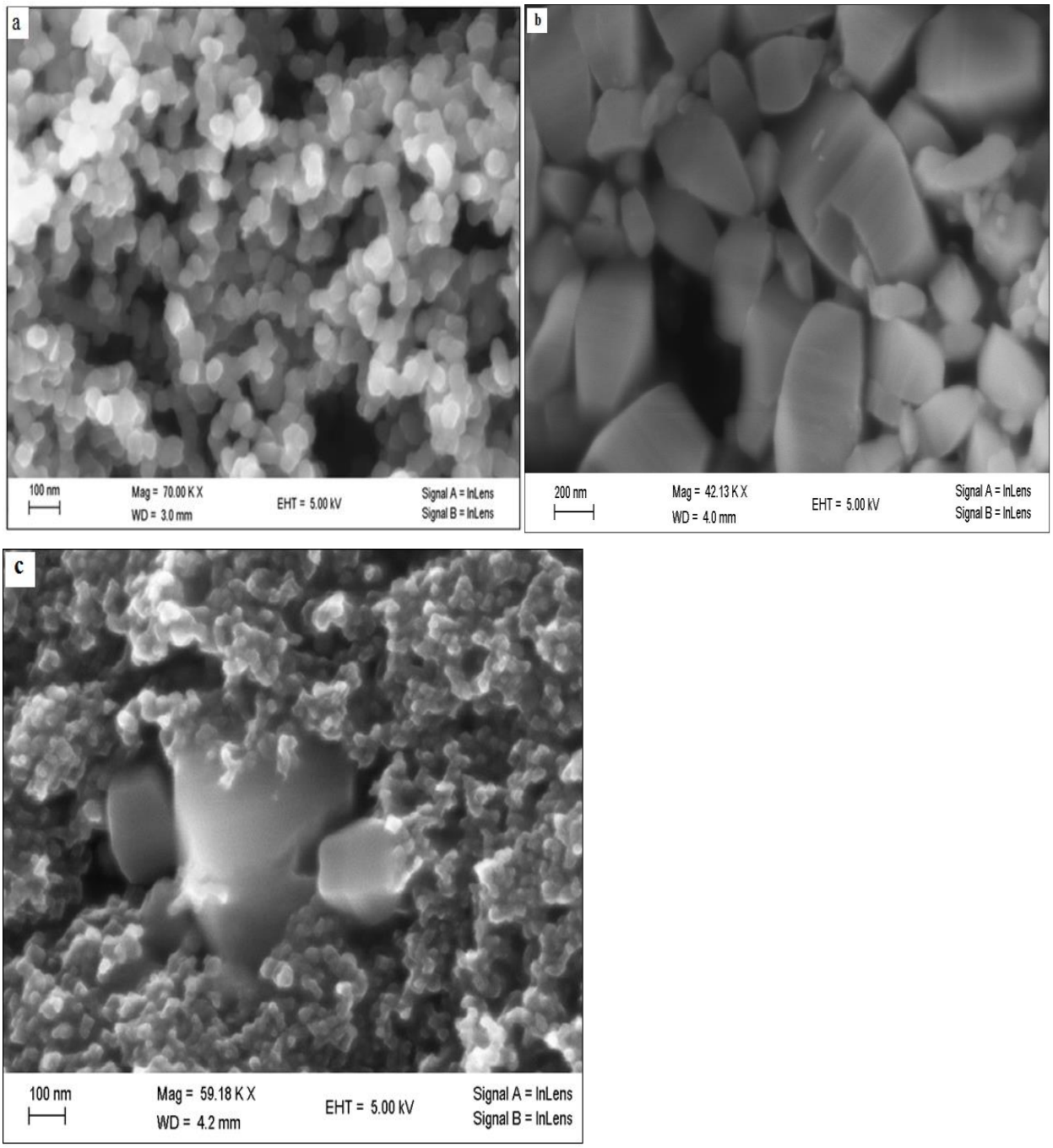

Figure 2.2.3: FE-SEM of (a) Carbon (b) ETS-10 (c) 10 wt % C@ETS-10

2.2.4 Scanning electron microscopy-Energy dispersive spectroscopy (SEM-EDS) of pellets

Figure 2.2.4 shows the FE-SEM image of fresh 10 wt % C@ETS-10 sorbent pellet with same instrument as mentioned above. It can be seen from Figure 2.2.4a that 10 wt % hollow carbon polyhedron nanoparticles cover the surface of ETS-10. The sample was dense due to pressing of the powder material during pellet preparation. Elemental composition of as-prepared fresh

adsorbent was analyzed by energy dispersive spectroscopy (EDS). The spectrum revealed abundance of all anticipated constituents such as C, Na, Si, Cl, K and Ti (Figure 2.2.4b). No other element was found in the fresh adsorbent indicating the high purity of the adsorbent.

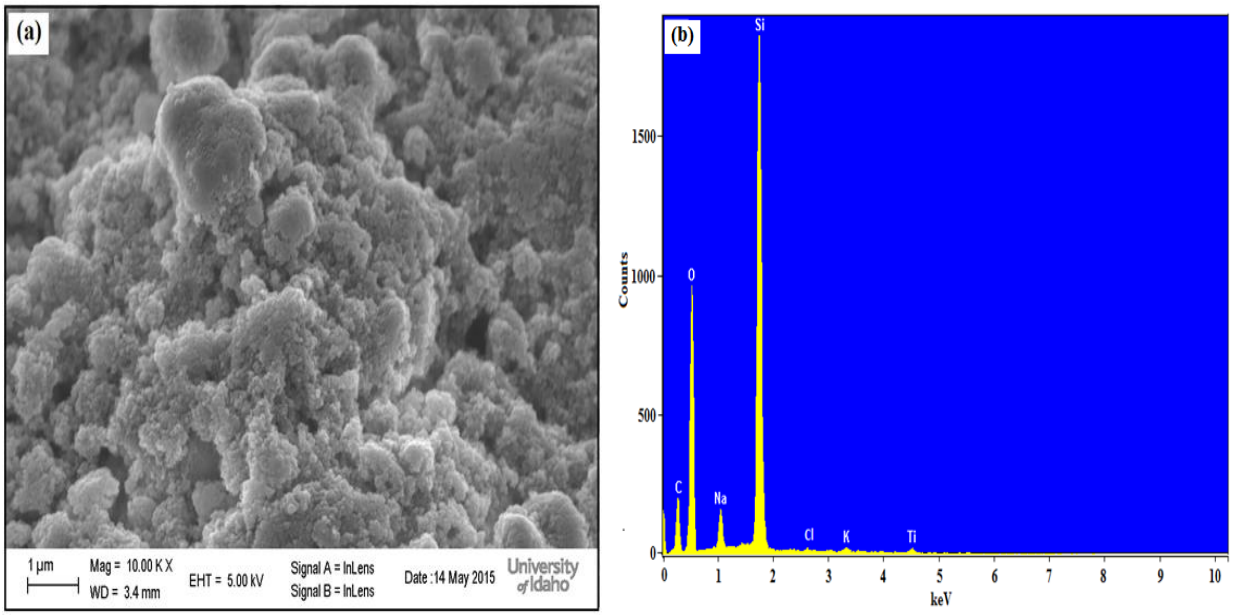

Figure 2.2.4: (a) SEM image (b) EDS spectrum of fresh 10 wt % C@ETS-10 adsorbent

2.2.5 Transmission Electron Microscopy (TEM)

The morphological investigations of as-synthesized samples were conducted by TEM (JEOL JEM 2100), and are shown in Figure 2.2.5. The ETS-10 particle-size ranged from 400-500 nm with well-defined square truncated bipyramid shape and flat surface (Figure 2.2.5a). The morphology of prepared hollow carbon is shown in Figure 2.2.5b & c (Yang and Truitt, 1996). Uniform-sized carbon nanospheres interconnected into netlike loose structure can be seen from the figure. The magnified image shows the hollow cores in carbon nanosphere (Zhu et al, 2012). Lattice fringes were not clearly visible in the image. Maximum carbon nanoparticle size was found in the range of 20-50 nm with polyhedron structure. Figure 2.2.5d-e show the images of 10 wt % C@ETS-10 nanostructured adsorbent/nanosorbent. Carbon nanoparticles (C) can be observed to be well dispersed onto ETS-10 surface. In addition, a large number of carbon nanoparticles do not have close contact with the surface of the ETS-10, possibly due to ionic charge on ETS-10 surface. The as-formed hollow carbon nanoparticles tended to agglomerate in absence of ETS-10. This suggests that ETS-10 acts as a support to control the agglomeration of

the loose hollow carbon particles onto C@ETS-10, and supported carbon nanoparticles maintain their original shape and size without any aggregation.

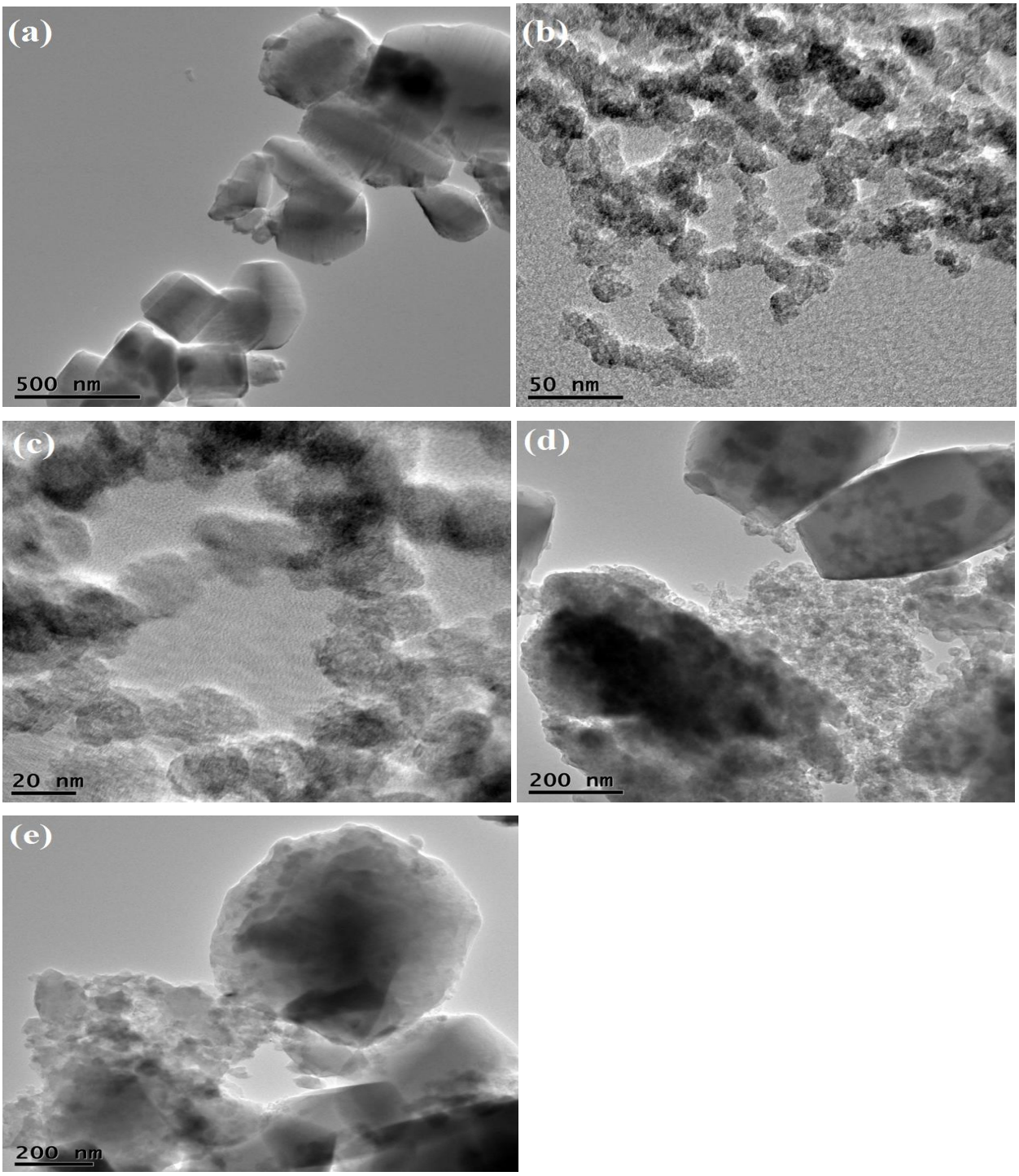

Figure 2.2.5: TEM images of (a) ETS-10, (b-c) Carbon (d-e) 10 wt % C@ETS-10 adsorbent

2.2.6 Brunauer-Emmett-Teller (BET) surface area and pore size distribution

Nitrogen adsorption-desorption isotherm of samples were carried out at 77 K with adsorption instrument TriStar II 3020, Micromeritics. The pore size of the samples was calculated from the N_2 adsorption/desorption data using the BJH method, and results are presented in Figure 2.2.6. The isotherm on activated carbon exhibits the characteristic type I curve, typical of microporous materials (Figure 2.2.6a). The pore volume and surface area were found to be 0.05 cm^3/g and 882 m^2/g, respectively (used in krypton isotherm). The average pore size of activated carbon was 0.29 nm. For 10 wt% C@ETS-10, the nitrogen adsorption-desorption isotherm exhibits the typical IV-type shape. The isotherm shown in Figure 2.2.6b, with a small hysteresis loop at the relative pressure between 0.3 and 1.0, indicates the diversity of pore in the sample. The calculated surface area and pore volume of sorbent were 130-149 m^2/g and 0.072 cm^3/g, respectively. The pore size distribution curve of 10 wt% C@ETS-10 indicate a large variation in diameter and average pore size of 39 nm. The properties of various samples are presented in Table 2.2.1. The pure carbon and ETS-10 surface areas were 70 and 242 m^2/g, respectively. The surface area of C@ETS-10 sorbent increased with increasing carbon loading on the support.

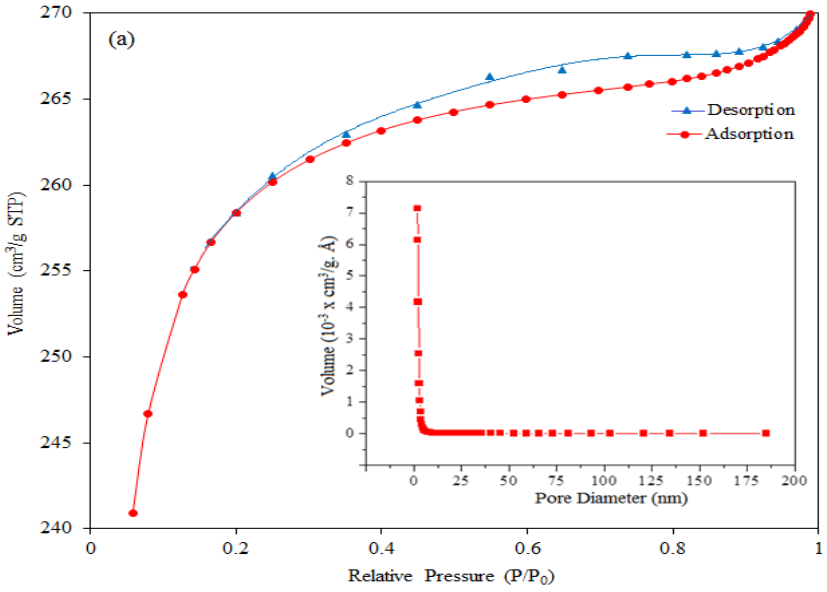

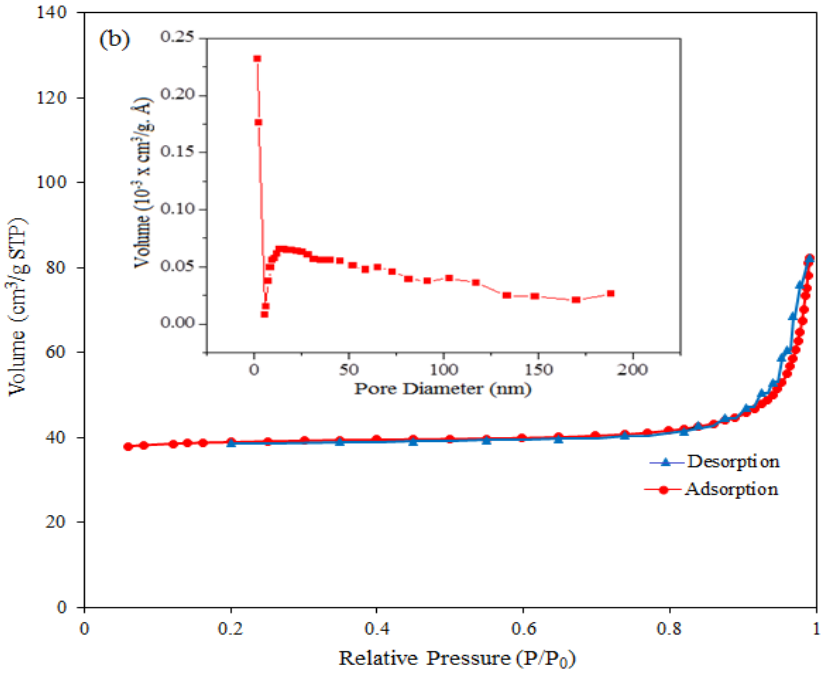

Figure 2.2.6: Nitrogen adsorption-desorption isotherms and the corresponding pore size distribution for (a) activated carbon (b) 10 wt % C@ETS-10

Table 2.2.1: Properties of the sorbent and support materials

Name	BET Surface area (m^2 g^{-1})	Average Pore size (nm)	Pore volume (cm^3 g^{-1})
Carbon	70	22.6	0.79
ETS-10	242	111.6	0.05
5 wt% C@ETS-10	118	-	-
10 wt% C@ETS-10	149	36.9	0.072
20 wt% C@ETS-10	145	-	-
Activated carbon	882	0.29	0.05

2.3 Characterization of used sorbents post-iodine adsorption experiments

2.3.1 SEM-EDS of Used Pellets

The iodine sorption experiments were carried out at 20 ºC column temperature, 150 mL flow rate and ~ 30 ppm iodine concentration on C@ETS-10 sorbents (experimental details described in section 3). After an experimental run, the presence of iodine on adsorbent pellets was confirmed by SEM-EDS (LEO SUPRA 35VP), as shown in Figure 2.3.1. SEM image of used sorbent indicates a slight change in morphology as compared to fresh sample (Figure 2.3.1a). The

orthorhombic/cubic crystal structure was observed on the surface of pellet. It is postulated that initially iodine molecules insert into the porous sites of adsorbent. When these sites are blocked, then the vapors of iodine adsorb on the surface of adsorbent. EDS spectra of the used 10 wt % C@ETS-10 were obtained to confirm the iodine presence on the adsorbent, and compared to the similar spectra of the fresh adsorbent. The new abundance of elemental iodine observed at 3.984 keV was due to presence of iodine onto the adsorbent (Figure 2.3.1b).

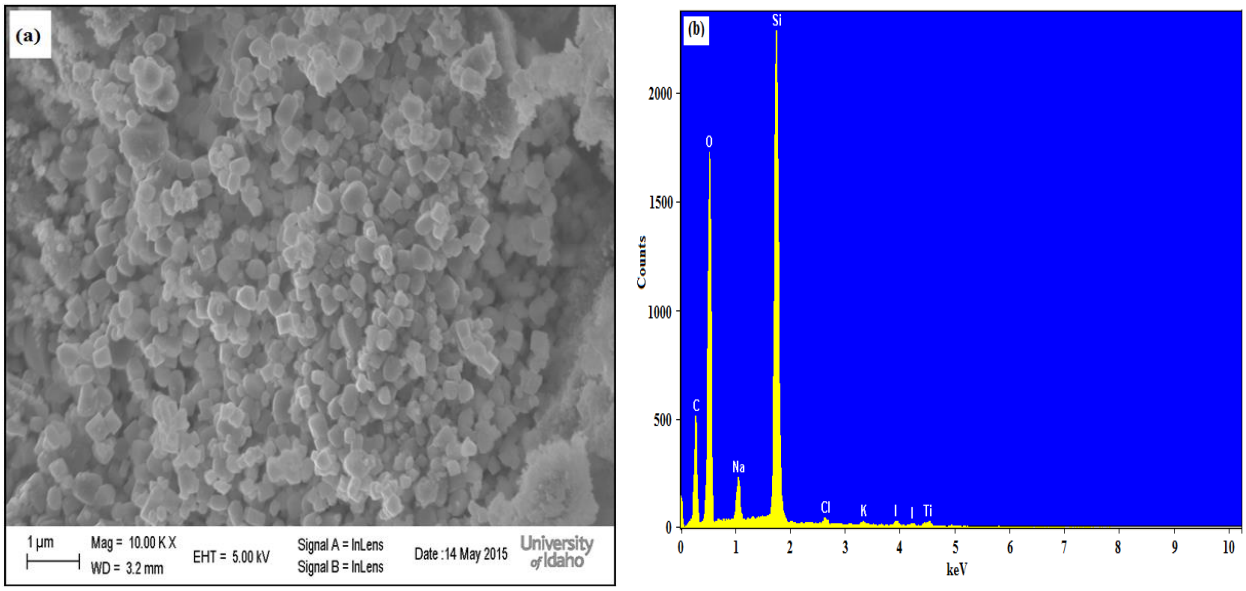

Figure 2.3.1: (a) SEM image (b) EDS spectrum of used 10 wt % C@ETS-10 for iodine adsorption

2.3.2 XRD of Fresh and Used Pellets

The crystalline structures of fresh and used (10 wt % C@ETS-10) pellets sorbents from the iodine experiments were analyzed using a powder XRD using Bruker D5000 (Germany), and the results are shown in Figure 2.3.2. Initially no iodine was present in fresh sample, as seen from the black colored pellets (Figure 2.3.2a - right). Carbon and ETS-10 sharp peaks can be seen in XRD. The iodine adsorbed on pellets caused black color to turn dark yellowish (Figure 2.3.2b - right). The used pellets (I_2-containing pellets) were ground to a powder in a mortar-and-pestle apparatus powder for XRD analysis. The iodine adsorbed on the pellets reduced the intensity of all the peaks of C@ETS-10.

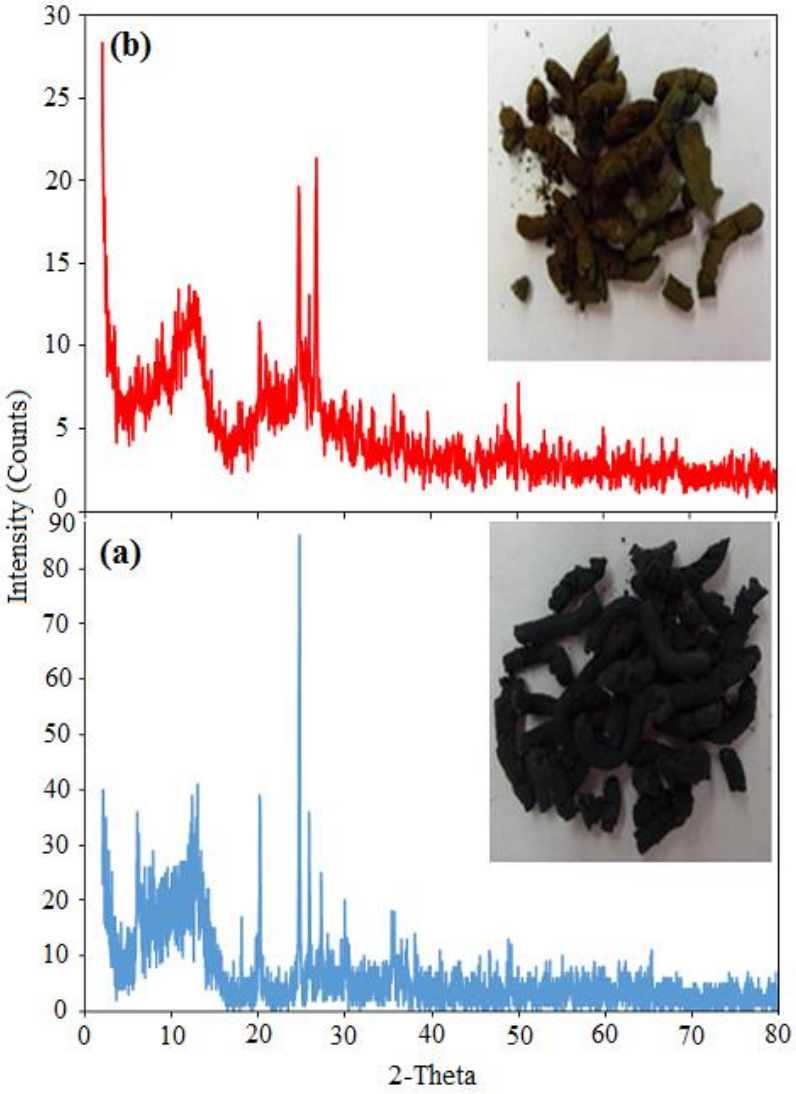

Figure 2.3.2: Photograph and P-XRD of (a) fresh pellets (b) used pellets of 10 wt% C@ETS-10

2.3.3 Thermogravimetric Analysis of Fresh and Used Pellets

Weight loss measurements of the as-synthesized samples were performed under argon atmosphere using thermogravimetric analysis (TGA), model STA 409 PC Luxx, Netzsch. Figure 2.3.3 shows that the thermogravimetric analysis of synthesized samples performed from room temperature to 1000 ºC. A heating rate of 15 ºC/min was used in the experiments. The total weight loss of 9.2 wt % observed for the ETS-10 sample includes a 6.8 wt % loss due to the dehydration of loosely bound water from the ETS-10 framework up to 340 ºC (Prasanth et al, 2010). After this temperature, rate of weight loss was slow up to 650 ºC, indicating the removal of water from the pores of ETS-10. Nanostructured carbon sample shows weight loss of about 15

wt %. A pristine 10 wt % carbon loaded ETS-10 sample shows 13.5 wt % total weight loss. Approximately 5 wt % weight loss was observed due to removal of moisture from sample in the initial period up to 200 ºC. Another potential cause of weight loss of adsorbent was the combined effect of carbon and ETS-10. At high temperature, carbon nanoparticles were removed from ETS-10 surface due to dehydration of ETS-10. The used sample showed 19.5 wt % weight loss. The iodine molecules adsorbed onto the sorbent pellets at two sites: (a) inside of sorbent pore (b) outer surface of sorbent. In initial ~10 min at around 150 ºC, outer surface-adsorbed iodine and water moisture desorbs from the sorbent. Further weight loss of sample can be attributed to desorption of captured (internal) iodine from adsorbent at continuous increasing temperature. Therefore, higher weight loss was observed during TGA.

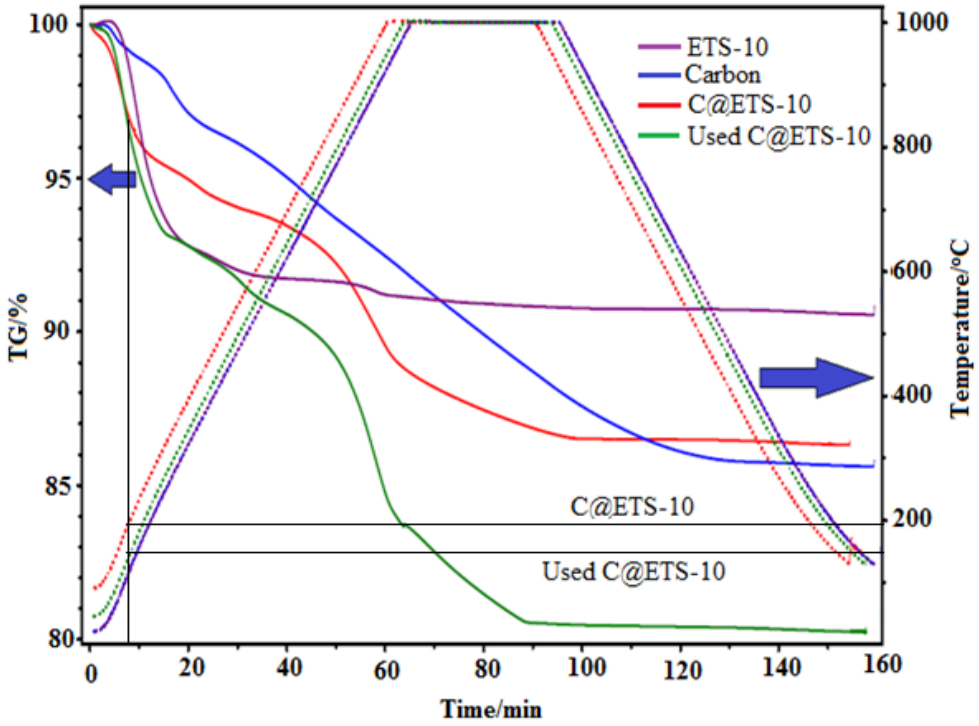

Figure 2.3.3: TGA of as-synthesized samples, fresh and used 10 wt % C@ETS-10 sorbent

2.4 Summary

ETS-10 supported nanostructured carbon polyhedron sorbent was synthesized via hydrothermal techniques for investigations of off-gas contaminant removal. The freshly synthesized sorbents as well as those used in sorption experiments were characterized by various techniques, such as SEM-EDS, TEM, XRD, Raman, BET surface area for detailed information regarding its structure, qualitative compositional analysis, surface area, and pore size distribution. Used C@ETS-10 pellets loaded with iodine after the sorption experiments were also characterized using SEM-EDS, XRD and TGA.

3 Determination of Adsorption Equilibria

3.1 Single Component Sorption Studies

3.1.1 Adsorption Equilibria for Krypton

3.1.1.1 Bench-scale adsorption system

The schematic diagram of lab scale experimental apparatus is shown in Figure 3.1.1. The apparatus was constructed of glass to avoid any adsorption on metal surface and metal corrosion. Adsorption column with the inside diameter 1" and a height 12" was packed with 0.003 kg of the synthesized nanosorbent. The temperature of the column was controlled by circulating the water through the jacket using an Isotemp digital temperature controller. Carrier gas nitrogen was flowed through sorbent loading column under 130 mL/min for 5 min to establish flow pattern before introducing Kr-nitrogen mixture. The flow rate of the krypton-nitrogen mixture was 4 mL/min, yielding a total flow rate of 134 mL/min. The residence time in the nanosorbent bed was 4.0 sec. The removal efficiency of nanosorbent was determined by analyzing the inlet and outlet streams at different time intervals. Krypton gas was analyzed using a gas chromatograph (*Hewlett Packard 6890 series*) equipped with CP-Molsieve 5Å 25 m × 0.25 mm × 30 mm capillary column with mass selective detector. The temperature of the GC capillary column was initially kept at 100°C for 5 min and then increased 30°C/min and held at 200ºC for 1 min. Helium flow rate was maintained 1.0 mL/min through the GC column.

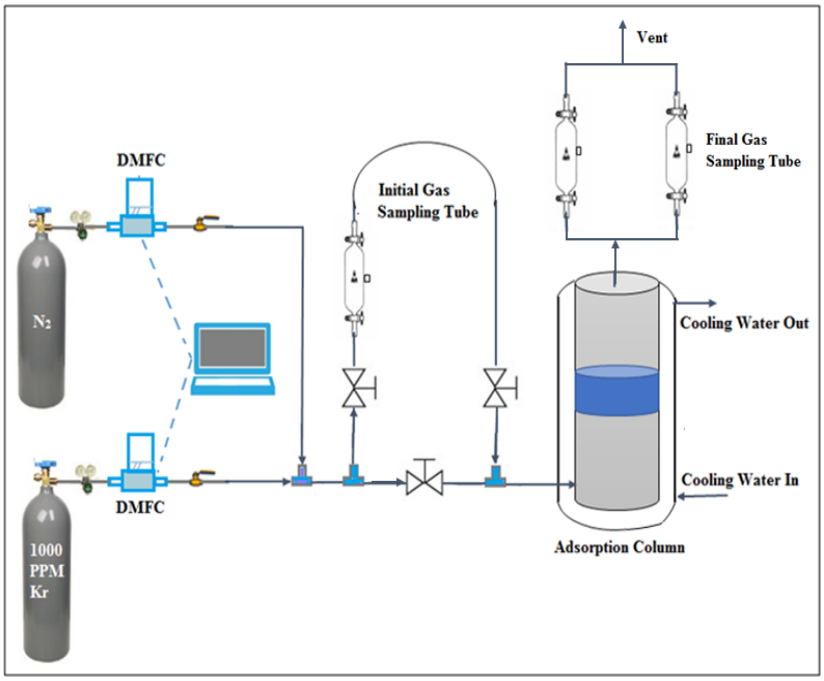

Figure 3.1.1: Schematic for lab scale experimental system

The capacity of sorbents were calculated by the following equation (equation 3.1.1):

$$q = \int_0^V \frac{(C_0 - C_e)}{M} \, dV \quad \text{---------- (3.1.1)}$$

where, q is the adsorption capacity (mmol kg^{-1}), C_0 (mmol L^{-1}) and C_e (mmol L^{-1}) are the inlet and outlet concentrations, respectively, V is the total volume processed at breakthrough (L), and M is the mass of nanosorbent (kg).

3.1.1.2 Breakthrough curve

Figure 3.1.2 shows the breakthrough curves of C@ETS-10 and activated carbon for krypton gas adsorption. Eq. 3.1.1 was used to calculate the true capacities of sorbents by integrating the areas above the curve. The capacities were calculated at 263 K and 0.1 torr pressure drop. Bazan et al. (2011) reported that activated carbon is usually considered to be a benchmark adsorbent for the removal of noble gases such as Kr and Xe. From the breakthrough curve, the sorption capacities of 10 wt % C@ETS-10 nanosorbent and activated carbon were found to be 0.75 and 0.64 mmol/kg, respectively. The capacity of synthesized nanosorbent was 15% higher than the activated carbon, despite the greater surface area of the activated carbon. The lower capacity of the activated carbon is potentially attributable to greater diffusional mass transfer resistances in the narrow pores of activated carbon as compared to the larger pores of the C@ETS-10, which

makes the entire surface available for sorption. As seen from the breakthrough curve, the sorbent approached saturation in about 10 min. The operational capacities of 10 wt % C@ETS-10 nanosorbent and activated carbon at 10 min were 0.45 and 0.4 mmol/kg, respectively. Therefore, other parameters, namely, the effects of temperature and carbon loading on 10 min sorption capacity of C@ETS-10 were studied.

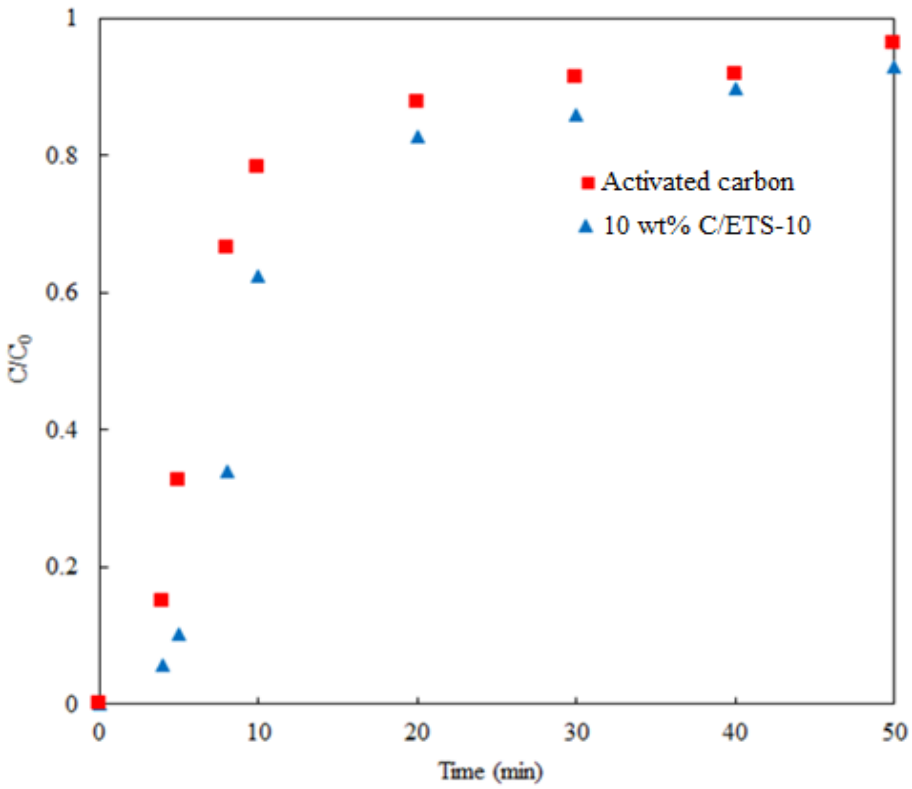

Figure 3.1.2: Breakthrough curve for krypton adsorption at different sorbents

3.1.1.3 Effect of temperature

Adsorption of krypton on sorbents was studied at temperatures ranging from 263-293 K, at constant pressure drop of 0.1 torr across the column. Figure 3.1.3 shows the activity of 10 wt % C@ETS-10 and activated carbon as a function of temperature. It was observed that 10 wt % C@ETS-10 nanosorbent had higher removal efficiency of krypton gas at lower temperature than activated carbon. The capacity of sorbent gradually decreased with increase the temperature of system which was due to the exothermic nature of the adsorption process. Lower temperature would be favorable for the adsorption of krypton on 10 wt % C@ETS-10.

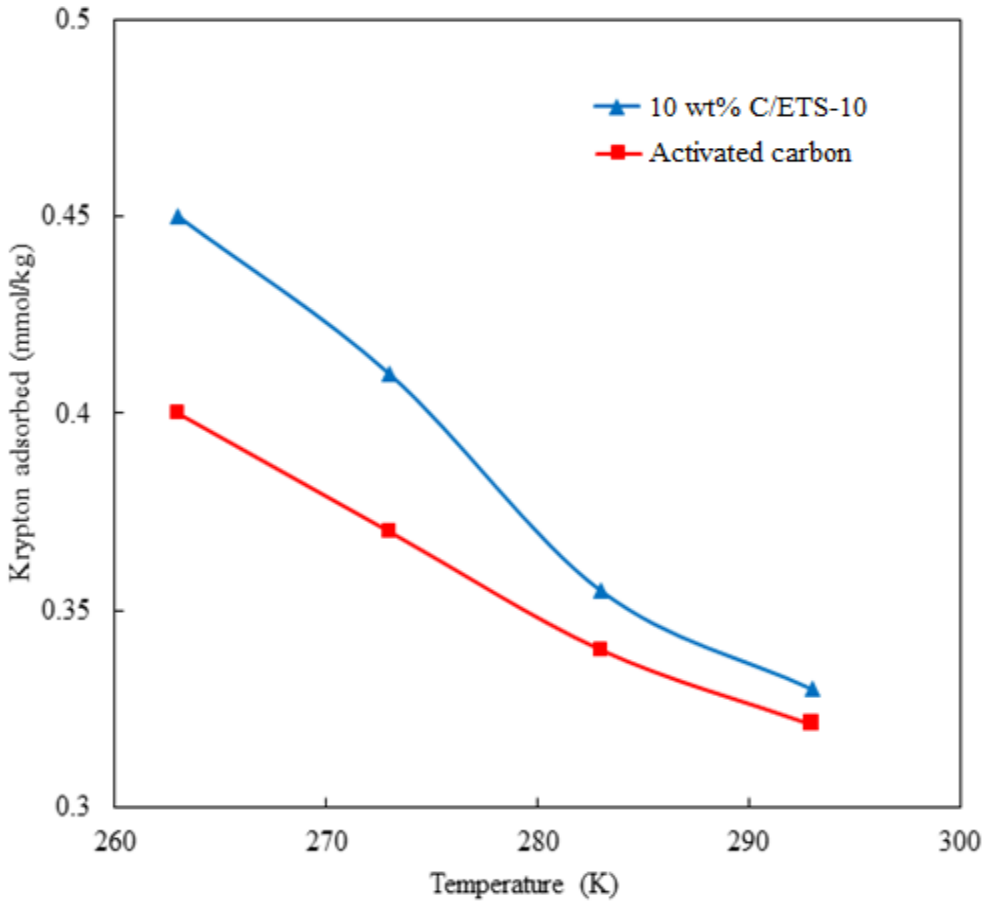

Figure 3.1.3: Effect of temperature vs adsorption capacity of sorbent

3.1.1.4 Effect of carbon loading

Adsorption of krypton at 263 K was studied on the C@ETS-10 nanosorbent at different carbon loading (3-20 wt %). The capacity of the nanosorbent was observed to increase with an increase in carbon loading from 3 to 10 wt%. After 10 wt % carbon loading gas adsorption decreased slightly, possibly due to the formation of the light carbon cluster on the surface of support (Figure 3.1.4). In between 3 to 10 wt% carbon loading, the capacity increased by ~ 6.0% between each successive loading level. However, for carbon loadings in 10-20 wt % the average increase was only ~1.2%. The 10 wt% C@ETS-10 nanosorbent adsorbed 1.27 mg/kg of krypton and would be more economical than 20 wt% C@ETS-10.

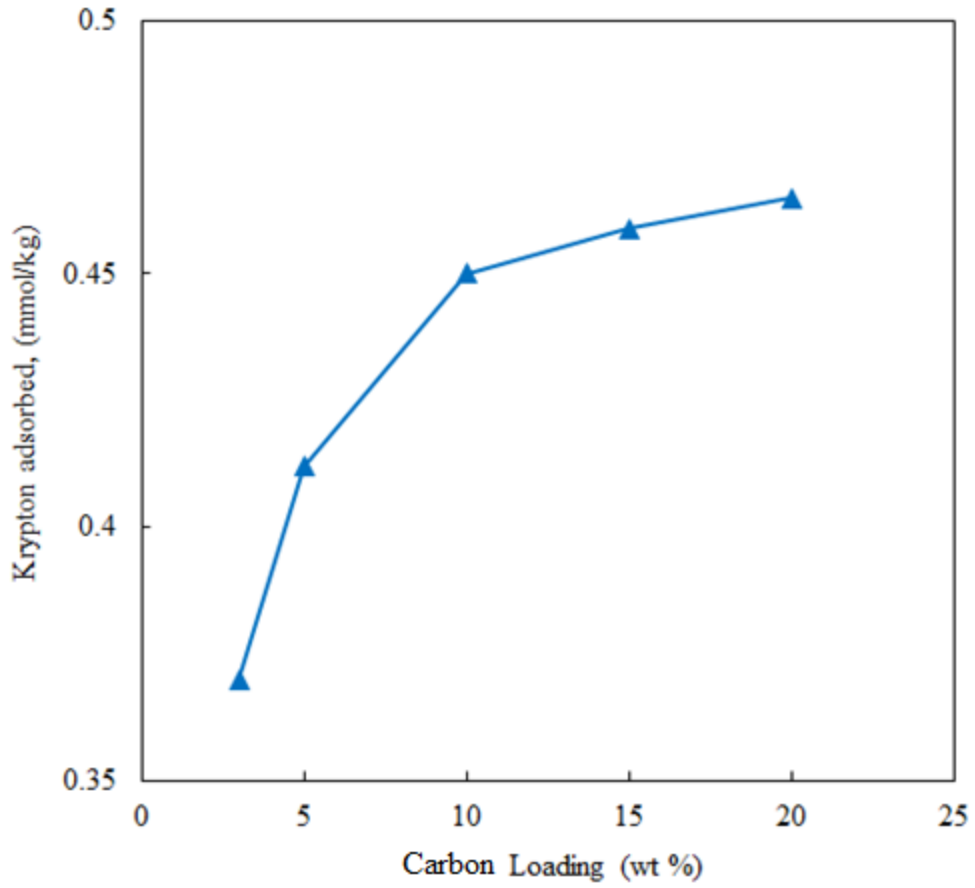

Figure 3.1.4: Effect of carbon loading on gas adsorption capacity of sorbent

3.1.2 Adsorption Equilibria for Iodine

3.1.2.1 Experimental setup

The krypton sorption set-up was modified for the iodine adsorption. Figure 3.1.5 shows the revised experimental setup for capture of iodine from gas stream. The prepared C@ETS-10 adsorbent (1.0 g) was packed in a 1 inch inside diameter and 12 inch height jacked column made of pyrex glass to avoid any adsorption on metal surface and metal corrosion. Two g elemental iodine (nonradioactive) was placed in a 25 mL jacked iodine glass vaporizer, where nitrogen purge served as the carrier gas for iodine vapor. The temperatures of iodine vaporizer (40±2 ºC) and adsorption column (10-60 ºC) were maintained by circulating the water through the respective jackets using two different temperature controlled water baths. The experiments were performed at atmospheric pressure. Carrier gas nitrogen was flowed through adsorbent loading column at a flow rate of 130 mL min^{-1} to establish flow pattern through the column for 5 min

prior to starting the carrier gas flow through the iodine vaporizer at 20 mL min^{-1}, yielding a total flow rate of 150 mL min^{-1}. The partial pressure of elemental iodine in the gas was 0.025±2 mm Hg (concentration - 32±3 ppm). The residence time in the nanostructured adsorbent column was 1.6 second. Removal efficiency of adsorbent was determined by analyzing the iodine concentrations in inlet and outlet streams. Iodine analysis was performed by trapping iodine in de-ionized water (solubility of iodine in water 1 g/3450 mL at 20 ºC) by passing the streams through bubblers (bubbler-1 for inlet, and bubblers 2 and 3 for outlet). Complete trapping of iodine in bubbler 2 was confirmed by the absence of iodine in bubbler 3. The iodine trap water was analyzed by the Leuco Crystal Violet (LCV) method using Thermo Scientific Evolution 60S UV-Visible Spectrophotometer.

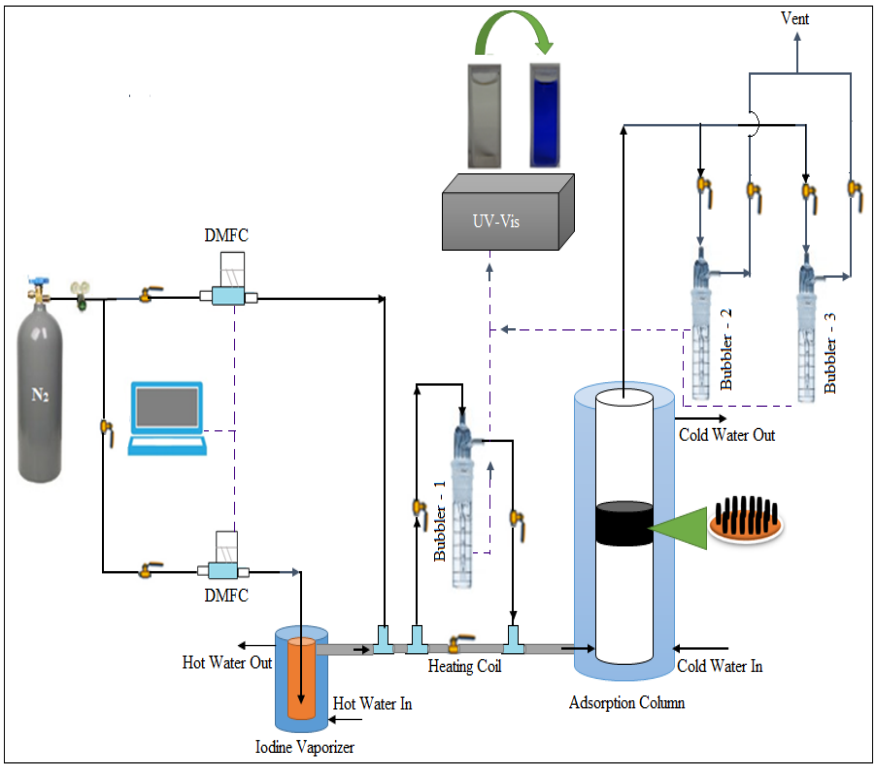

Figure 3.1.5: Schematic diagram of lab scale iodine adsorption experimental apparatus

3.1.2.2 Iodine capture: sorbent comparison

The performance evaluation of synthesized materials (carbon and ETS-10) and nanostructured adsorbents, C@ETS-10 for capture of gas phase iodine was conducted at 20 °C. Figure 3.1.6 shows the breakthrough curve of each sample (C/C_0) plotted as a function of time. The adsorption capacity of each sample was calculated by integrating the area above the curve

according to equation 3.1.1. Freshly prepared pellets of each sample were used in adsorption test. As seen from the breakthrough curves, the outlet iodine concentration was low at the beginning of the experiment, increasing gradually with time. Notably, black color of sorbent gradually changed into dark yellow from the bottom to the top providing a visual indication of iodine sorption. The results show that pure ETS-10 and carbon have lower iodine adsorption capacity, 5.5 and 11.5 mg g^{-1}, respectively, compared to the 10 wt % C@ETS-10 which had the iodine capture capacity of 28.9 mg g^{-1}. ETS-10 has higher surface area and pore size, but lower iodine adsorption capacity, possibly due to higher adsorption-desorption rate of iodine molecules on sorbent (average pore size – 111.6 nm). It is postulated that C@ETS-10 holds the iodine molecules within both the internal and external structure (average pore size – 36.9 nm).

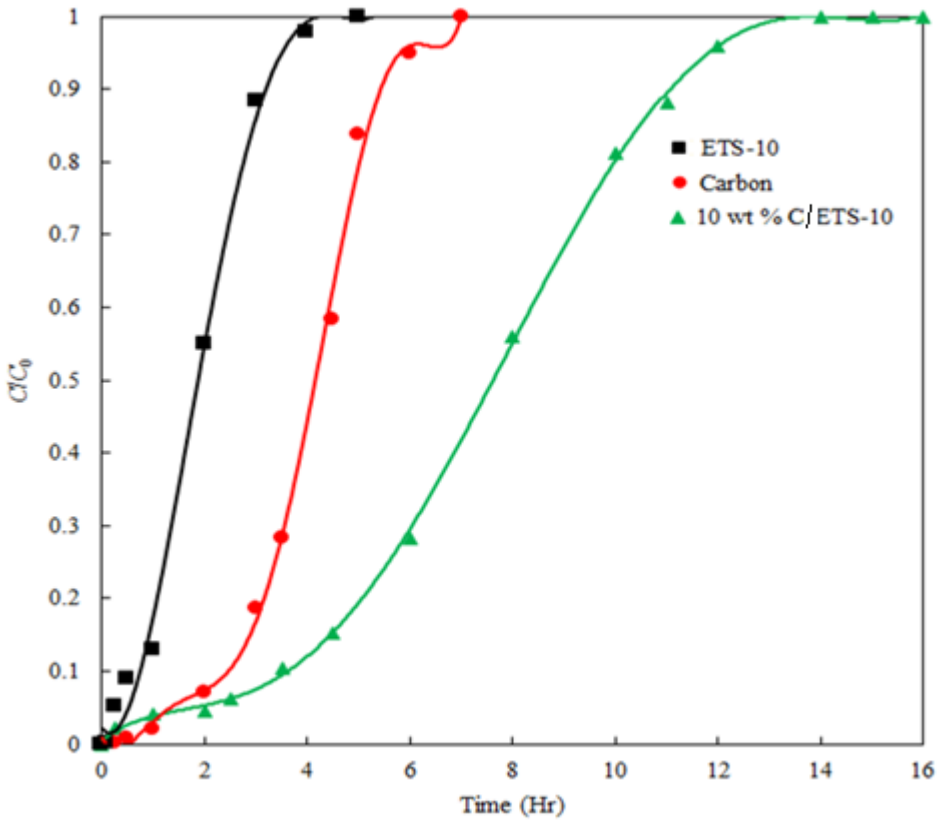

Figure 3.1.6: Breakthrough curve vs time for ETS-10, Carbon and 10 wt % C@ETS-10 sorbent

3.1.2.3 Effect of carbon loading on iodine capture

Iodine removal capacities of the sorbent with different carbon loading (3-20) wt % C@ETS-10 were determined at 20 °C and are shown in Figure 3.1.7. Iodine removal from gas stream was

observed to increase with an increase in carbon loading on ETS-10 from 3 -10 wt %. A 10 wt % C@ETS-10 was found to have the highest adsorption capacity, 28.9 mg g^{-1}, due to higher surface area of sample, 149 m^2 g^{-1}. But further increases in carbon percentages on ETS-10 showed a decrease in the iodine adsorption capacity. It might be possible that at higher carbon loading particles would be overlap on each other forming carbon clusters that block the active sites of sorbents. Therefore, the 10 wt % C@ETS-10 was selected for studying the effects of additional parameters – operating temperature and bed height.

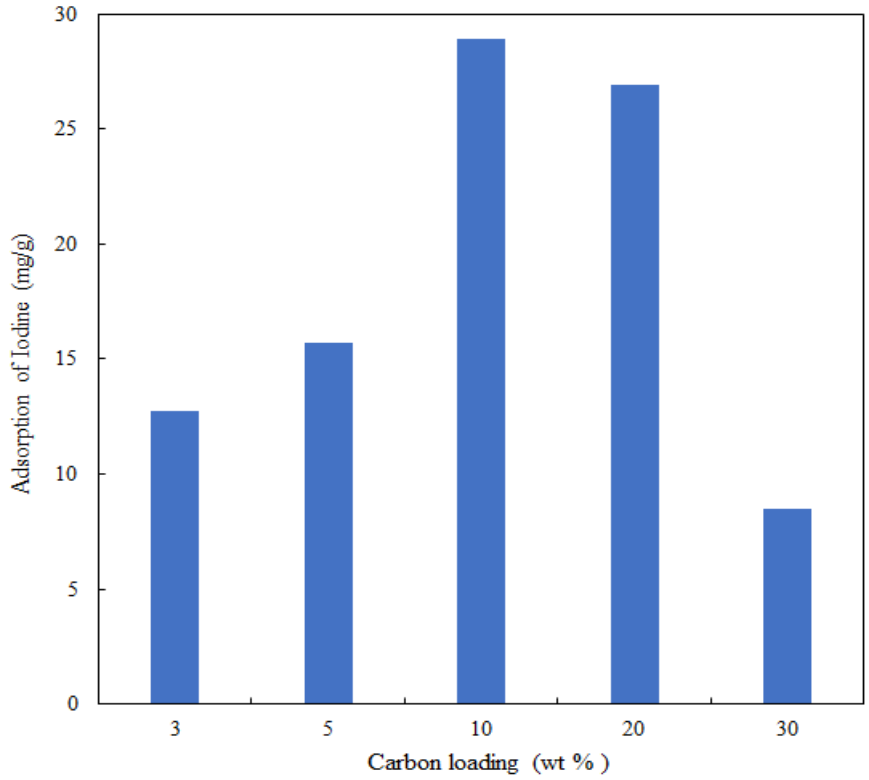

Figure 3.1.7: Effect of carbon loading on capture of iodine

3.1.2.4 Effect of temperature on iodine capture

Figure 3.1.8a shows the effect of adsorption temperature on the capture of iodine by 10 wt % C@ETS-10 by analyzing the breakthrough curves at temperatures ranging from 10 – 60 ºC. The breakthrough point decreased with an increase in the temperature of the adsorption column. Figure 3.1.8b shows the adsorption capacity of 10 wt% C@ETS-10 calculated from equation 1 at different temperatures. The adsorption capacity gradually decreased with an increase in column temperature from 30.1 mg g^{-1} at 10 ºC to 9.6 mg g^{-1} at 60 ºC. The capacity at the lowest

temperature, 10 ºC was only 4 % higher than that at 20 ºC. This is only a physical adsorption phenomena, in which iodine molecules adsorb on the surface of sorbent due to the van der Waals force of attraction. At the lowest temperature (10 ºC), iodine would be condensing from the gas stream, therefore, 20 ºC was selected as the operating temperature to examine the effect of bed height.

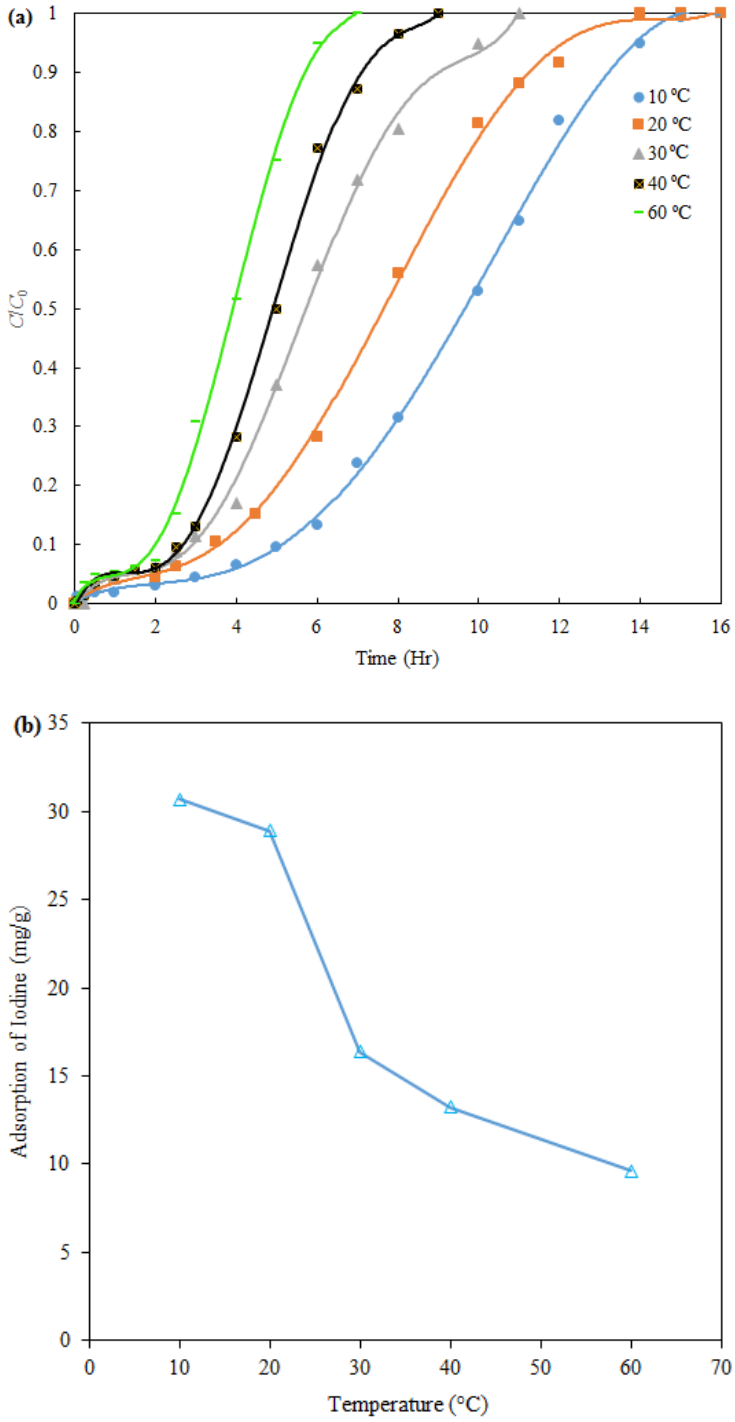

Figure 3.1.8: (a) Breakthrough curve and (b) Iodine adsorption capacity of 10 wt % C@ETS-10 at different temperatures

3.1.2.5 Effect of adsorbent bed height

The height of adsorbent bed was varied in another set of experiments to study a possible effect of flow maldistribution on iodine capacity of sorbent in column. The adsorption capacity of adsorbent was calculated from breakthrough curves for different bed heights (4 - 36 mm) at 20 ºC. The breakthrough and exhaustion times increased with increasing bed height. Figure 3.1.9a shows that the iodine sorption capacity of adsorbent with amount of sorbent used in different bed heights. At low bed height (4-5 mm), the sorbent saturated rapidly, and yielding adsorption capacity of 24.2 mg g^{-1} with 0.79 g adsorbent. The sorbent capacity was 28.9 mg g^{-1} at 6-7 mm bed height (1.0 g - adsorbent), and it gradually increased with bed height. A higher capacity of adsorbent (39.3 mg g^{-1}) was observed at higher bed height, 35-36 mm, due to the large amount of 10 % C@ETS-10 adsorbent (5.35 g) in column. These results suggested that (a) observed sorbent capacity increases linearly with amount at lower amounts, and (b) sorbent capacity is approaching a limiting maximum value at high amounts. These two statements indicate a Langmuir isotherm type relationship between observed capacity and adsorbent amount. The maximum (limiting) sorbent capacity is calculated by linearizing the relationship as shown below (Langmuir, 1918):

$$\left(\frac{1}{Q_e}\right) = \left(\frac{1}{Q_m}\right) + \left(\frac{1}{K_L Q_m M}\right) \quad \text{---------- (3.1.2)}$$

where, Q_m = maximum adsorption capacity (mg g^{-1}), Q_e = equilibrium observed capacity (mg g^{-1}), M = equilibrium amount of adsorbent (g), K_L = characteristic adsorption constant. The adsorption capacity (Q_m) was found to be ~ 40.0 mg g^{-1} from linear plot of $1/Q_e$ vs $1/M$ (Figure 3.1.9b).

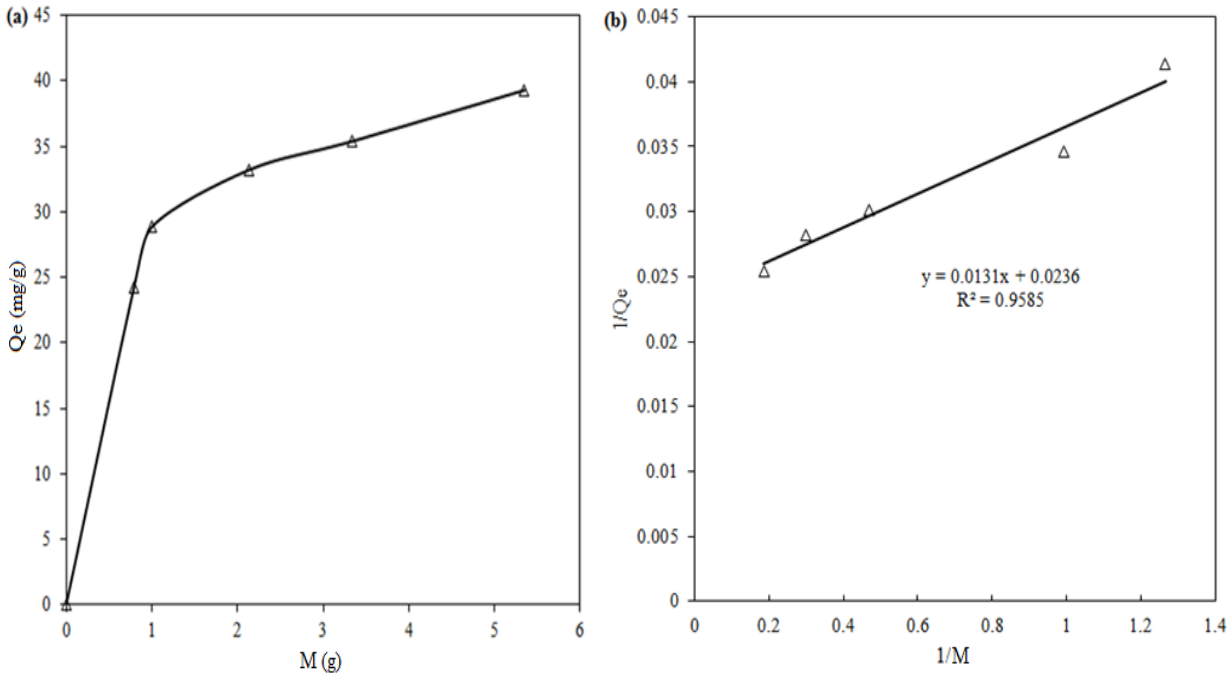

Figure 3.1.9: (a) Effect of bed height (amount of adsorbent) on iodine adsorption (b) Linear fir for Langmuir model for iodine adsorption on 10 wt % C@ETS-10

3.2 Multicomponent Sorption Studies

3.2.1 Experimental Set-up and Procedure

For multicomponent adsorption experimental apparatus was modified from the one reported previously for single adsorption system. The schematic diagram of new lab scale experimental apparatus is shown in Figure 3.2.1. Several parts of the system such as gas flow lines, jacked adsorption column (1 inch I.D. and 12 inch height) and iodine vaporizer (25 mL) were made of pyrex glass to prevent adsorption of iodine on metal surface and metal corrosion. Two g elemental iodine (Fisher Scientific, USA) was packed into the jacketed iodine vaporizer, where 10 mL min^{-1} of Kr balanced with nitrogen (1000 ppm, Airgas, USA) purge served as a carrier gas for iodine vapor. The concentration of iodine gas-phase was adjusted by controlling the temperature (45±3ºC) of iodine vaporizer by circulating the water through the jacket from water bath. The resulting stream containing iodine and krypton in nitrogen was mixed with another stream of nitrogen gas yielding a total flow rate of 150 mL min^{-1}. The gas containing iodine and krypton was then passed through adsorption column.

Known quantity of 10 wt% C@ETS-10 nanosorbent was packed into the adsorption column (10 wt% C@ETS-10 optimized for krypton and iodine sorption). The temperature of the adsorption column was maintained at 20ºC by circulating the water through jacket from another water bath. The removal efficiency of prepared nanosorbent was calculated by analyzing the inlet and outlet concentrations of streams. Iodine analysis was performed by trapping iodine in de-ionized water by passing the streams through bubblers (bubbler-1 for inlet and bubbler-2 for outlet), followed by the analysis of the iodine trap water by the Leuco Crystal Violet (LCV) method using Thermo Scientific Evolution 60S UV-Visible Spectrophotometer. Outlet sample for krypton analysis was collected after trapping iodine in de-ionized water. A moisture trap was used to dry the gas stream prior to collection of the krypton outlet sample. Krypton concentration was measured by Gas Chromatograph equipped with TCD using Carboxen-1010 PLOT capillary column, long 30 m × 0.53 mm ID. The temperature of capillary column was initially kept at 80ºC for 3 min and then increased at 10ºC/min to 200ºC and held at that temperature for 1 min. Helium was used as a carrier gas at 3 mL min^{-1}.

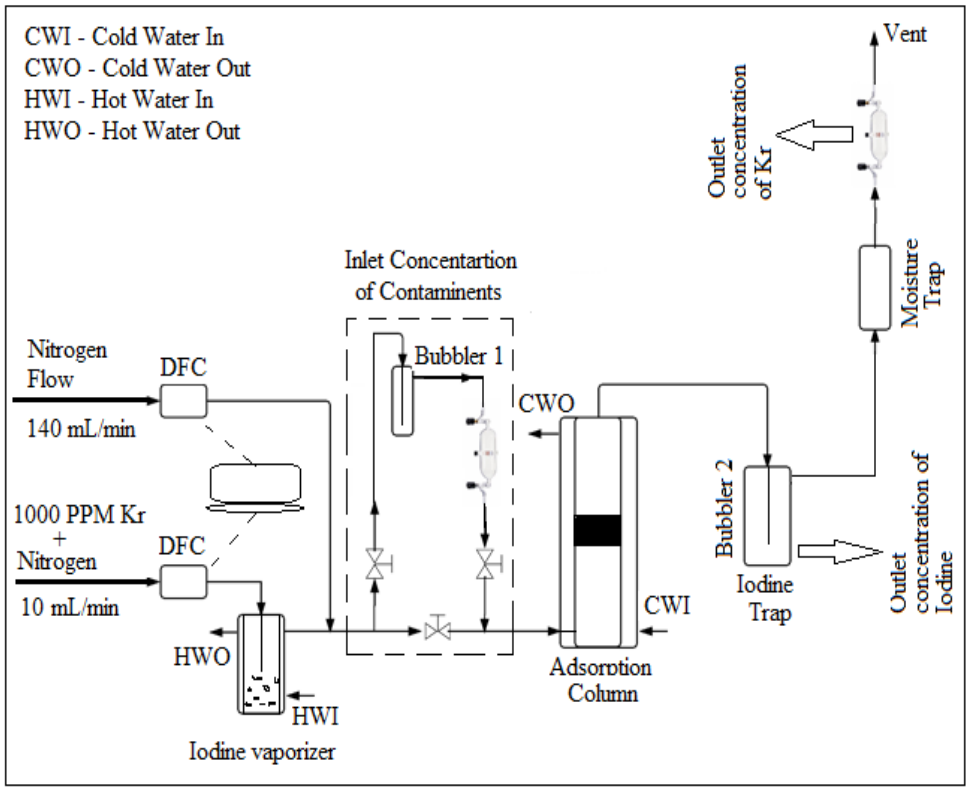

Figure 3.2.1: Schematic diagram of lab scale apparatus for adsorption of iodine and krypton from gas stream

3.2.2 Effect of Empty Bed Contact Time (EBCT)

Figure 3.2.2 shows the breakthrough curves for krypton and iodine on 10 wt% C@ETS-10 as a function of time at 20 ºC, and two different empty bed contact times (EBCTs): 1.4 s (1 g - sorbent) and 3.5 s (2.5 g – sorbent). The experiment was conducted at higher EBCT to mitigate the flow maldistribution effects. For both EBCTs, Kr breakthrough was observed within 1 h (Figure 3.2.2a). Negligible outlet concentration of iodine was observed (Figure 3.2.2b) in this time. The capacity of sorbent was calculated using Eq. 3.1.1 for the multicomponent off-gas stream. The Kr adsorption capacity of 10 wt% C@ETS-10 was 0.143 mg g^{-1} for 1.4 s and 0.102 mg g^{-1} for 3.5 s EBCT. The outlet concentration of iodine gradually increased with increase in experiment time. The iodine sorption capacity of 1.4 and 3.5 s EBCT was 24.5 and 27.5 mg g^{-1}, respectively.

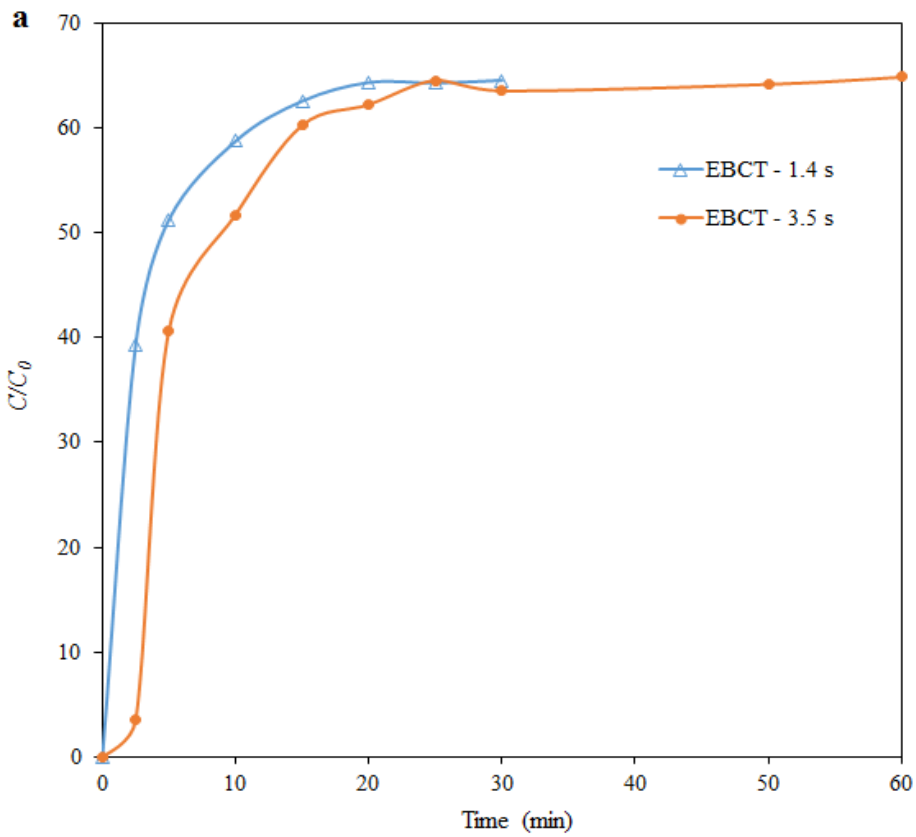

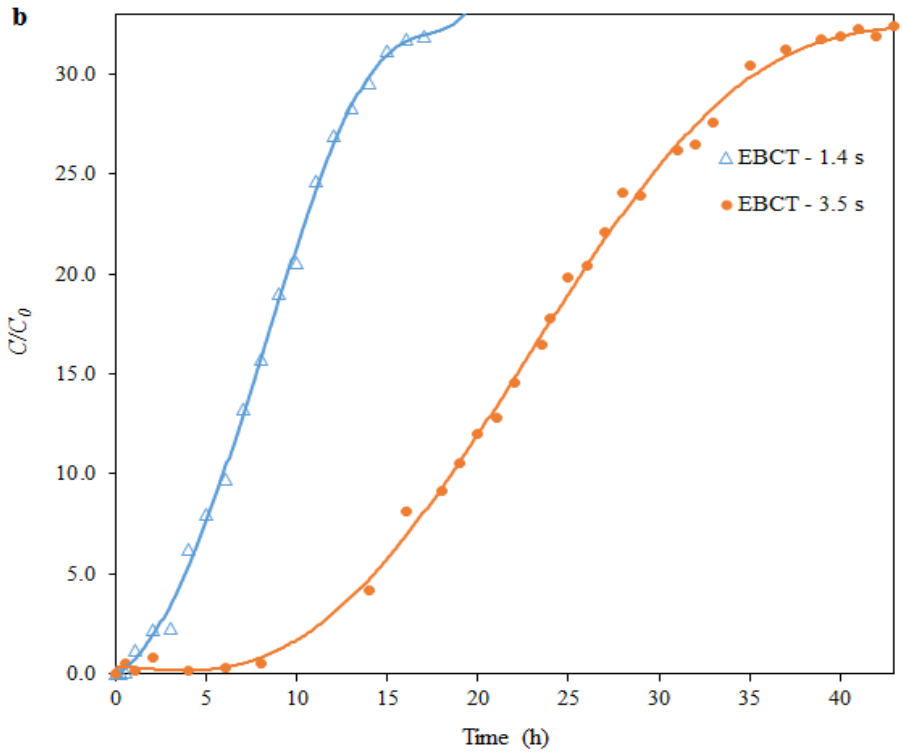

Figure 3.2.2: Breakthrough curve of (a) krypton and (b) iodine adsorption on 10 wt% C@ETS-10 at 20 °C

3.2.3 Effect of Multiple Components

Three different experiments were performed to test the effect of presence of both contaminants on sorption. In the first experiment, the sorbent was first saturated with pure iodine (25 ppm), and then krypton was introduced into the inlet stream at 70 ppm. In the second experiment, iodine was introduced into the inlet stream containing krypton after saturating sorbent by krypton. In the third experiment, both the contaminants (I_2 & Kr) were passed through the sorbent simultaneously. Figure 3.2.3 shows the breakthrough curves for both iodine and krypton. Examination of the Figure 3.2.3a indicates introduction of the second contaminant causes a slight reduction in the breakthrough times of either contaminant. Kr capacity decreased from 0.2002 mg g^{-1} (in absence of iodine) to 0.1135 mg g^{-1} when both the contaminants were fed simultaneously. Figure 3.2.3b shows the iodine breakthrough curves. It is observed that having been previously saturated with krypton does not affect the sorbent's iodine sorption capacity. While passing krypton and iodine simultaneously, however, the breakthrough time decreased from ~50 to ~40 h and iodine capacity decreased from 32.56 mg g^{-1} to 29.63 mg g^{-1}.

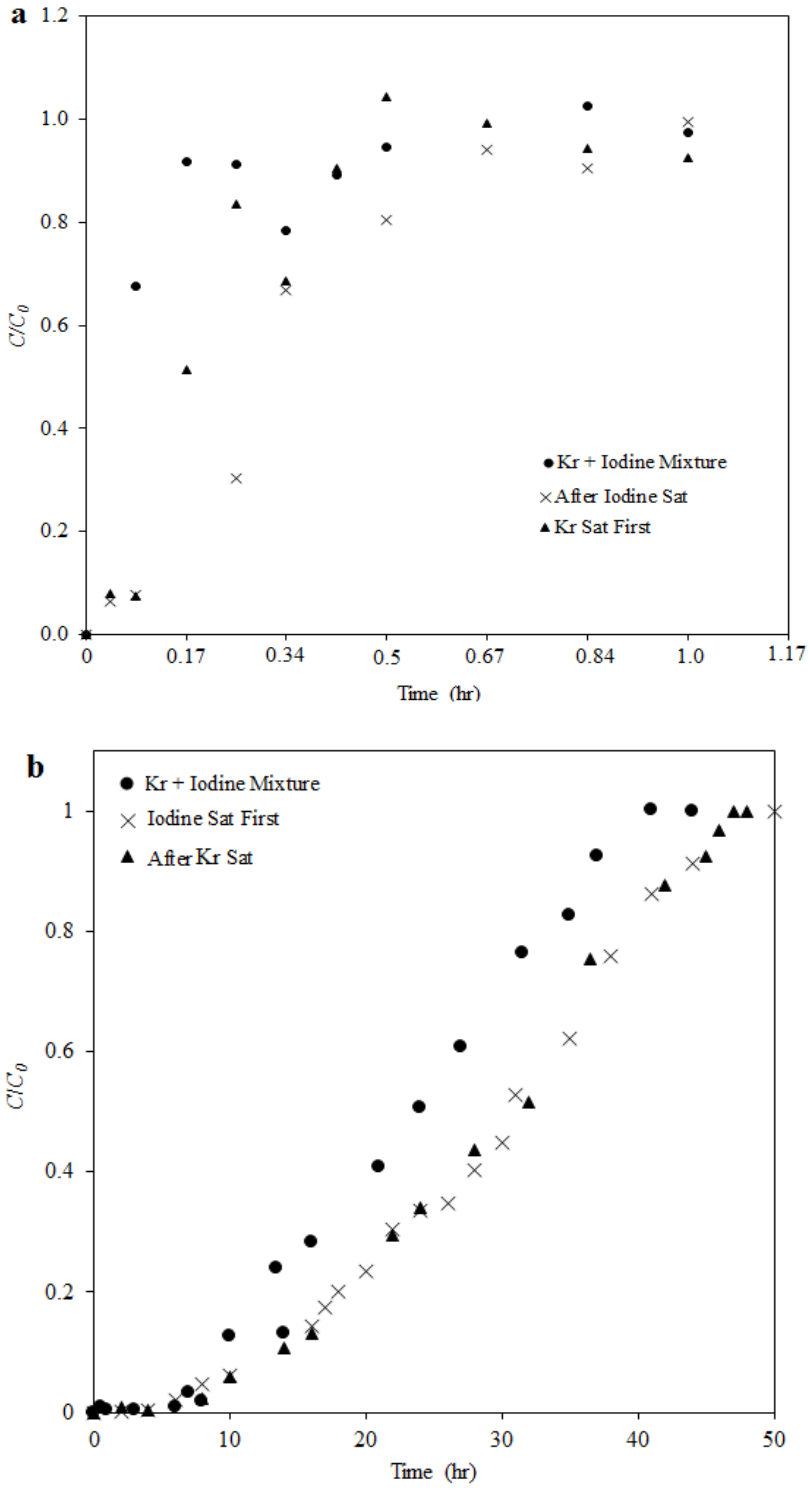

Figure 3.2.3: Interaction of components: (a) effect of iodine on krypton, and (b) effect of krypton on iodine sorption on 10 wt% C@ETS-10

(Total gas flow – 180 mL/min; I_2 Concentration – 25±2 ppm; Kr Concentration – 70±5 ppm; column temperature – 20 ºC; amount of sorbent – 2.5 g)

3.2.3.1 Effect of inlet concentration of iodine

The effect of krypton concentration on iodine sorption capacity of 10 wt% C@ETS-10 sorbent was studied by varying the inlet concentration of iodine from 15 – 50 ppm, while maintaining the inlet Kr concentration constant at 70 ppm. Figure 3.2.4 shows the breakthrough curves for iodine at the column operating temperature of 20 °C. The iodine capacity of sorbent was plotted with concentration of iodine in Figure 3.2.5. It was observed that the iodine sorption capacity of sorbent increased with increase in iodine concentration. The lowest and highest sorbent capacities of sorbent were found to be 39 and 49 mg g^{-1} at 17 and 50 ppm I_2 concentration, respectively.

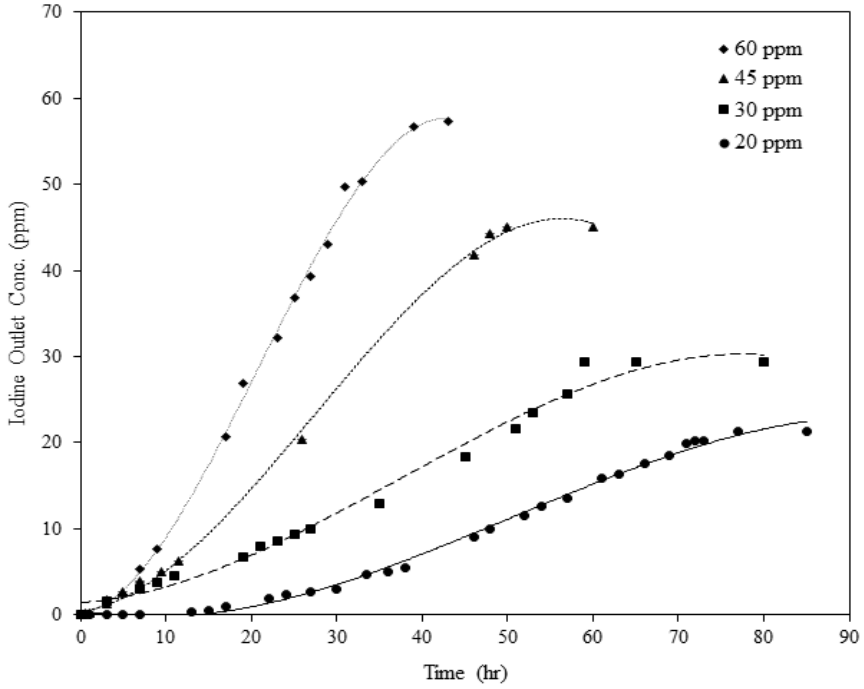

Figure 3.2.4: Breakthrough curve of iodine adsorption of different iodine concentration on 10 wt% C@ETS-10 at 20 °C
(Total gas flow – 180 mL/min; Kr Concentration at inlet - 70 ppm; amount of sorbent – 2.5 g)

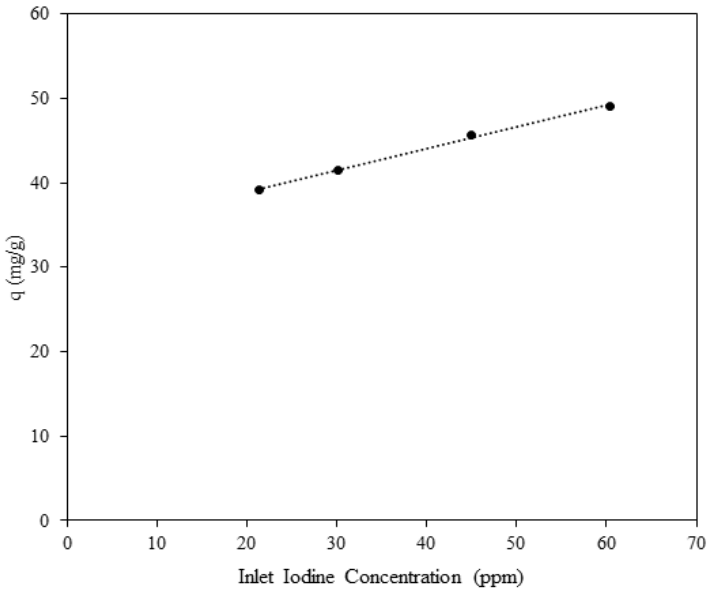

Figure 3.2.5: Effect of iodine concentration on capacity of 10 wt% C@ETS-10 sorbent at 20 °C

(Total gas flow – 150 mL/min; Kr Concentration at inlet - 67 ppm; amount of sorbent – 2.5 g)

3.2.3.2 Effect of inlet concentration of krypton

The effect of krypton concentration on Kr sorption capacity of 10 wt% C@ETS-10 sorbent was studied by varying the inlet concentration of Kr from 70 – 150 ppm, while maintaining the inlet iodine concentration constant at 25 ppm throughout the experiment. The breakthrough curves were plotted with outlet concentration of Kr versus time are shown in Figure 3.2.6. Kr sorption capacity of sorbent was increased with increase in inlet concentration of Kr. The minimum and maximum sorbent capacities of sorbent were found 0.0323 and 0.0617 mg g^{-1} at 70 and 150 ppm Kr concentration, respectively.

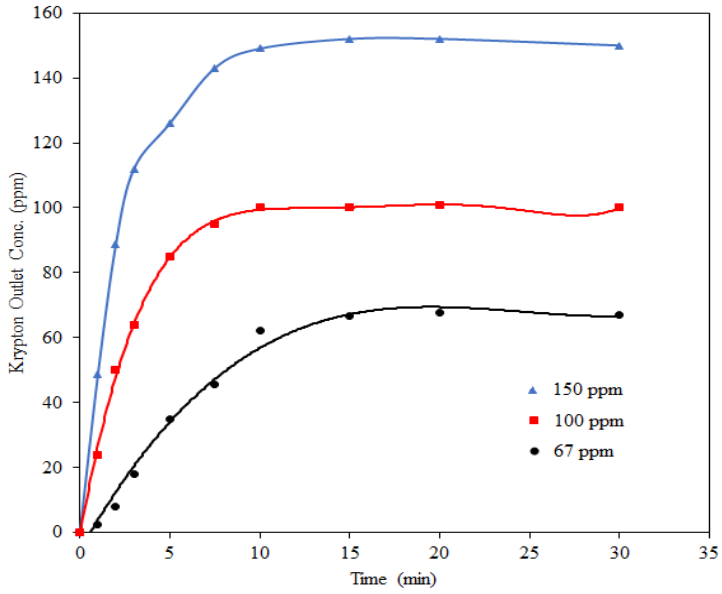

Figure 3.2.6: Breakthrough curve of krypton adsorption of different krypton concentration on 10 wt% C@ETS-10 at 20°C
(*Experimental conditions: Total gas flow – 180 mL min^{-1}; I_2 concentration at inlet - 25 ppm; amount of sorbent – 2.5 g*).

3.2.3.3 Effect of temperature on multicomponent sorption

The effect of temperature (20 - 60°C) on the sorption capacity of 10 wt% C@ETS-10 sorbent was studied for multicomponent gas stream containing 25 ppm I_2 and 67 ppm Kr inlet concentrations. Figure 3.2.7a & b show the breakthrough curves of the two components (iodine and Kr) on 10 wt% C@ETS-10 at different temperatures. The capacity of sorbent decreased with increase in column temperature, possible due to exothermic nature of the adsorption process of I_2 and Kr contaminants. The capacities of sorbent decreased from 41.5 to 27.9 mg g^{-1} for I_2 and 0.0323 to 0.0245 mg g^{-1} for Kr from 20 to 60°C.

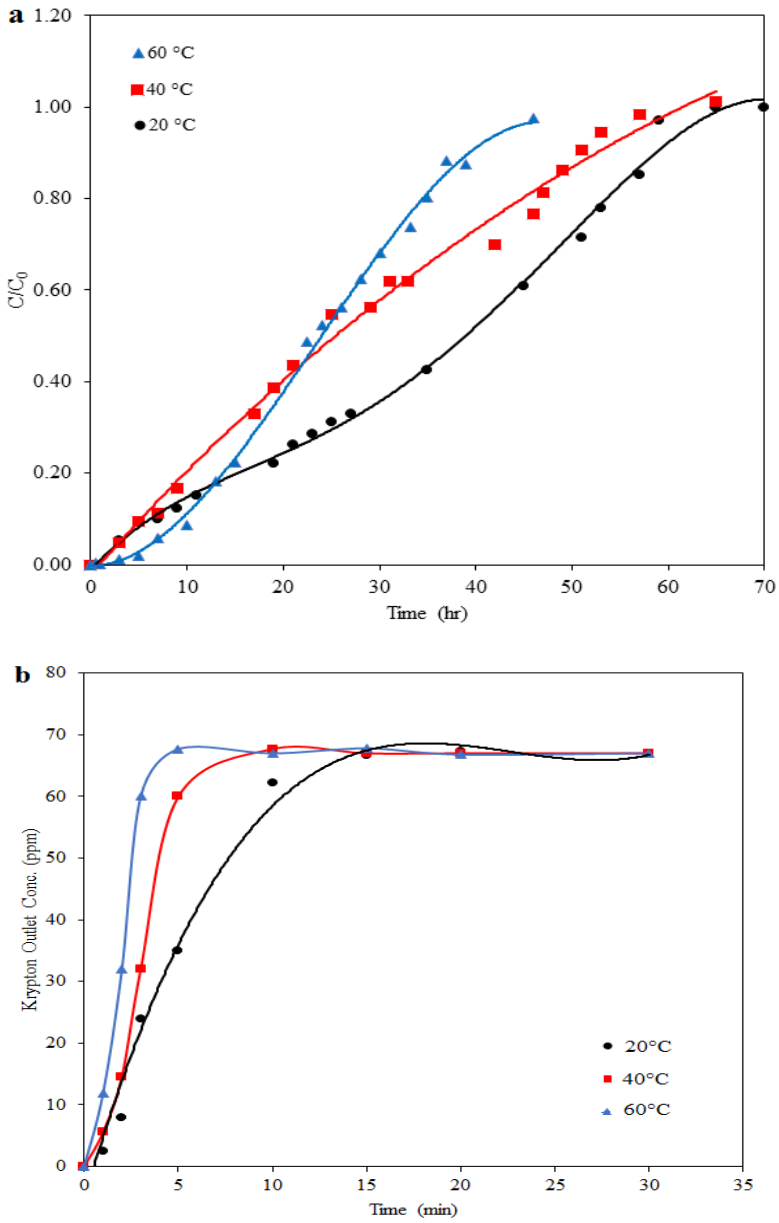

Figure 3.2.7: Effect of adsorption column temperature on (a) iodine and (b) krypton sorption from multicomponent gas stream
(Total gas flow – 180 mL min^{-1}; iodine concentration – 25 ppm; Kr Concentration - 70 ppm; carbon loading – 10 wt% C@ETS-10; amount of sorbent – 2.5 g)

Calculated iodine sorption capacity at different temperatures is shown in Figure 3.2.8. The decreasing trend is thermodynamically consistent for the exothermic adsorption process.

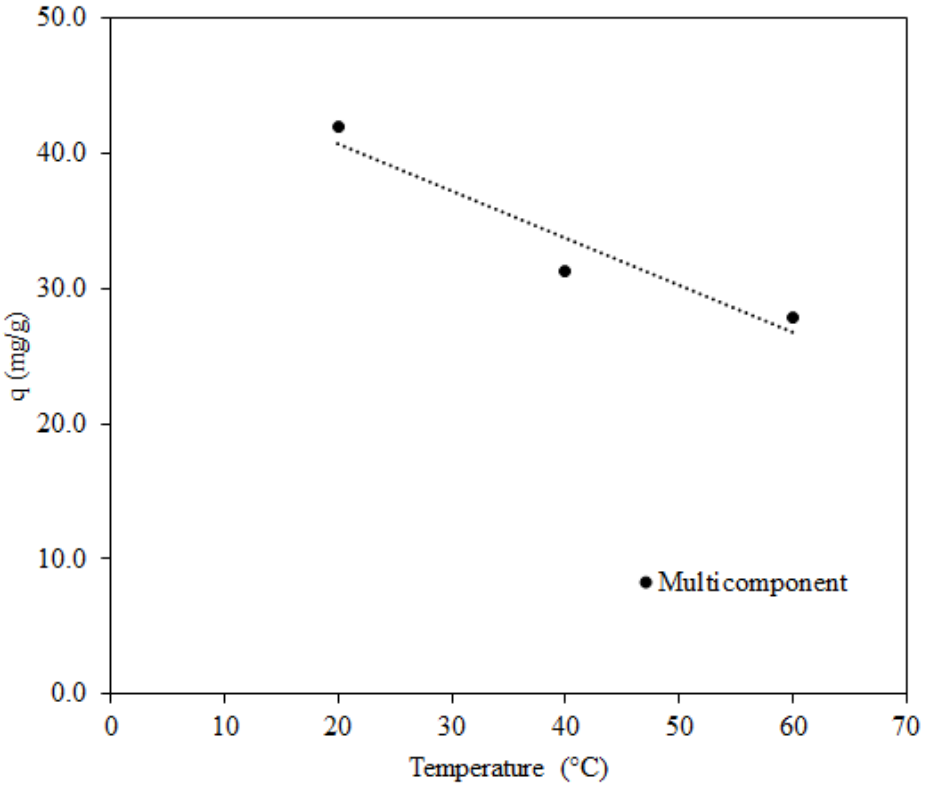

Figure 3.2.8: Effect of adsorption column temperature on capacity of 10wt% C@ETS-10 from multicomponent gas stream

3.2.3.4 Characterization of used sorbent

SEM: Surface morphology of 10 wt % C@ETS-10 pellet before and after sorption. SEM micrographs were obtained using a LEO SUPRA 35VP FE-SEM. Both the samples appeared nonporous at high magnifications (Figure 3.2.9). The morphology of the used sample showed globular deposits not present on the fresh sample which may be the adsorbed iodine. No differences were noticed between the morphology of the single contaminant, I_2 (*Annual report 2015*), and multicomponent (I_2 & Kr) adsorbed samples. Iodine and krypton presence on the pellet was confirmed by EDS analysis (Figure 3.2.10). The spectra of the unused sorbent was collected with expected constituents (elements comprising the sorbent and sorbates). Identical spectra were recorded with the used pellet sample. Iodine abundance was noticed in the sample at 3.9 keV, indicating that iodine was present on the surface of the pellet at about 3.4 wt%.

However, krypton abundance could not be deduced from the spectra, indicating the limitation of EDS to detect the small amount of krypton molecules on sample.

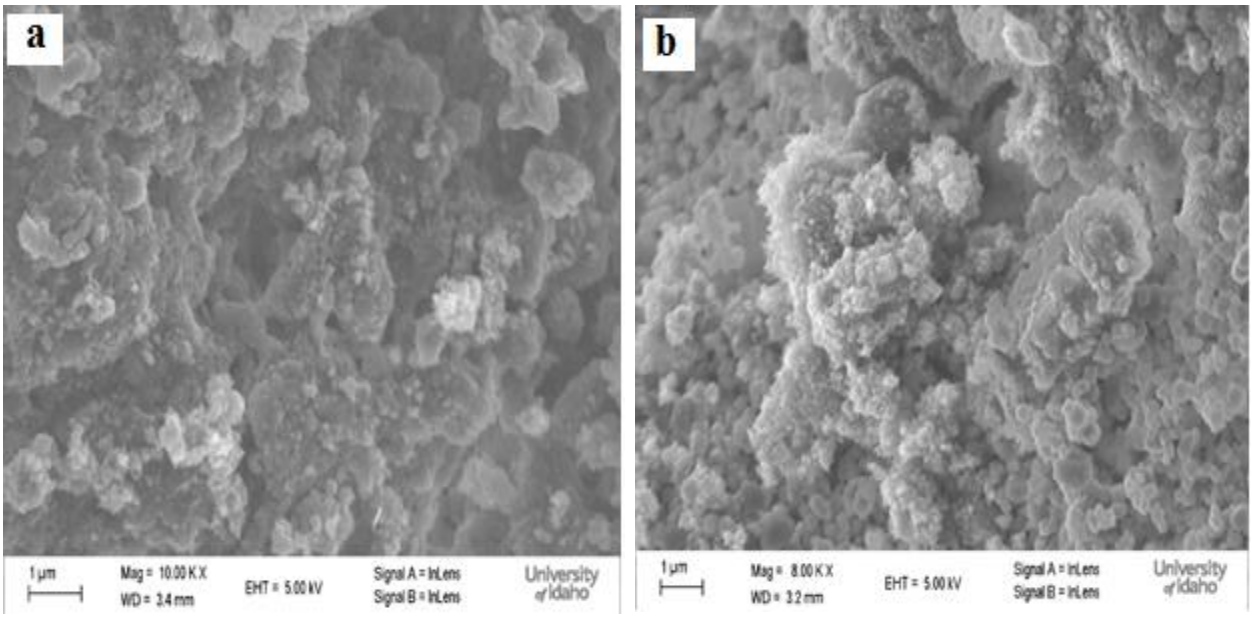

Figure 3.2.9: SEM images of 10 wt % C@ETS-10 pellet (a) before, and (b) after I_2 and Kr sorption at 20 ºC *(25 ppm iodine, 70 ppm Kr)*

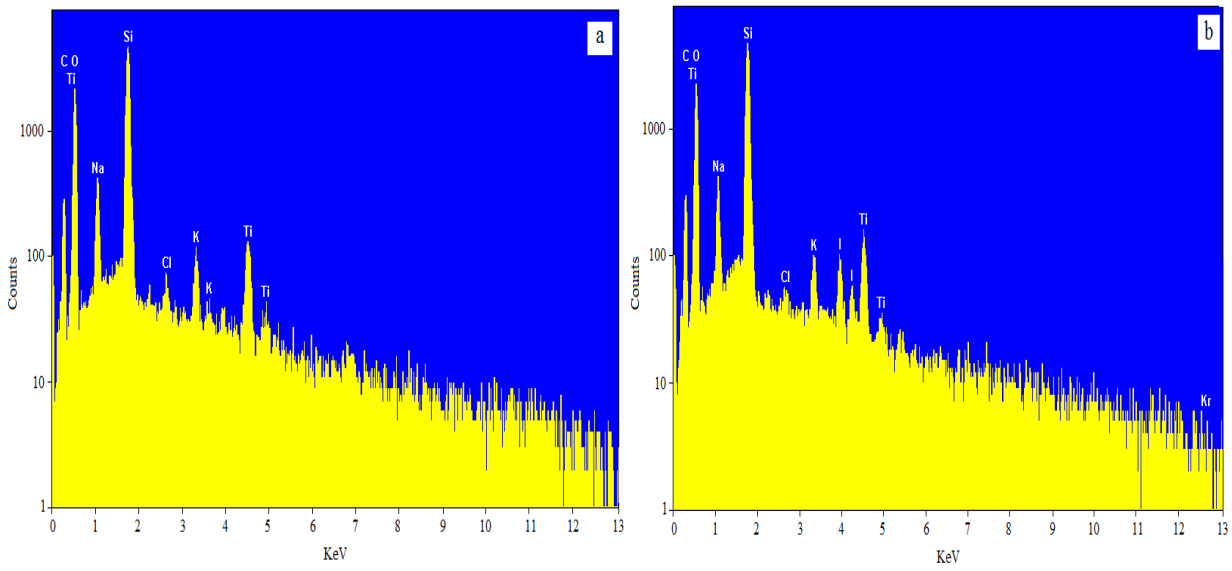

Figure 3.2.10: EDS spectra of (a) fresh, and (b) used 10 wt % C@ETS-10 pellet for iodine and krypton sorption at 20 ºC

***Raman*:** Raman spectra of samples were recorded using a WITec alpha300 Raman microscope (Ulm, Germany) with excitation at 532 nm. Figure 3.2.11 shows the difference between pristine and used 10 wt% C@ETS-10 pellet sample Raman spectra. The pristine C@ETS-10 sample shows the most intense peak for ETS-10 at 723 cm^{-1}, due to the stretching vibration of Ti-O-Ti of the TiO_6 structural group. The weak band observed in the range of 300 - 400 cm^{-1}, may be attributed to bending vibration of Si-O-Si and Ti-O-Ti fragments. Three major carbon peaks were observed in the sample for D-band (1332 cm^{-1}), G-band (1579 cm^{-1}), and 2D (2690 cm^{-1}). As shown in a previous report, the original powder sample of carbon nanoparticles shows that the peak of D-band was more intense than G-band and 2D, indicating long range disorder in the carbon nanomaterial. The iodine and krypton adsorbed/used sample shows the completely different spectra than the pristine sample. Only a small peak of ETS-10 was observed. Other peaks of ETS-10 and carbon were reduced due to adsorption of iodine and krypton on the sample. No other evidence was found in the used sample related to sorption of iodine and krypton.

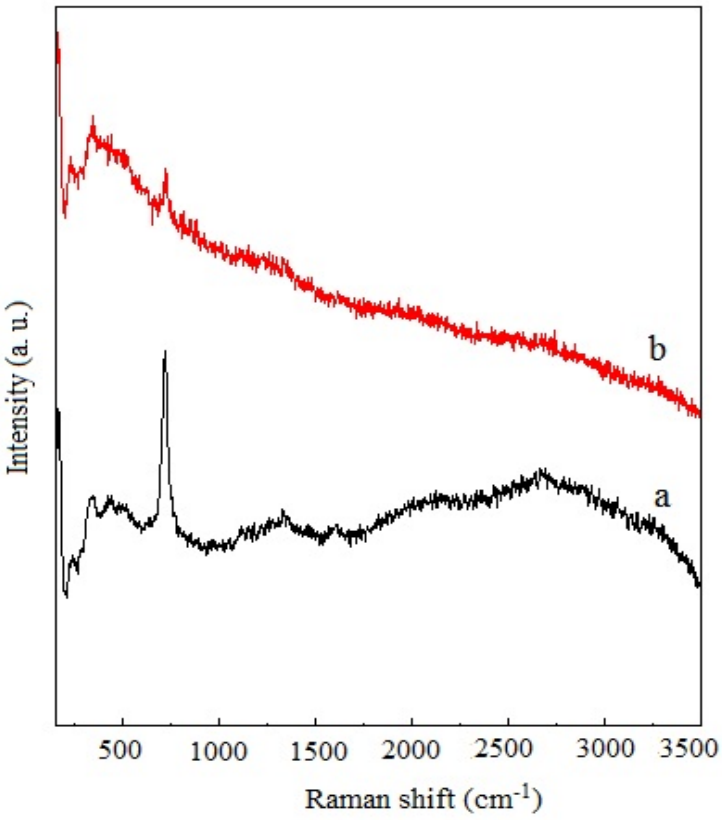

Figure 3.2.11: Raman spectra of (a) pristine, and (b) used 10 wt% C@ETS-10 pellet for multicomponent sorption

TGA. The thermal stability tests of pristine and used C@ETS-10 pellets were performed using STA 409 PC Luxx, Netzsch at rate of 10 ºC/min under argon atmosphere (Figure 3.2.12). The pristine sorbent pellet was dried overnight at 120 ºC before analysis to remove moisture from sample, therefore, no weight loss was observed from room temperature to 120 ºC. After this temperature, maximum 4 wt % weight was lost up to 600 ºC, possibly due to the dehydration of loosely bound water from ETS-10 structure and removal of water from pore of ETS-10. The total ~ 7 wt % weight loss was observed in the experiments with the used sample. The difference between weight losses of two samples could be attributed to the adsorbed iodine. At high temperature, surface and pore-sorbed iodine was removed from the sorbent. ~ 3 wt% weight was lost from the sorbent in the multicomponent experiment. Also, the small amount of iodine was lost during sample preparation for analysis.

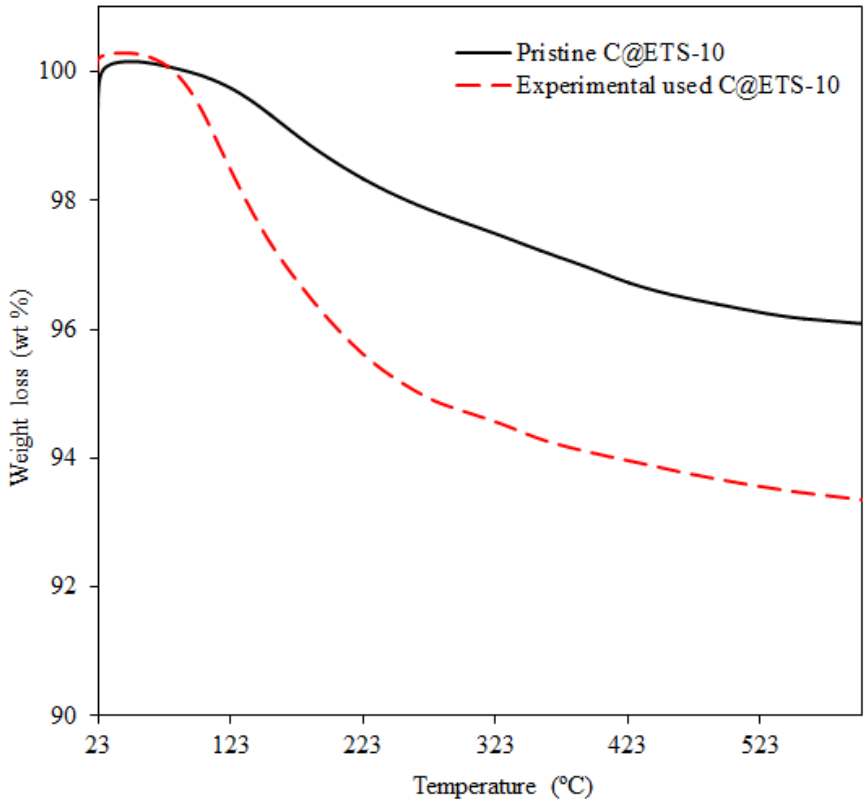

Figure 3.2.12: TGA of (a) pristine, and (b) used 10 wt% C@ETS-10 sorbent for multicomponent adsorption

***XPS*:** X-ray photoelectron spectroscopy (XPS) spectra of pristine and used samples were recorded by using ultra-high vacuum (UHV) chamber with a base pressure of 1.5×10^{-10} Torr. The chamber is equipped with an Omicron EA 125 hemispherical electron energy analyzer and a dual anode X-ray source. ETS-10 and carbon sharp peaks were noticed in pristine C@ETS-10 sorbent at binding energy 458.9 and 1072 eV, which were assigned for Ti $2p_{3/2}$ and Na1s (Lv, 2006). The C1s and O1s peaks were employed with high resolution at 284.6 eV and 532.6 eV binding energy, respectively (Datsyuk, 2008) (Figure 3.2.13a). The spectra of used sample show the existing and new peaks for iodine adsorption (Figure 3.2.13b), in which the characteristic peaks of iodine, $I3p_{1/2}$, $I3p_{3/2}$, $I3d_{3/2}$, $I3d_{5/2}$ and $I3d_{3/2}$ were clearly observed at binding energies (in eV) 930.7, 875.4, 630.8, 619.2 and 51.3, respectively (Scott, 2015). No evidence was found in the used sample related to capture of Kr, possibly due to the release of sorbed Kr molecules from the sorbent under vacuum conditions in the instrument before analysis.

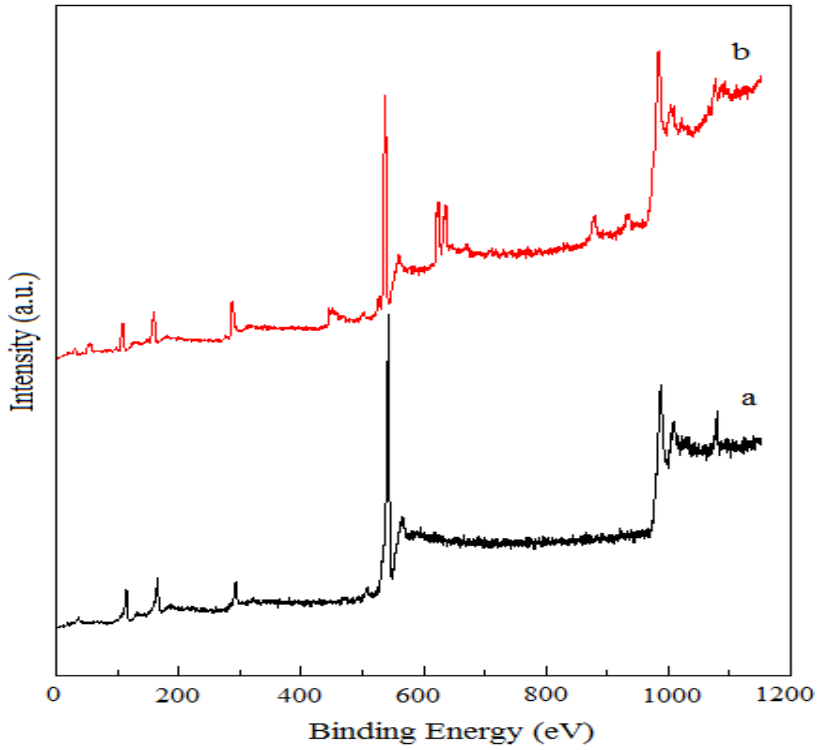

Figure 3.2.13: XPS spectra of samples (a) Pristine and (b) used 10 wt% C@ETS-10 sorbent for multicomponent (I2 and Kr) sorption at 20 °C

3.2.4 Modification of Experimental Setup to Allow Moisture in the Feed Stream

A Teledyne 50 SCCM mass flow controller (MFC) was connected to a flow split from the main N_2 gas cylinder and sparged flow through a bubbler filled with 100 mL of Millipore water. The stream was then added to a dry N_2 flow from an Aalborg 1000 SCCM MFC. Flow from an Aalborg 50 SCCM MFC containing 1000 krypton balanced with N_2 was flowed through a water-jacketed iodine vaporizer, adding iodine to the stream, and added to the overall flow. The experimental setup is shown in Figure 3.2.14.

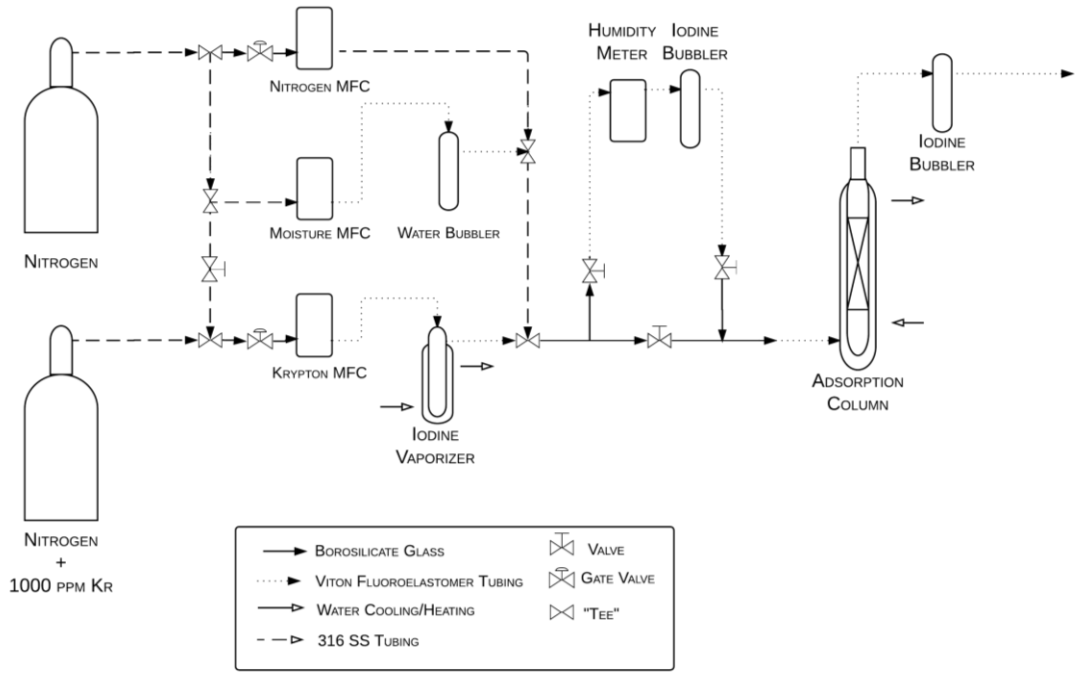

Figure 3.2.14: Experimental setup for off-gas contaminant adsorption including moisture addition

The flow rates from the three MFCs were adjusted to create a stream containing 25 ppm iodine, 70 ppm krypton, and 5-90% relative humidity (RH). All experiments were performed holding the adsorption column at 25 °C.

Figure 3.2.15 shows the breakthrough curves for dry and 90% RH gas streams.

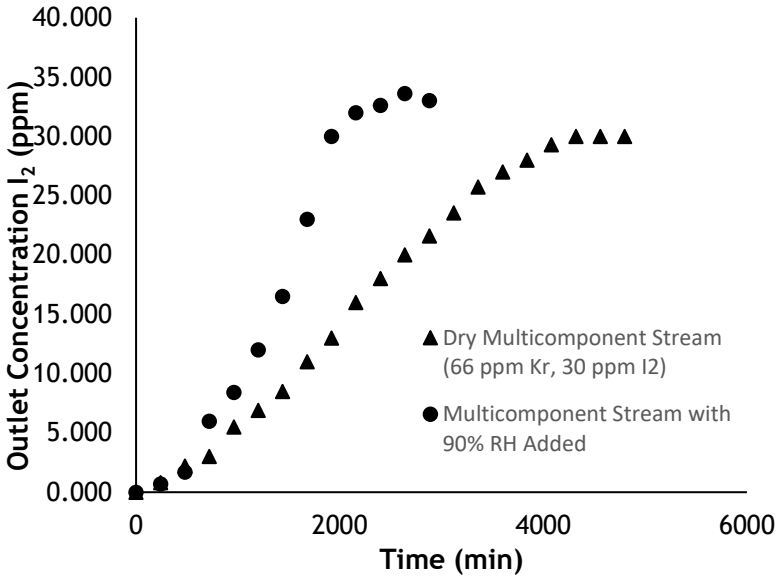

Figure 3.2.15: Breakthrough curve for iodine sorption on 10 wt% C@ETS-10 in a multicomponent (25 ppm iodine, 70 ppm krypton) stream including moisture at 90% RH

High moisture content of 90% RH was shown to have a substantial effect on the adsorption of iodine, decreasing SC by 28.4% from 41.5 mg/g in a dry stream to 29.7 mg/g in a stream of 90% RH. This decrease shows that the active surface of the sorbent is made inaccessible to iodine by moisture, which either competes for active sites or blocks pores through condensation.

The hypothesis of inhibition of iodine sorption on C@ETS-10 by water was further supported by running an experiment with 0% RH and intermittently adding moisture to the inlet stream. After each introduction of 90% RH into the off-gas stream, the outlet concentration of iodine increased by 3-6 ppm, whereas the outlet concentration in the dry stream increased by only 0.1-0.9 ppm in the same total experiment time, indicating that the addition of water inhibited the adsorption of iodine. The breakthrough curves for the intermittent addition of moisture are shown in Figure 3.2.16.

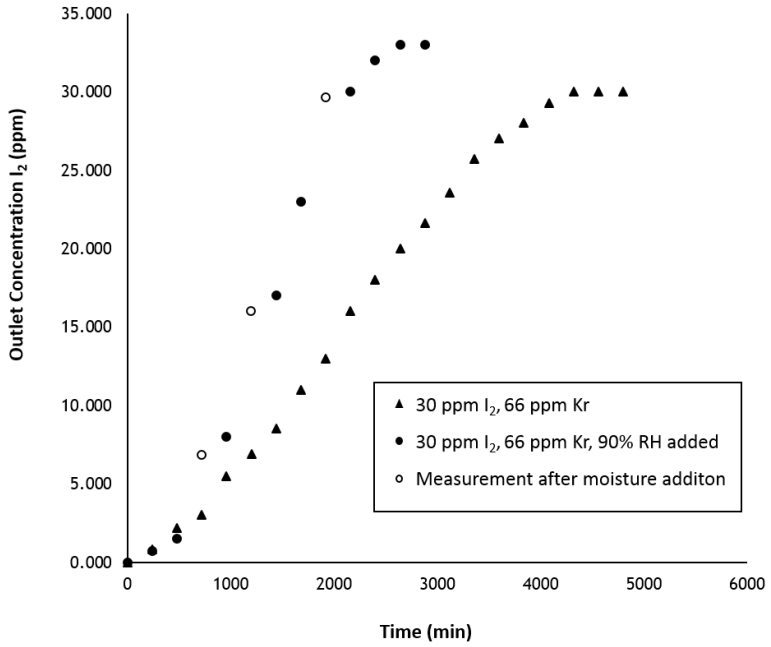

Figure 3.2.16: Effect of intermittent moisture addition in a multicomponent stream to the adsorption of iodine on 10 wt% C@ETS-10 sorbent

The effect of 90% RH on krypton SC was not as severe. SC for the dry multicomponent stream was 0.1214 mg/g compared to 0.1164 mg/g for a 90% RH stream, decreasing the capacity only 4.1%, as shown below in Figure 3.2.17.

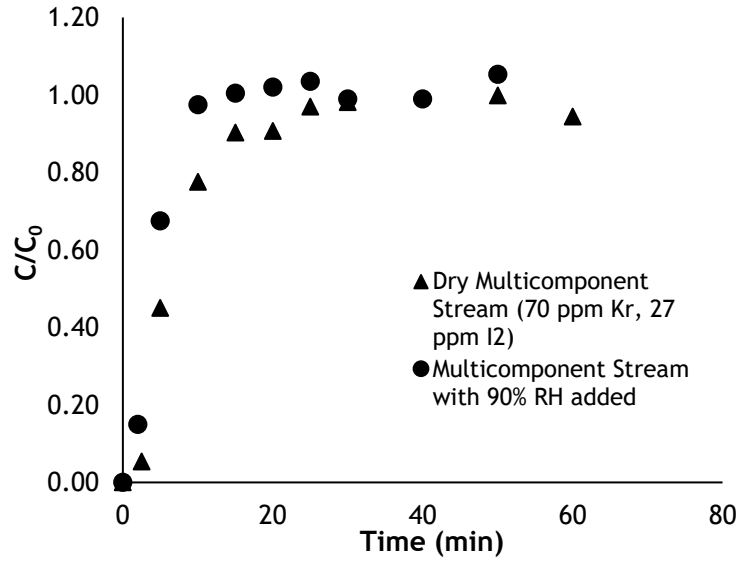

Figure 3.2.17: Breakthrough curve for krypton sorption on 10 wt% C@ETS-10 in a multicomponent (25 ppm iodine, 70 ppm krypton) stream including moisture at 90% RH

The effect of moisture on the adsorption capacity of iodine at other RH values is shown in Figure 3.2.18. Sorbent capacities (SC) for iodine in the moist stream were calculated from the generated breakthrough curves shown in Fig. 3.2.18, and are listed in Table 3.2.1.

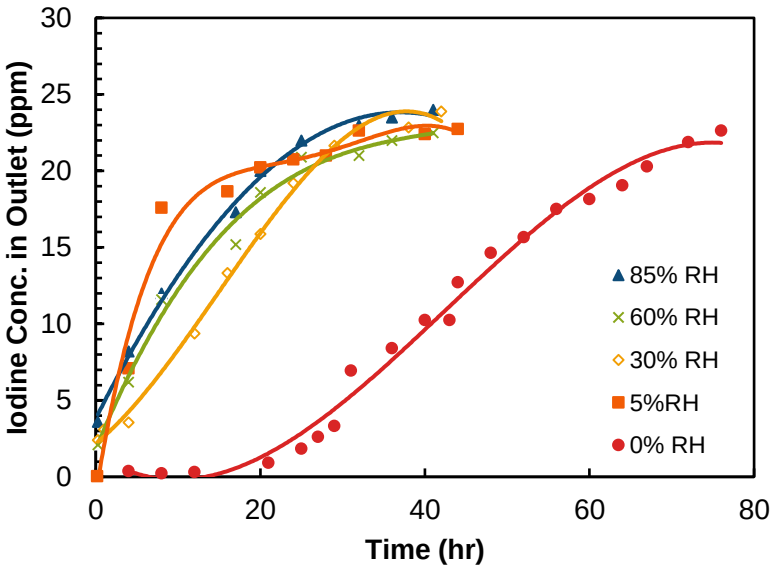

Figure 3.2.18: Breakthrough curves for iodine sorption on 10 wt% C@ETS-10 in a multicomponent (25 ppm iodine, 70 ppm krypton) stream including moisture from 5-85% RH

Table 3.2.1: Iodine sorption capacities for 10 wt% C@ETS-10 with moisture addition

Relative Humidity	q ($mg\ I_2/g_{sorbent}$)
85%	15.3
60%	18.1
30%	20.4
5%	18.1
0%	40.5

Introducing moisture into the simulated off-gas stream even in small amounts had a significant effect of the 10 wt% C@ETS-10, reducing capacity 50% from 41.5 mg/g with no moisture added to 20.3 mg/g at 30% RH. (The 5% data point is most likely an outlier). However, higher RH further reduced the capacity only 12% more, with iodine sorption capacity decreasing to 15.3 mg/g at 85% RH. This decrease shows that the active surface of the sorbent is made inaccessible

to iodine by moisture, which either competes for active sites or blocks pores through condensation.

3.3 Summary of Results

The findings of the experimental sorption studies can be summarized as following:

1. The continuous column experimental setup is effective for conducting dynamic sorption studies on gas streams containing single and multiple components as well as moisture.
2. The ETS-supported nanostructured carbon sorbent (C-ETS) developed in these studies was more effective than other sorbents for the capture of contaminants under investigation.
3. The optimum carbon loading on ETS-10 was 10%.
4. The sorption capacity increases with decreasing temperature, consistent with the predictions for an exothermic process.
5. Increasing the empty bed contact time seems to mitigate the channeling/maldistribution issues with the feed gas, leading to a better contact and higher sorption capacity.
6. The presence of another component results in the reduction of sorption capacity for a component.
7. Characterization of fresh and used sorbent indicates the presence of captured iodine. The conditions used in the characterization techniques are likely resulting in the removal of sorbed krypton.
8. Introducing moisture in the gas stream results in the reduction of sorption capacity. However, the sorbent does seem to retain sufficient operational capacity.

4 Immobilization of Contaminants

4.1 Introduction

A ceramic sleeve-lid type of container was considered for enclosing the loaded sorbent to isolate the contaminants from the environment. Initial work for immobilization utilized celite powder shaped into the form of a sleeve, and subsequent work utilized alumina tubes procured from commercial vendors.

4.2 Preparation and Characterization of Celite Sleeve

A cylindrically shaped sleeve (Height – 26 mm; ID – 15 mm; OD – 19 mm; Thickness of edge – 2 mm) was prepared using celite powder. In a typical procedure, 4 g of celite powder (Sigma Aldrich, USA) was mixed with appropriate amount of Ludox HS-40 colloidal silica (Sigma Aldrich, USA) to make a thick paste. The resulting mixture was stirred manually at room temperature for another 20 min. The cylindrical shape sleeve was obtained by filling with it the annular space between an HDPE solid piece and a 3-mm thick PVC pipe. Another HDPE disc was used to press the material. This system was allowed to dry for 30 min in air. Following air drying, the sleeve was maintained in a furnace at 900 ºC for 12 h.

The surface morphology of the fabricated sleeve (celite powder) was analyzed by scanning electron microscopy (SEM) as shown in Figure 4.2.1. The images of low and high magnification indicates the porous nature and rough surface of the sleeve. Fabrication process involving manual pressing of the material does not appear to yield a strong and nonporous sleeve. Therefore, other analysis was not performed with the existing sleeve. It was decided to not continue with this approach of formulating a custom sleeve from ceramic powder. Instead commercially available nonporous hard celite (~ 98% Al_2O_3) sleeve and lid (1.2” height and 0.9” OD) was procured from AdValue Technology (Tucson, Arizona), USA for further trials.

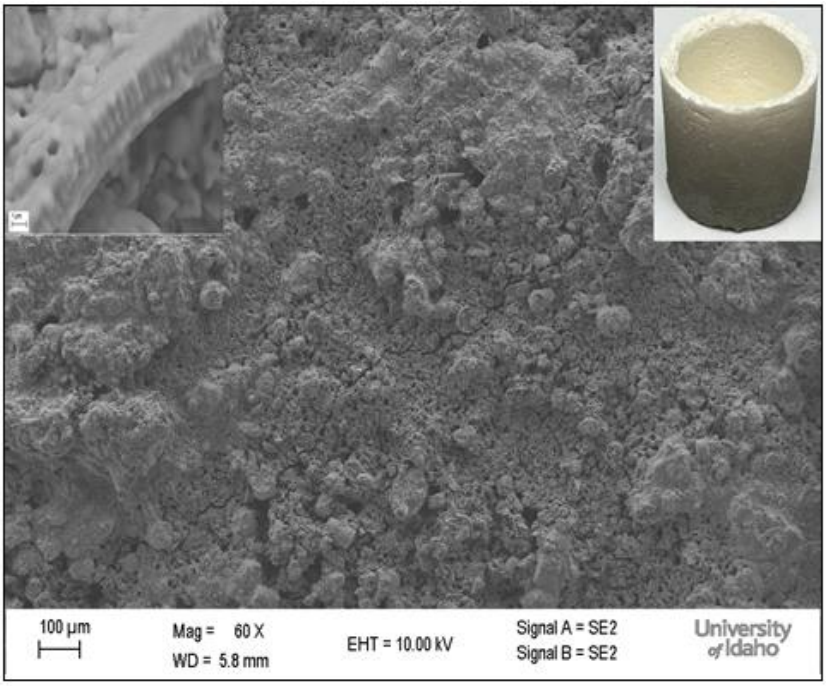

Figure 4.2.1: SEM image and photograph of prepared celite sleeve

4.3 Alumina Sleeve & Lid

Figure 4.3.1 shows the schematic diagram of a ceramic (98% Al_2O_3) sleeve and lid procured from AdValue Technology, USA for use as a containment device. This material was selected due to its physical properties such as hardness and low porosity (less than 10%). The shape and dimensions of the sleeve and lid are shown in Figure 4.3.1a-c.

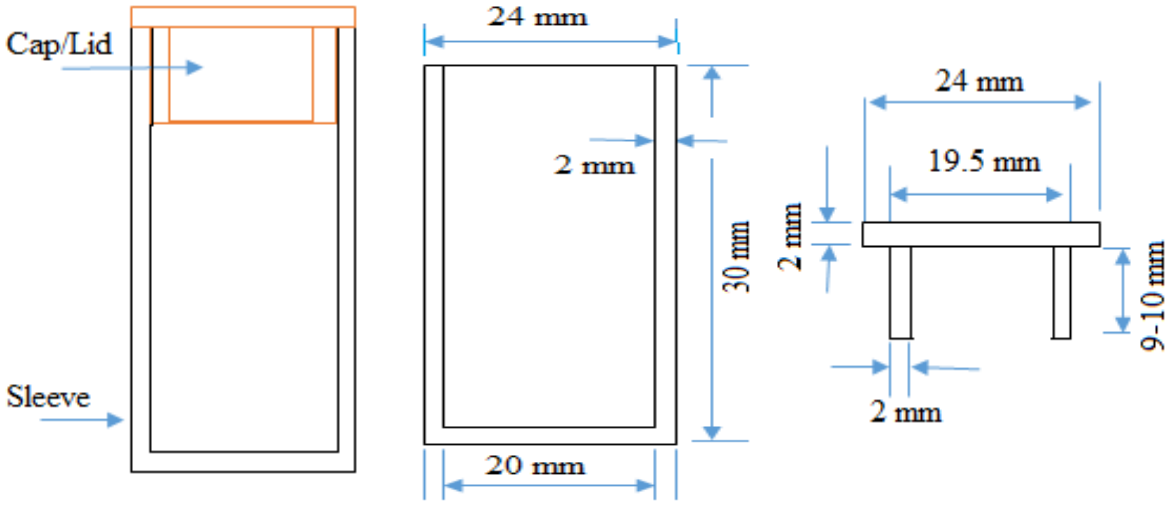

Figure 4.3.1: Schematic diagram of ceramic (a) sleeve and lid (b) sleeve (c) lid

4.4 Carbon coating on sleeve and lid

The ceramic sleeve and lid were coated with pyrolytic carbon (PyC) by isothermal chemical vapor deposition (CVD) method. A 3-inch OD, 4 feet long quartz tube was placed in a high temperature electrical furnace (Lab-Temp, Kittanning, PA). The ceramic sleeve and lid were washed with acetone and placed in this quartz tube as shown in Figure 4.4.1. In a typical procedure, impurities were driven out from the sleeve/lid by preheating (30 min) them before raising the furnace temperature to 900 °C. Then a known quantity of carbon source (tire pieces - 130 g and clay 8 g) was quickly inserted from one of the end of quartz tube. The carbon deposition on the ceramic sleeve and lid was carried out for 15-20 min in an inert nitrogen atmosphere. The furnace was allowed to cool down naturally, and the coated product was washed with propanol to remove any organic impurities. Photograph of before and after PyC coated sleeve and lid is shown in Figure 4.4.2.

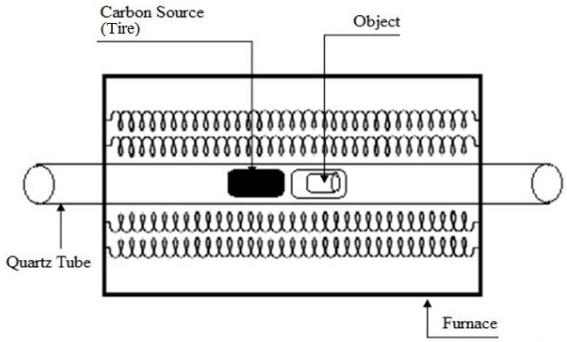

Figure 4.4.1: A schematic diagram of quartz tube furnace for PyC by chemical vapor deposition

(a) (b) (c) (d)

Figure 4.4.2: Photograph of sleeve and lid (a-b) before (c-d) after PyC coating

The surface morphology before and after PyC coating sleeve was analyzed by FE-SEM (LEO SUPRA 35VP). Figure 4.4.3a & b show the SEM images of ceramic sleeve before PyC coating. The polyhedron structure of alumina particles was noticed on the surface of sleeve which appears rough. The surface exhibited a presence of small pores 100 – 200 nm in diameter (not shown in SEM images). The surface morphology of PyC coating sleeve is shown in Figure 4.4.3. The small polyhedron structure of carbon particles (1-3 μm) was complete covered the surface of ceramic sleeve (Figure 4.4.4 a & b). The thickness of carbon layer on sleeve was around 550-650 μm (Figure 4.4.4 c). The elemental analysis of as received and PyC coated sleeve was performed using EDS. EDS spectra of as received sleeve shows only Al, O and C on surface (Figure 4.4.5a). EDS spectra of PyC sleeve shows the maximum amount of carbon and small amount of impurity such as sulfur (S), Na, Zn, attributable to the use of shredded tire pieces as carbon source (Figure 4.4.5b).

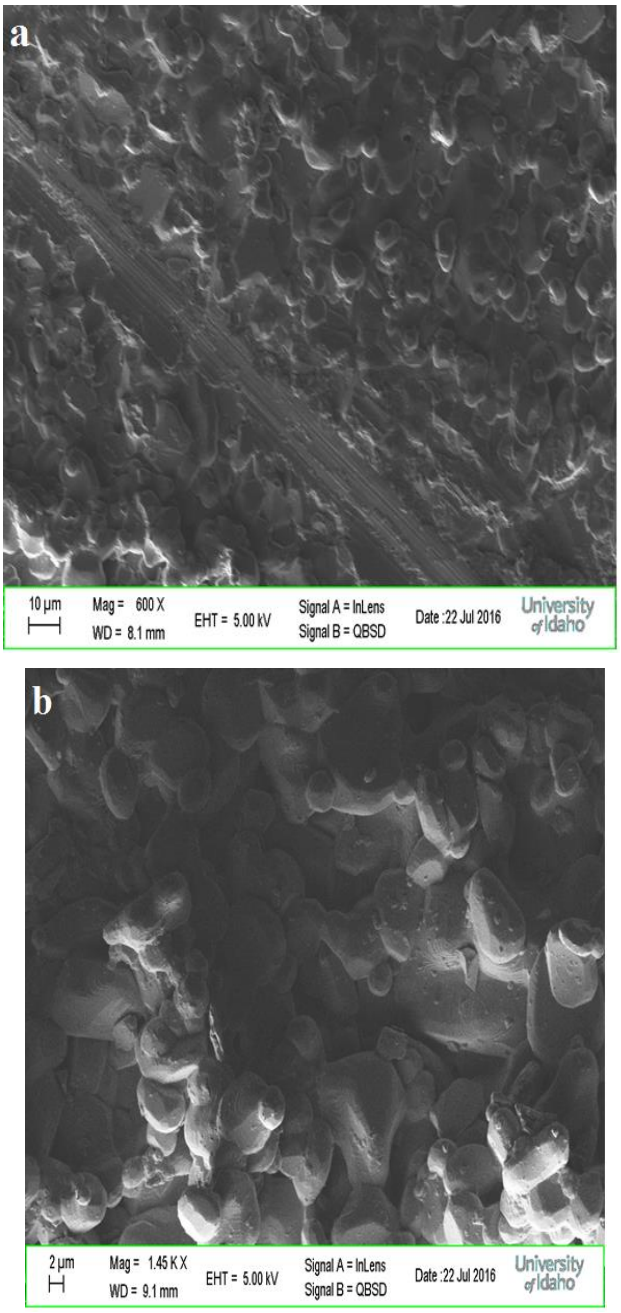

Figure 4.4.3: SEM images of sleeve surface before PyC (a) low (b) high magnification

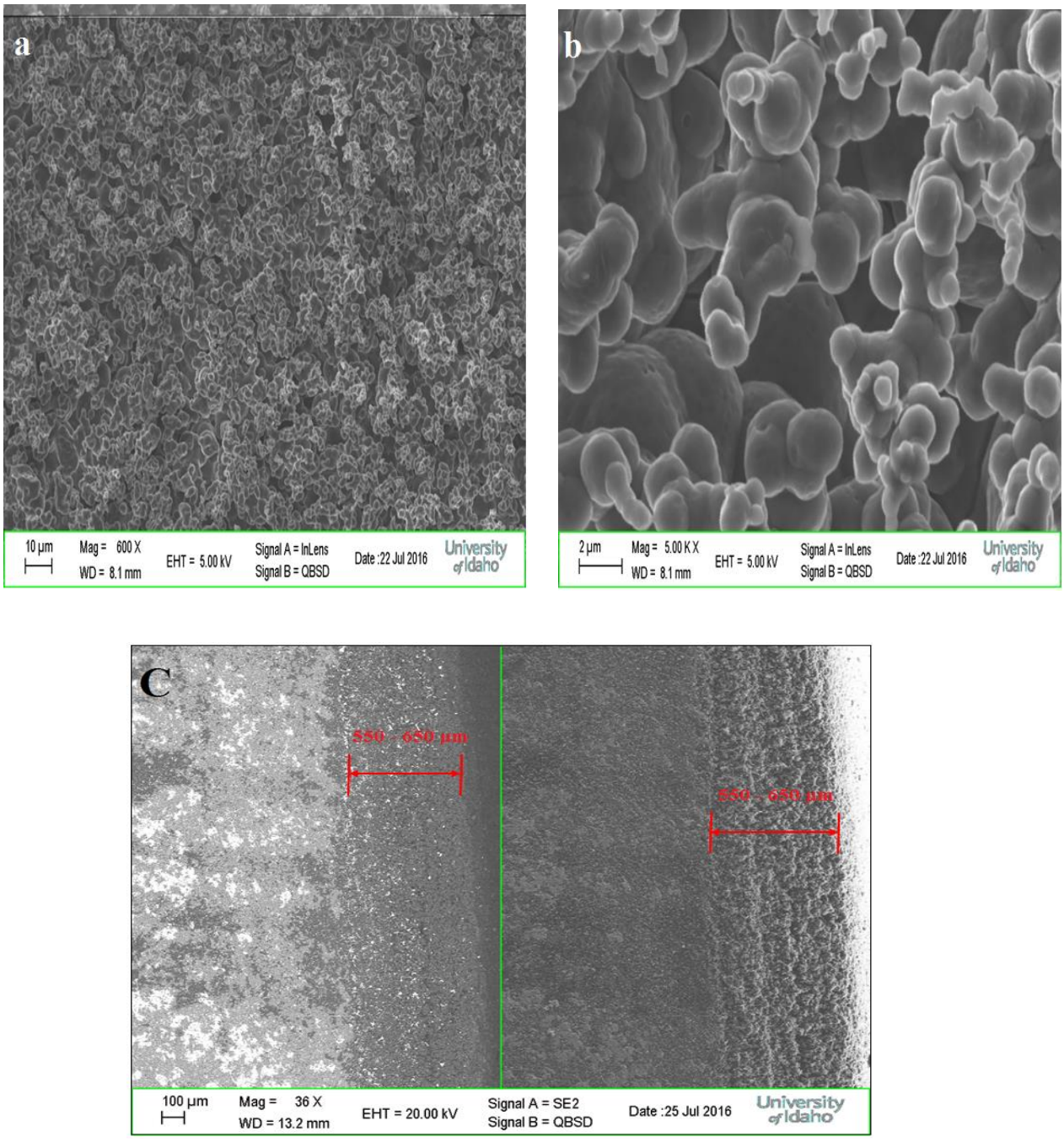

Figure 4.4.4: SEM images of sleeve after PyC coating (a) low (b) high magnification (c) actual size of carbon layer on sleeve

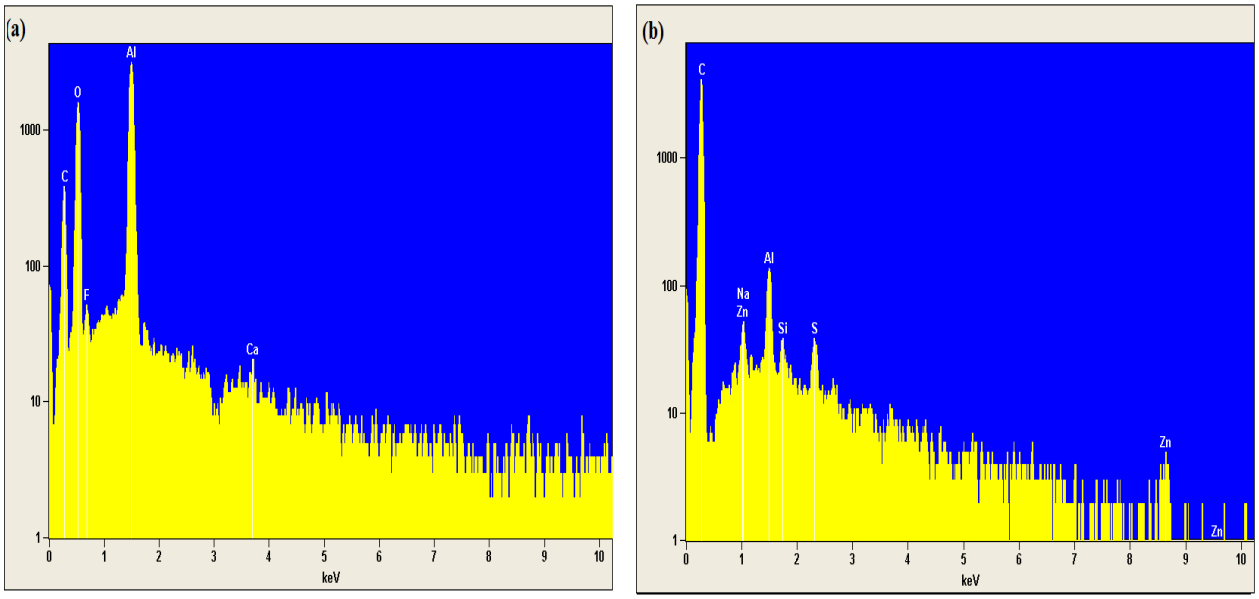

Figure 4.4.5: EDS spectra of sleeve (a) before (b) after PyC coating

4.5 SiC coating on carbon layer of ceramic sleeve and lid

Figure 4.5.1 shows the schematic diagram for synthesis of SiC coating on sleeve and lid by CVD based on the technique described by Haibo et al (2008). The experiment was performed using long ceramic tube (1.5 inch OD, 3 feet long), fixed into a high temperature furnace (Thermolyne OV-11, Thermo Scientific). Inert gas (argon - 5 mL min^{-1}) was purged through one of the end of the tube to carry the silicon vapor over the target. The mixture of SiO_2 and Si powder (Sigma Aldrich, USA) was placed in the boat. The molar ratio of the Si and SiO_2 was about 1.2. Subsequently, the carbon coated ceramic sleeve was placed into the boat after the source in the middle of tube and furnace was heated upto 1600°C. The furnace was held at 1600°C to 4 h, then, it was allowed to cool naturally. The coated product was washed with acetone to remove organic impurities.

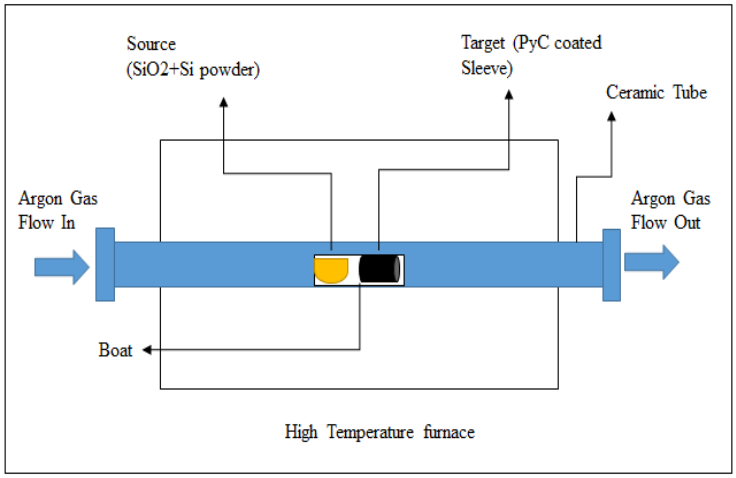

Figure 4.5.1: Schematic diagram of tube furnace set up for SiC by chemical vapor deposition

The surface morphology of SiC coated sleeve was analyzed using FE-SEM (LEO SUPRA 35VP). SEM image of SiC coated on ceramic sleeve is shown in Figure 4.5.2a. The surface of PyC coated ceramic sleeve was rough and numbers of micro-sized SiC granules were deposited on the surface of sleeve. It was observed that the surface of sleeve was not completely covered by SiC; possibly 4 h sample holding time in furnace was not enough to form a uniform layer of SiC on sleeve. Figure 4.5.2b shows the EDS pattern of the SiC coating on sleeve. Silicon, carbon and alumina were presented on the surface of sleeve.

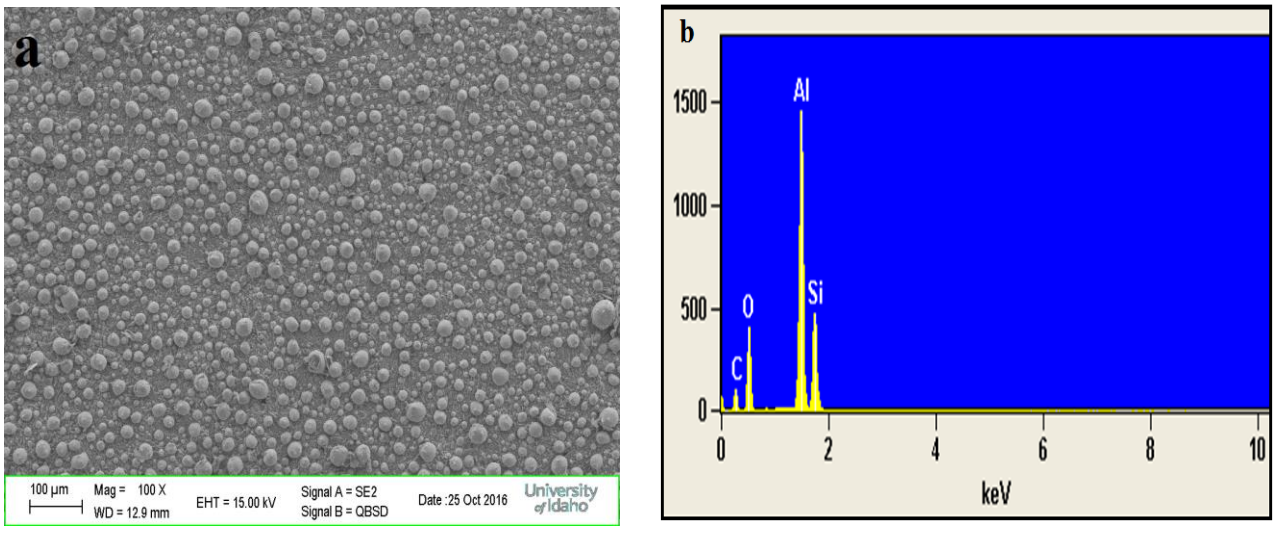

Figure 4.5.2: (a) SEM image and (b) EDS spectra of SiC coating on PyC ceramic sleeve

SiC coating experiments were repeated for different time durations (heating time: 6 and 8 h) to provide the uniform coating of Si layer on carbon deposited ceramic sleeve. Both the experiments were performed at 1600 ^{o}C using high temperature tube furnace under argon gas flow. It was observed that carbon was burned/removed from the surface of the ceramic sleeve in both runs and silicon layer was not deposited on ceramic sleeve. Therefore, to eliminate the existing issues the subsequent SiC coating experiments will be performed using high temperature vacuum furnace. Detailed procedures subsequently followed are described below.

The alumina substrate was first washed with acetone. Carbon coating was conducted in a Lindberg type 54352 tube furnace at 900^{o}C using kaolin coated tire shreds as a source of carbon. Kaolin was not used in the initial trials, but after being used in the subsequent trials, was judged visually to yield superior results and was used in all subsequent trials. The quantities used were ~40g tire shreds and 1.5-1.6g kaolin. The alumina substrate consisted of either an alumina sleeve ~1in tall or one or more thin sheets of alumina, 1-2 inches long.

The alumina substrate was placed in the cool furnace in a dish in such a way to maximize exposed surface area. Nitrogen at a flow rate of 0.65 SCFH was passed through the tube during the entire coating step. Starting from room temperature, the oven was then heated up to 900^{o}C in just over an hour. After reaching this temperature, the tire shreds were added. The temperature was maintained for few minutes until negligible off gas was observed at the outlet based on the color, and the furnace was turned off. The tube was allowed to remain in the furnace for about 15 minutes to cool. The tube was then removed from the furnace, and allowed to cool an additional 15 minutes resting, the alumina substrate was removed. After the alumina substrate was completely cool, it was washed with propanol.

The SiC coating was performed in a SentroTech model number STT-1700C-1.5-6 tube furnace at 1500^{o}C, as shown in Figure 4.5.3. In all trials, the carbon coated alumina was placed in the furnace with Si and SiO_2 powder. Roughly a 1:2 molar ratio of Si:SiO_2 was used, with 3-4g total powder used. The furnace was evacuated and then heated up at 2.5^{o}C/min with the tube being sealed until the temperature reached 1100^{o}C. The vacuum was then turned off to trap the

gases in the tube with the alumina for the remaining heating time, the bake time of 4 hours, and the cool off time of 10 hours.

Initially, the Si and SiO_2 powder were kept in the same container, but in separate piles. This did not yield the dark coating expected, it instead yielded a light gray coating. Next, the powders were mixed together. This too did not yield the expected results. Finally, coating the same piece twice (i.e. carbon->silicon->carbon->silicon) with the powders mixed; this still did not yield the expected results. Visual analysis of the coated alumina suggested that the carbon coating came off in the furnace, as the coating looked like the coating on alumina that had been in the silicon furnace without carbon (used as supports to maximize surface area of pieces being tested).

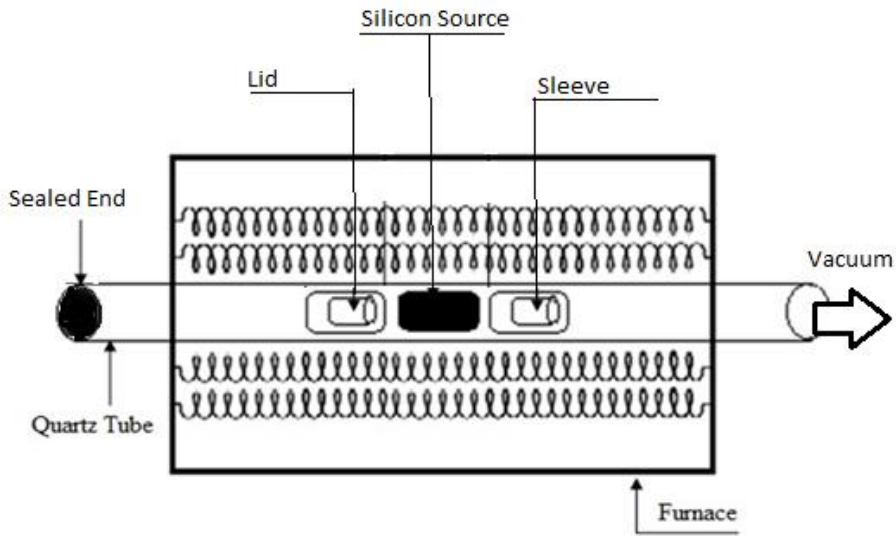

Figure 4.5.3: SiC Coating Setup

In order to test the hypothesis that carbon coating is being stripped off due to high temperature and vacuum conditions, decoating experiments of carbon coated alumina were initiated at 1100^{o}C (with no Si or SiO_2 present) both under vacuum and argon flow.

The first experiment was an attempted removal under vacuum at 1100^{o}C. Carbon coated alumina was inserted in the furnace shown above, and heated to 1100^{o}C over 500 minutes (heating rate ~2.2 ^{o}C/min). Then it was held at 1100^{o}C for 240 minutes and allowed to cool in the furnace for 500 minutes. Vacuum was applied continuously throughout the duration of the

test. Examination of the specimen indicated a complete removal of carbon from the alumina. The second experiment was conducted under the same temperature conditions, however, with a continuous argon flow during the process. This resulted in no change to the physical appearance of the carbon coated alumina.

The comparison of the two experiments pointed to the application of vacuum as the cause of removal of the carbon coating. To eliminate high temperature as a cause of decoating, another experiment was conducted under argon flow, however, the temperature was raised to 1600^{o}C over 640 minutes, followed by holding it at that temperature for 240 minutes, and subsequent cooling. This resulted in no change to the physical appearance of the carbon coated alumina.

The conclusions from these experiments suggest that the reason for the carbon removal in the SiC coating was a result of the vacuum applied during the process.

Subsequent experiments were conducted for SiC coating on the pyrolytic carbon coated sleeve in the SentroTech furnace at 1500^{o}C under argon flow of 50ml/min). The carbon coated alumina was placed in the furnace with Si and SiO_2 powder mixed together. Roughly a 1:2 molar ratio of Si:SiO_2 was used, with 3-4g total powder used. The furnace was then heated to the bake temperature of 1500^{o}C using a heating rate of 2.5^{o}C/min, and then held at the high temperature for 4 hours. The furnace was switched off and the tube cooled off over 10 hours in argon flow.

Figure 4.5.4 shows an SEM of the specimen subjected to SiC coating. Two distinct regions can be seen in the micrograph, with a globular one similar to those of the pyrolytic carbon coating, while the second region showing a pillar-sheet type elongated regular structure.

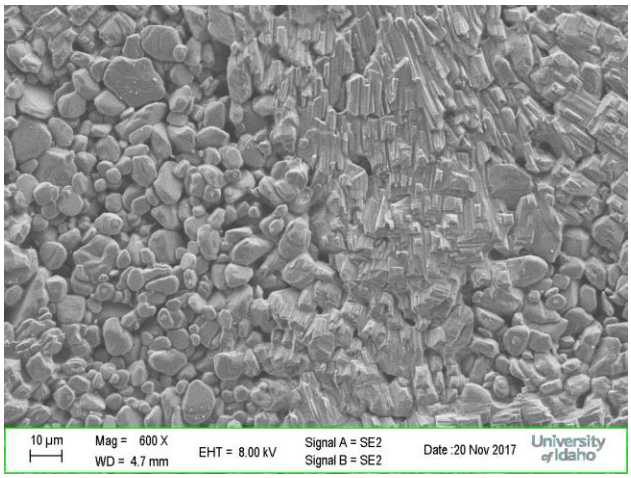

Figure 4.5.4: SEM Image of Specimen subjected to SiC Coating

EDS spectra of the specimen were taken focusing on two different spots in these two regions and are shown in Figure 4.5.5.

(a)

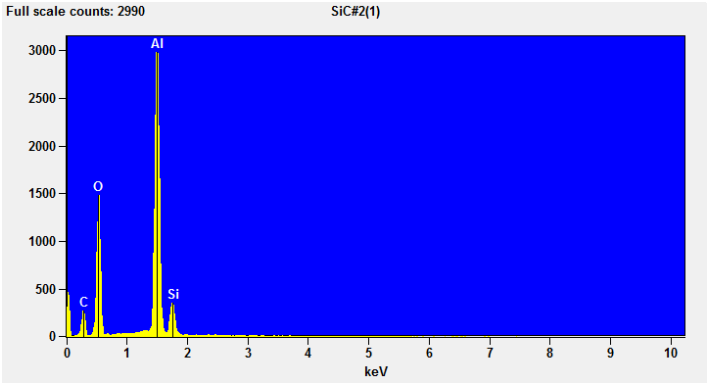

(b)

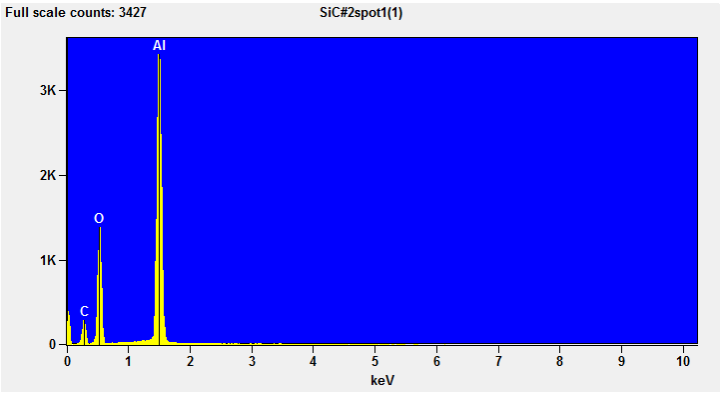

(c)

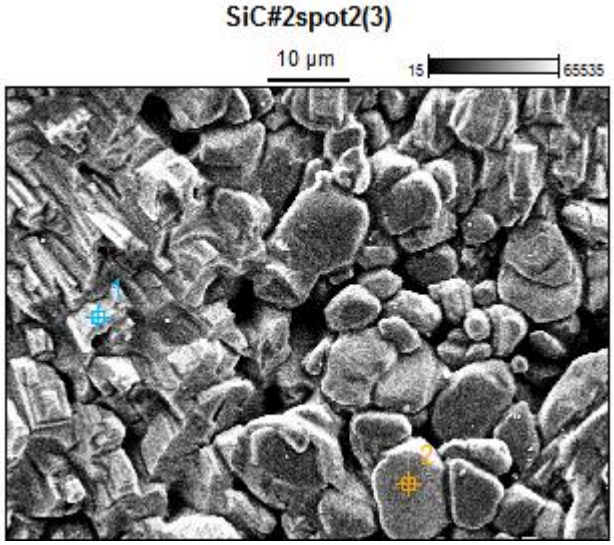

Figure 4.5.5: EDS Spectra of the SiC coated Specimen; (a) Spectrum at Location #1, (b) Spectrum at Location #2, (b) Position of the Two Locations on the Specimen Surface

It can clearly be seen that both Si and C were detected in Location #1, while only C was found in Location #2. It appears that SiC was deposited at Location #1 but not at #2. The presence of SiC can be directly correlated to the structural formation.

4.6 Summary and Recommendations for Future Work

The proposed immobilization strategy shows considerable promise for isolation of sorbed contaminants. The sorbate-sorbent matrix can be enclosed in inert ceramic container that can be coated with successive layers of pyrolytic carbon and silicon carbide. Coating the ceramic with carbon was found to be relatively straightforward, however, some difficulties were encountered while attempting to coat the carbon-coated material with SiC. Manipulation of reaction conditions resulted ultimately in successful deposition of SiC on carbon coated matrix, although the coating was not uniform.

Further work needs to be conducted to optimize the coating conditions for SiC coating. The furnace available and used in this work limits the exposure of the specimen to be coated to the SiC vapor. New configurations need to be investigated with superior equipment to enable uniform coating. Detailed characterization of the substrate including structural integrity determinations need to be conducted. Optimization of operating conditions (temperature, duration) also need to be investigated. Finally, container design needs to be developed for maintaining the integrity of isolation with any pressure or component build-up resulting from desorption or radioisotope decay.

5 Mathematical Modeling of Sorption Process

5.1 Theoretical Principles

5.1.1 Adsorption Equilibrium

Adsorption equilibrium is usually described by adsorption isotherms that relate the concentration of contaminant in the bulk gas, *C*, to the adsorption capacity of the adsorbent at equilibrium, q_e. One of the simplest thermodynamic models for adsorption is the Langmuir isotherm, with the basic assumptions (Langmuir, 1918):

1. Molecules of adsorbate are adsorbed on a fixed number of sites.
2. Each site may hold one adsorbate molecule.
3. All sites have equal affinity for the sorbate
4. There are no interactions between adsorbed molecules.

The Langmuir model can be derived by balancing the rates of elementary adsorption and desorption reaction steps (Langmuir, 1918):

Rate of adsorption

$$r_{ads} = k_a C(1 - \frac{q_e}{q_m}) \tag{5.1.1}$$

Rate of desorption

$$r_{des} = k_d \left(\frac{q_e}{q_m}\right) \tag{5.1.2}$$

Where k_a and k_d are the kinetic rate constants of adsorption and desorption, respectively; *C* is the bulk concentration of contaminant; q_e is the amount of contaminant adsorbed in equilibrium with *C*, and q_m is the maximum capacity of the sorbent. Equating the two rates at equilibrium,

$$q_e = \frac{q_m K_L C}{1 + K_L C} \tag{5.1.3}$$

where, K_L is the Langmuir equilibrium constant and is equal to k_a/k_d. This expression shows that adsorption under the Langmuir assumptions exhibits asymptotic behavior; as $C \rightarrow \infty$, $q_e \rightarrow q_m$. Linearizing Eq. (5.1.3),

$$\frac{C}{q_e} = \frac{C}{q_m} + \frac{1}{K_L q_m} \tag{5.1.4}$$

By plotting C/q_e vs. C at constant temperature from experimental data, C being the inlet concentration of contaminant, q_m and K_L can be found from the reciprocals of the slope and intercept, respectively.

Though the Langmuir isotherm is based on theoretical principles, it makes many simplifying assumptions and is not adequate to represent all adsorption systems. Langmuir's isotherms failures have led to an empirical isotherm, called the Freundlich isotherm (Ruthven, 1984).

$$q_e = K_F\, C^{1/n} \tag{5.1.5}$$

The Freundlich isotherm assumes that q_e is proportional to the bulk concentration of sorbate raised to a power, $1/n$, where n is greater than one for favorable isotherms, and less than one for non-favorable isotherms. K_F is the Freundlich equilibrium constant. The linearized form of the Freundlich isotherm is:

$$ln(q_e) = ln(K_F) + \frac{1}{n} ln(C) \tag{5.1.6}$$

Plotting $ln(q_e)$ vs. $ln(C)$ gives K_F and n from the intercept and slope of the graph, respectively.

5.1.2 Kinetics of Sorption in Column Adsorbers

5.1.2.1 Application of Models Reported in Literature

Practical adsorption systems consist of fixed bed adsorbers packed with the sorbent, and these adsorbers are operated until a breakthrough of the sorbate occurs from the column. Several models have been reported in literature to describe the kinetics of the sorption process occurring in these adsorbers. The model proposed in 1944 by Thomas (1944) is one of the most widely used models to predict fixed-bed column breakthrough. The Thomas Model, show below assumes that the Langmuir isotherm applies and that axial dispersion of the sorbate in the column is negligible (Biswas and Mishra, 2015; Mustafa and Ebrahim, 2010; Xu et al, 2013):

$$ln\left(\frac{C_0}{C_e} - 1\right) = \frac{q_0 k_{TH} M}{Q} - k_{TH} C_0 t \tag{5.1.7}$$

where C_0 and C_e are the inlet and outlet concentrations of the column, respectively; q_0 is the maximum adsorption capacity of the sorbent in equilibrium with C_0; k_{TH} is the Thomas kinetic constant; M is the mass of sorbent charged to the column; Q is the volumetric flow rate of fluid through the column, and t is the time of experiment. A plot of ln (C_0/C_e -1) vs. t gives a linear trend from which q_0 and k_{TH} can be found.

The Yoon-Nelson Model is a less complicated model that does require any adsorbent characteristics, such as sorbent capacity (Ghribi and Chlendi, 2011). The model assumes that the probabilities of breakthrough and the rate of decrease in adsorption are proportional. The Yoon-Nelson Model is described by Eq. (5.1.8).

$$ln\left(\frac{C_e}{C_0 - C_e}\right) = k_{YN}t - \tau k_{YN} \tag{5.1.8}$$

In Eq. (5.1.8), k_{YN} is the Yoon-Nelson kinetic constant, and τ is the time required for 50% breakthrough of the adsorbate. k_{YN} and τ can be found from the slope and intercept of the plot of left hand side Eq. (5.1.8) vs. t, respectively.

The model proposed originally proposed by Adams and Bohart (Bohart and Adams, 1920) was meant to account for the adsorption of chlorine on a fixed bed of activated carbon. It is based on the definition chemical activity in a diluted medium, and it is simplified to Eq. (5.1.9) by assuming (Chowdhury et al, 2013; Karpowicz et al, 1995):

- Low bulk concentrations of contaminant. $C << C_0$.
- When $t \rightarrow \infty$, $q \rightarrow N_0$. Where N_0 is the adsorption capacity of the adsorbent per unit volume of the bed.
- The rate of adsorption is limited by external mass transfer.

$$ln\left(\frac{C_e}{C_0}\right) = C_0 k_{AB}t - N_0 k_{AB}(H_T/v) \tag{5.1.9}$$

Like the Thomas and Yoon-Nelson Models, the Adams-Bohart Model includes a kinetic constant, k_{AB}. H_T is the height of the bed, and v is the superficial velocity of fluid through the column.

N_0 and k_{AB} can be found from a linear plot of ln (C_e/C_o) vs. t.

In general, these models can explain and fit to the experimental data reasonably well, however, their "kinetic constants" largely lack a physical meaning. We can examine the parameters' trend with temperature or concentration; however, no thermodynamic consideration is included in their calculation and the kinetic constants of these models lumped many phenomena into a single constant. Including thermodynamics in the BT curve prediction allows an iterative solution that is much more adaptable and discloses fundamental information about the adsorption process, such as the heat of adsorption, spontaneity of the process, and adsorption

behavior (isotherms)A more rigorous model can be derived from mass balance of the sorbate around a differential element of the adsorption column as described in the next section.

5.1.2.2 Mass-Transport Based Model

5.1.2.2.1 Model Derivation

A generalized mass balance over a differential element of a fixed bed adsorber is:

Rate of change of concentration in the gas phase = Flow of sorbate in - Flow of sorbate out - Rate of adsorption

This relation allows a differential equation to be derived provided the following assumptions,

1. The adsorption column has no radial concentration gradient.
2. Bulk gas follows the ideal gas law.
3. Properties of the sorbent including affinity for the contaminant and bed density are uniform.
4. The inflow of gas has a constant velocity, which it maintains in the column.

leading to Eq. (5.1.10).

$$\frac{\partial C(t,z)}{\partial t} = D_z \frac{\partial^2 C(t,z)}{\partial z^2} - v\frac{\partial C(t,z)}{\partial z} - \rho_b \frac{\partial q(t)}{\partial t} \qquad (5.1.10)$$

Where,

- t = Time of experiment
- z = Position in the column. z is contained in the range [0,L]
- $C(t,z)$ = Concentration of the gas contaminant or sorbate as a function of time and bed depth
- D_z = Diffusivity of the contaminant through the bulk gas
- v = Superficial velocity of the bulk gas through the column
- ρ_b = Density of the sorbent bed, (mass/volume)
- $q(t)$ = Adsorbed amount of the contaminant. Varies with time

Eq. (5.1.10) relates the spatial and temporal change in the bulk concentration of contaminant, $C(t,z)$ (left hand side of the equation), to the diffusive and convective mass convective mass transports in and out of the differential element (the first and second terms on the right hand side, respectively) and the rate of adsorption (the third term on the right hand side). Typically, the axial dispersion in gas flow columns at low flow is negligible, which reduces Eq. (5.1.10) to,

$$\frac{\partial C(t,z)}{\partial t} = -v\frac{\partial C(t,z)}{\partial z} - \rho_b \frac{\partial q}{\partial t} \qquad (5.1.11)$$

In Eq. (5.1.11), the adsorption rate term is the most significant, and is where the thermodynamics and kinetics of adsorption can be included.

Pseudo-First and Second Order Kinetic Models

There are several kinetic models proposed to describe the rate of adsorption on different adsorbents. The pseudo-first and pseudo-second order models for gas-solid adsorption are the most widely used because they are simple and fit many systems well (Song et al, 2016). Lagergren (1898) proposed the pseudo-first order model with the assumption that adsorption rate is proportional to the number of vacant adsorption sites, and is expressed as,

$$\frac{\partial q}{\partial t} = k_i(q_e - q) \tag{5.1.12}$$

Where, k_i is the pseudo-first order adsorption rate constant, and q_e is the equilibrium adsorption amount relative to the bulk concentration. At $t = 0$, $q = 0$, and as $t \rightarrow \infty$, $q \rightarrow q_e$. Solving Eq. (5.1.12) using these boundary conditions yields,

$$q = q_e\left(1 - e^{-k_i t}\right) \tag{5.1.13}$$

Pseudo-second order kinetics are similar, but assume that the rate of adsorption is proportional to the square of the number of vacant sites, as shown by Eq. (5.1.14).

$$\frac{\partial q}{\partial t} = k_s(q_e - q)^2 \tag{5.1.14}$$

Eq. (5.1.14) is the pseudo-second order kinetic model where k_s is the pseudo-second order kinetic rate constant. Using the same boundary conditions as above, the adsorbed amount at any time following pseudo-second order adsorption is given by,

$$q = \frac{q_e^2 k_s t}{1 + q_e k_s t} \tag{5.1.15}$$

Knowing how k_i varies with temperature allows us to solve the mass-transfer model to generate calculated BT curves at many temperatures, and makes the model more flexible. Kinetic rate constants are known to vary with temperature according to the Arrhenius equation,

$$k_i = k_0 * e^{\frac{-E_a}{RT}} \tag{5.1.16}$$

Where k_0 is the pre-exponential, or frequency, factor; E_a is the activation energy of adsorption; R is the universal gas constant, and T is the operating temperature. Linearizing Eq.(5.1.16) yields,

$$ln(k_i) = ln(k_0) - \left(\frac{E_a}{R}\right)\frac{1}{T} \tag{5.1.17}$$

From this equation, a plot of $ln(k_i)$ vs. $1/T$ can be used to find k_0 and E_a.

5.1.2.2.2 Development of a Numerical Solution

Eq. 11 was solved numerically by converting the differential equation into difference equations. The backward divided difference (BDD) approximations of various terms are shown in Eqs. (5.1.18) and (5.1.19).

$$\frac{\partial C(t,z)}{\partial t} \cong \frac{C_i^l - C_i^{l-1}}{\Delta t} \tag{5.1.18}$$

$$\frac{\partial C(t,z)}{\partial z} \cong \frac{C_i^{l-1} - C_{i-1}^{l-1}}{\Delta z} \tag{5.1.19}$$

Δz and Δt above are the segment and differential time element lengths, respectively; i and l denote the bulk off-gas concentration length segment and time element, respectively. Figure 5.1.1 depicts the adsorption column split into N_z segments of Δz length, and is shown at various saturation levels. The substituted approximations from Eqs. (5.1.18) and (5.1.19) are shown in Eq. (5.1.20) and the BDD method illustrated in Figure 5.1.2.

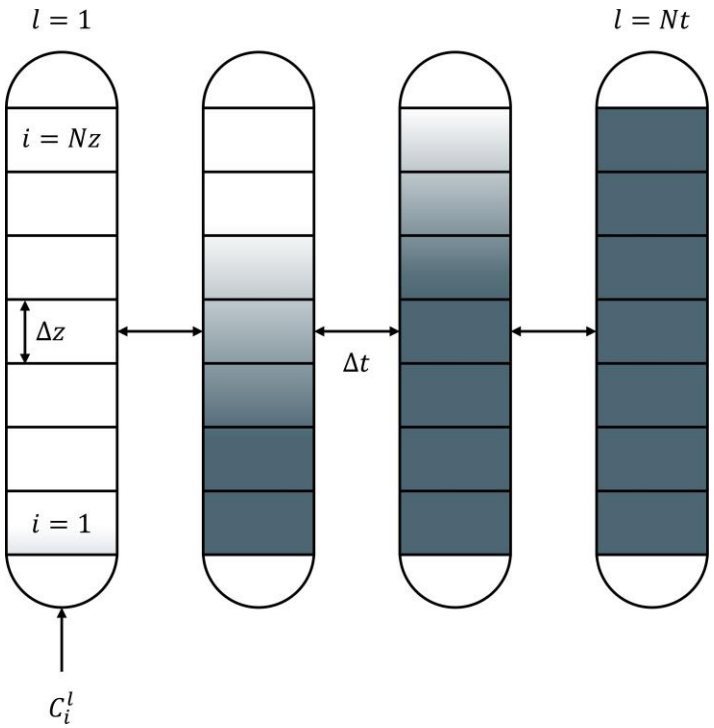

Figure 5.1.1: Fixed-bed adsorption column with discrete time and length steps

(*Column length: N_z segments of height Δz. Time steps duration of Δt. Current segment denoted by subscripts i, and l.*)

$$\frac{C_i^l - C_i^{l-1}}{\Delta t} = -v\frac{C_i^{l-1}C_{i-1}^{l-1}}{\Delta z} - \rho_b \left.\frac{\partial q}{\partial t}\right|_i^l \tag{5.1.20}$$

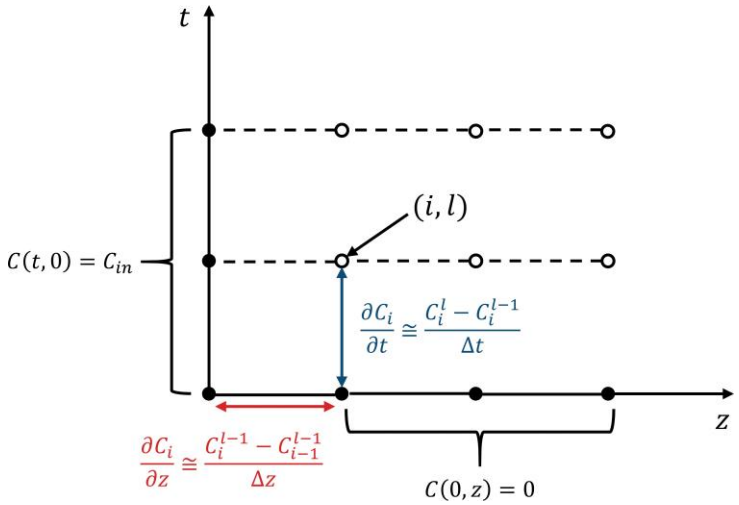

Figure 5.1.2: Illustration of method to solve Eq. (5.1.11)

Each circle represents a concentration at a segment in the column denoted by *i*, at a time step denoted by *l*. The filled circles represent values that are known before any solution is implemented, and the empty circles are concentration values that are unknown.

The first unknown node, (*i*, *l*) in Figure 5.1.2 is solved using known quantities, represented by the red and blue arrows, using Eq. (5.1.11). Once the concentration at (*i*, *l*) is known, node (*i* + 1, *l*) can be solved for. This is repeated to solve concentrations for all *i* at time step *l*. The time step is incremented to *l* + 1, and bulk concentration can again be solved for all length segments. These steps are repeated until the bulk concentration is known for all *i* and *l*.

When carrying out this numerical solution, the rate of adsorption term from Eq. (5.1.11) is evaluated at the concentration node currently being solved; this is shown by Eq. (5.1.21).

$$\left.\frac{\partial q}{\partial t}\right|_i^l = k_i(q_e - q_i^l) \tag{5.1.21}$$

In Eq. 12, q_i^l is the amount of contaminant adsorbed in segment *i* at time step *l*, and is estimated by Euler's method, as shown in Eq. (5.1.22).

$$q_i^l = q_i^{l-1} + k_i(q_e - q_i^l)\Delta t \tag{5.1.22}$$

Solving Eq. (5.1.22) for q_i^l yields Eq. (5.1.23),

$$q_i^l = \frac{q_i^{l-1} + q_e k_i \Delta t}{1 + k_i \Delta t} \tag{5.1.23}$$

Eq. (5.1.23) is then substituted into Eq. (5.1.21) to obtain,

$$\left.\frac{\partial q}{\partial t}\right|_i^l = k_i\left(q_e - \frac{q_i^{l-1} + q_e k_i \Delta t}{1 + k_i \Delta t}\right) \tag{5.1.24}$$

Simplifying yields,

$$\left.\frac{\partial q}{\partial t}\right|_i^l = \frac{k_i}{1 + k_i \Delta t}\left(q_e - q_i^{l-1}\right) \tag{5.1.25}$$

And, further substituting for q_e using Eq. (5.1.3) yields,

$$\left.\frac{\partial q}{\partial t}\right|_i^l = \frac{k_i}{1 + k_i \Delta t}\left(\frac{q_m K_L C_i^l}{1 + K_L C_i^l} - q_i^{l-1}\right) \tag{5.1.26}$$

Now that we have obtained $\frac{\partial q}{\partial t}$ in terms of C_i^l and q_i^{l-1}—a known quantity— Eq. (5.1.26) can be substituted into Eq. (5.1.20) to obtain Eq. (5.1.27).

$$\frac{C_i^l - C_i^{l-1}}{\Delta t} = -v\frac{C_i^{l-1} C_{i-1}^{l-1}}{\Delta z} - \rho_b \frac{k_i}{1 + k_i \Delta t}\left(\frac{q_m K_L C_i^l}{1 + K_L C_i^l} - q_i^{l-1}\right) \tag{5.1.27}$$

To simplify Eq. (5.1.27) the following substitutions are made.

$$\lambda = v\frac{\Delta t}{\Delta z} \tag{5.1.28}$$

$$B = \frac{\rho_b k_i \Delta t}{1 + k_i \Delta t} \tag{5.1.29}$$

$$C_i^l = \alpha \tag{5.1.30}$$

$$C_i^{l-1} = \beta \tag{5.1.31}$$

$$C_{i-1}^{l-1} = \gamma \tag{5.1.32}$$

$$q_i^{l-1} = \delta \tag{5.1.33}$$

Substituting Eq. (5.1.28) – Eq. (5.1.33) into Eq. (5.1.27) results in:

$$\alpha - \beta = -\lambda(\beta - \gamma) - \rho_b \Delta t\left[\frac{k_i}{1 + k_i \Delta t}\left(\frac{K_L q_m \alpha}{1 + K_L \alpha} - \delta\right)\right] \tag{5.1.34}$$

Which can be rearranged into the quadratic form to solve for C_i^l:

$$\alpha = C_i^l = \frac{-b \pm \sqrt{b^2 - 4ac}}{2a} \tag{5.1.35}$$

Where,

$$a = K_L \tag{5.1.36}$$

$$b = K_L\left(\beta(\lambda - 1) - \lambda\gamma + B(q_m - \delta) + \frac{1}{K_L}\right) \tag{5.1.37}$$

and

$$c = -(\beta(1 - \lambda) + \lambda\gamma + B\delta) \quad (5.1.38)$$

A MATLAB program was developed to solve the equations numerically.

5.2 Experimental Validation

5.2.1 Experimental Setup and Procedure

Dynamic sorption experiments were conducted to obtain experimental data on the sorption of iodine and krypton on the sorbent used in the study – nanostructured carbon supported on Engelhard Titanosilicate 10 (C@ETS10). Simulated off-gas was flowed through an adsorption column charged with 1–4 g of sorbent. Details of the experimental setup, procedure for sorption studies and experimental data have been presented above and are not repeated here.

5.2.2 Results and Discussion

5.2.2.1 Adsorption Isotherm

Table 5.2.1 shows the isotherm constants obtained for I_2 and Kr at 20°C.

Table 5.2.1: Isotherm parameters for adsorption of multicomponent on C@ETS-10 sorbent at 20°C column temperature

Models	Constants	Species	
		Iodine	Krypton
Langmuir	Q_m (mg g^{-1})	57.33	0.2933
	K_L (L mg^{-1})	10.7	0.52
	R^2	0.9973	0.9526
Freundlich	K_F (mg g^{-1} ppm^{-1})	20.72	0.0009
	n (mg^2 g^{-1} L^{-1})	4.572	1.19
	R^2	0.9925	0.9992

The experimental data for multicomponent were properly fitted by Langmuir isotherm with large correlation coefficient (< 0.997). The iodine experimental data was also fitted to Freundlich isotherm with R^2 value - 0.9921 (Figure 5.2.1). However, a correlation coefficient value of

Freundlich for Kr adsorption was less than 0.90, which indicates large fluctuation in experimental data (Figure 5.2.2). It was clear that both Langmuir and Freundlich model approximately describe the adsorption isotherm of I_2, however, only Langmuir model fitted to Kr adsorption on C@ETS-10 sorbent. The maximum I_2 and Kr sorption capacities of sorbent were found to be 57.48 and 0.0765 mg g^{-1} from Langmuir isotherm at 20°C.

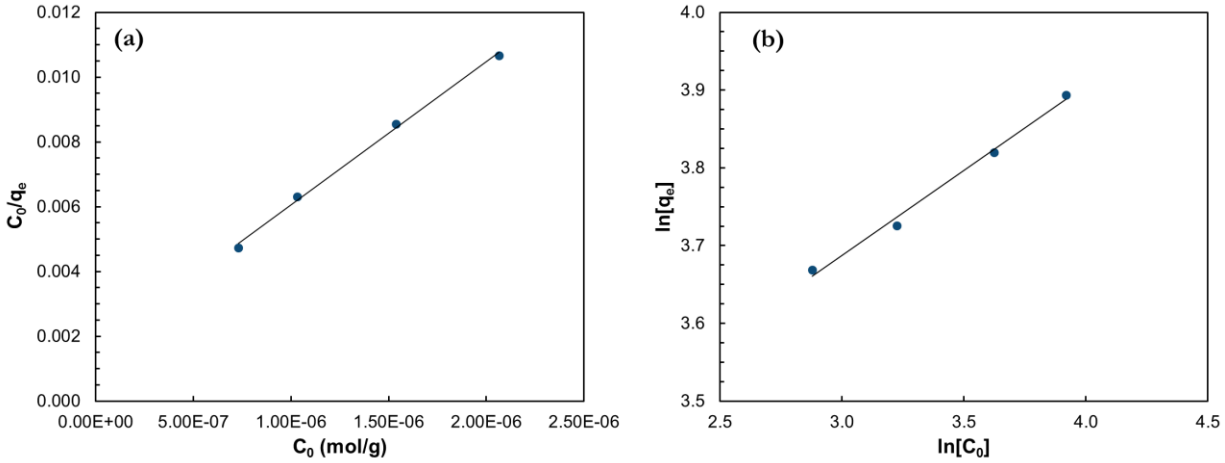

Figure 5.2.1: Adsorption isotherm of (a) Langmuir and (b) Freundlich models for adsorption of I2 on 10 wt% C@ETS-10 sorbent at 20°C

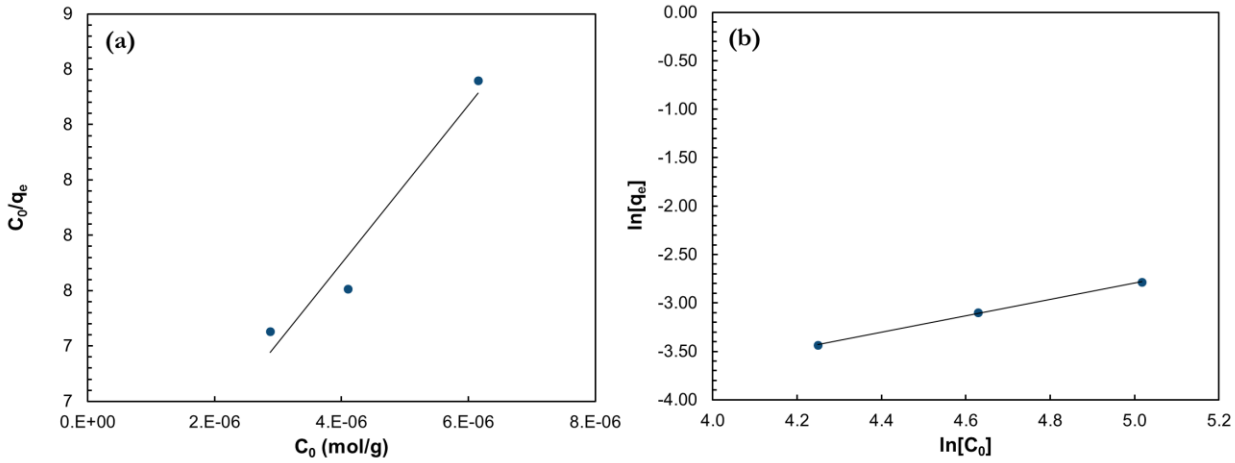

Figure 5.2.2: Adsorption isotherm of (a) Langmuir and (b) Freundlich models for adsorption of Kr on 10 wt% C@ETS-10 sorbent at 20°C

5.2.2.2 Application of Literature Kinetic Models

The Thomas, Yoon-Nelson, and Adams-Bohart model parameters from equations 7-9 were found for single component iodine experiments, shown in Table 5.2.2, and multicomponent experiments, shown in Table 5.2.3 and Table 5.2.4. Figure 5.2.3 and Figure 5.2.4 compare the experimental and model generated breakthrough curves. All model breakthrough curves were generated by solving equations 7-9 for C_e/C_0 using model parameters from the tables.

Table 5.2.2: Thomas, Yoon-Nelson, and Adams-Bohart Model parameters for iodine breakthrough in single component temperature variation experiments

Model	Component	Iodine			
	Temp. (°C)	10	20	40	60
Thomas	q_0 (mg/g)	24.69	19.37	12.62	9.56
	k_{TH} (L/gh)	2123	2536	4123	5049
	R^2	0.9640	0.9312	0.9409	0.9130
	SSE	0.0404	0.0302	0.0373	0.0674
Yoon-Nelson	τ (hr)	8.817	6.917	4.507	3.415
	k_{YN} (1/hr)	0.5506	0.6577	1.0690	1.3092
	R^2	0.9640	0.9312	0.9409	0.9130
	SSE	0.0404	0.0302	0.0373	0.0674
Adams-Bohart	N_0 (g/L)	9.111	8.139	5.251	4.189
	k_{AB} (L/gh)	1120	1101	1804	2131
	R^2	0.9574	0.9287	0.9242	0.9353
	SSE	0.6282	0.9370	1.0896	0.5517

The R^2 values shown in the tables are measures of how well the experimental data fits the linearized forms of the model equations. The sum of the squared errors, SSE, indicates how well the experimental breakthrough curves match the breakthrough curves generated by each model.

Examining model equations more closely, we see that the Thomas and Yoon-Nelson models are mathematically equivalent; this is made apparent by the identical R^2 and SSE values for both models. The difference between the two models is in their utility. The Yoon-Nelson Model is more concise in form, as it excludes parameters that describe the sorbent bed in its calculation; thus, when extrapolating the model over wide ranges of operating conditions the Yoon-Nelson

model has less utility than the Thomas model which includes flow rate and bed height in its calculation. In general, the Thomas and Yoon-Nelson models fit significantly better than the Adams-Bohart model. The superior fit is exemplified by the SSE values for the Thomas and Yoon-Nelson models being lower than the Adams-Bohart model in Table 5.2.2-4. Further, the Adams-Bohart breakthrough curve fits in Figure 5.2.3 and Figure 5.2.4 increase exponentially without being limited to $C_e/C_0 = 1$, and this trend is not realistic.

The parameters of the three models describe the bulk properties of the sorbent. These parameters define the general height and length of the BT curve. Figure 5.2.3 and Figure 5.2.4 show that each kinetic model generally fits the overall height and length of the experimental breakthrough curves well. As such, the sorption capacity parameters are close to the sorption capacities calculated for each experiment. In single component experiments, the sorbent capacity calculated from the experiment ranged from 11.8 mg/g at 60^{o}C to 28.0 mg/g at 10^{o}C; the q_0 parameter from the Thomas model for the single component iodine experiments is about 15% smaller, ranging from 9.56 to 24.7 mg/g in the same temperature range. The reason for the discrepancy between q0 and the actual sorption capacity is because the Thomas model predicts a slightly faster breakthrough, as shown in Figure 5.2.3, and this correlates to a smaller sorption capacity. Another discrepancy of the Thomas and Yoon-Nelson models is seen at the top and bottom of the 'S' curve shape. This is especially true of the multicomponent iodine breakthrough fits shown in Figure 5.2.4a and c. One possible explanation that the Thomas and Yoon-Nelson models do not conform to the exact shape of the experimental data breakthrough is that the inlet concentration of iodine during experiments tended to drift by ~3 ppm. Both models are based on a constant inlet concentration assumption and were found to be quite sensitive to changes; model parameters varied up to 25% when calculated with a 3 ppm change in the inlet concentration.

Table 5.2.3: Thomas, Yoon-Nelson, and Adams-Bohart Model parameters for iodine and krypton breakthrough in multicomponent concentration variation experiments

Model	Component	Iodine				Krypton		
	Concentration (ppm)	15	25	35	50	70	100	150
Thomas	q_0 (mg/g)	37.85	38.72	45.20	50.38	0.0286	0.0331	0.0621
	k_{TH} (L/gh)	656.7	325.5	254.7	311.2	300093	145439	110946
	R^2	0.9571	0.9306	0.9931	0.9868	0.9415	0.9958	0.9674
	SSE	0.0734	0.0385	0.0034	0.0134	0.0238	0.0025	0.0115
Yoon-Nelson	τ (hr)	47.79	34.30	28.75	22.50	0.0273	0.0226	0.0274
	k_{YN} (1/hr)	0.1207	0.0850	0.0930	0.1618	72.96	49.31	58.51
	R^2	0.9571	0.9306	0.9931	0.9868	0.9415	0.9958	0.9674
	SSE	0.0734	0.0385	0.0034	0.0134	0.0238	0.0025	0.0115
Adams-Bohart	N_0 (g/L)	12.64	15.84	18.77	19.22	0.0208	0.0404	0.0643
	k_{AB} (L/gh)	426.5	166.0	132.1	168.9	51905	19817	12475
	R^2	0.8757	0.9389	0.9402	0.8522	0.9653	0.7147	0.7956
	SSE	5.3118	0.0650	0.2447	1.6472	0.0061	0.0581	0.0376

Table 5.2.4: Thomas, Yoon-Nelson, and Adams-Bohart Model parameters for iodine and krypton breakthrough in multicomponent temperature variation experiments

Model	Component	Iodine			Krypton		
	Temp. (°C)	20	40	60	20	40	60
Thomas	q_0 (mg/g)	38.72	31.08	29.38	0.0869	0.0588	0.0347
	k_{TH} (L/gh)	325.5	411.3	682.6	122666	212487	406708
	R^2	0.9306	0.8852	0.9312	0.9844	0.9819	0.9939
	SSE	0.0385	0.1089	0.0784	0.0124	0.0114	0.0050
Yoon-Nelson	τ (hr)	34.31	26.86	25.98	0.0842	0.0560	0.0330
	k_{YN} (1/hr)	0.0850	0.1101	0.1788	29.41	51.66	98.89
	R^2	0.9306	0.8852	0.9312	0.9844	0.9819	0.9939
	SSE	0.0385	0.1089	0.0784	0.0124	0.0114	0.0050
Adams-Bohart	N_0 (g/L)	15.84	14.85	9.77	0.0545	0.0364	0.0187
	k_{AB} (L/gh)	166.0	154.7	470.9	33443	57733	103952
	R^2	0.9389	0.8012	0.8036	0.7047	0.6620	0.7725
	SSE	0.0650	0.7931	7.3840	0.2280	0.4864	0.2298

Another reason that the Thomas and Yoon-Nelson models may not conform to the shapes of the multicomponent curves specifically is the existence of a competition between iodine and krypton for adsorption sites. This competition can change the shape of the BT curves in ways unaccounted for by the Thomas and Yoon-Nelson models. However, the general fit still represents the experimental capacity and the length of the MTZ in general, as the inlet

concentration was taken frequently during experiments and an average value for the inlet concentration was used for all calculations.

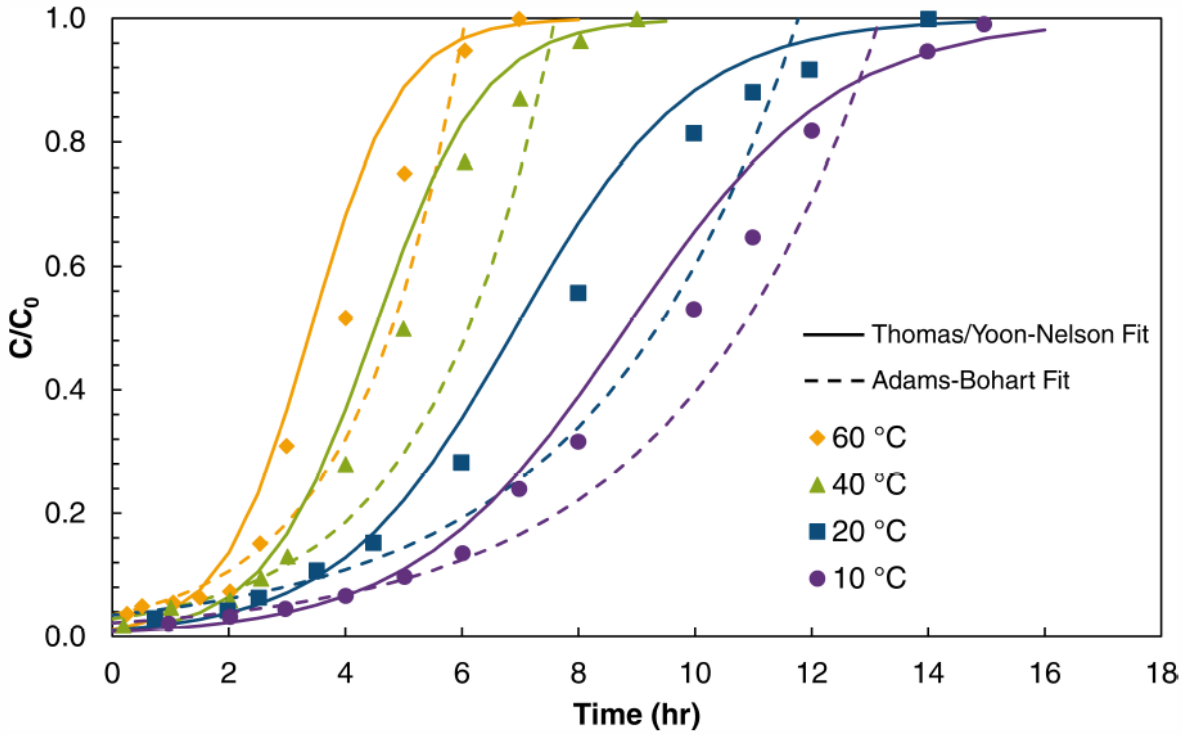

Figure 5.2.3: Thomas, Yoon-Nelson, and Adams-Bohart model fits for single component iodine breakthrough experiments

Overall, the purpose of modeling is to predict breakthrough behavior at inlet concentrations and temperatures not experimentally tested. To do this accurately, the model parameters must follow a predictable trend. The trends of the model parameters are illustrated in Figure 5.2.5, which shows the model parameters for iodine breakthrough experiments as functions of temperature for single component experiments, and inlet concentration for multicomponent experiments. Parameter fits for single component iodine experiments in Figure 5.2.5a–c show a definite trend in the model parameters. The kinetic constants for each model increase with temperature close to linearly, though the deviations appear unpredictable. Multicomponent iodine parameter fits are much more erratic. Trends exist, but it is less clear whether it is due to the system's conditions for outlying data.

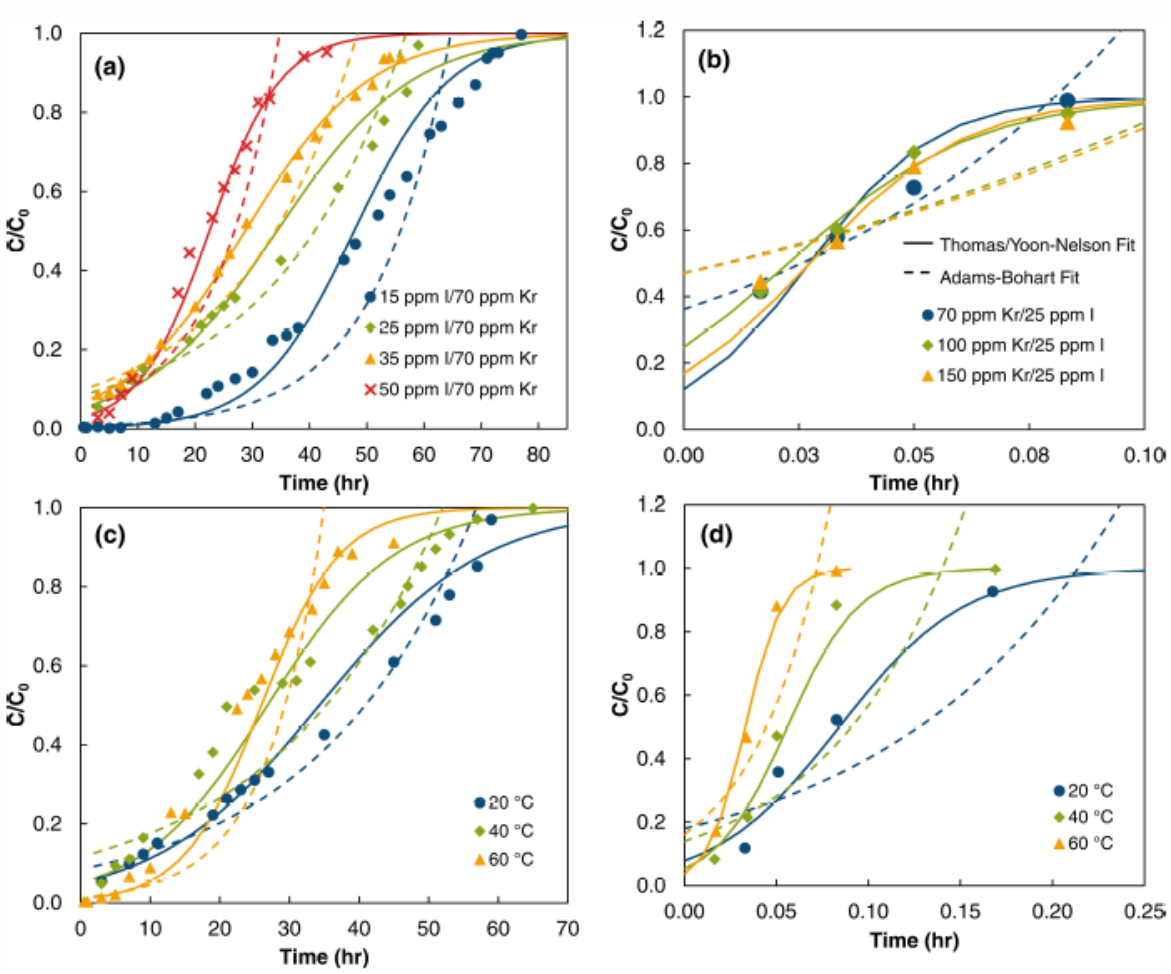

Figure 5.2.4: Thomas, Yoon-Nelson, and Adams-Bohart model fits for multicomponent experiments

(a) iodine breakthrough with inlet iodine concentration variation, (b) krypton breakthrough with krypton inlet concentration variation, (c) iodine breakthrough with column temperature variation, and (d) krypton breakthrough with column temperature variation. Thomas/Yoon-Nelson fits are shown by a solid line, and Adams-Bohart by a dashed line. Model line colors correspond the breakthrough colors shown in the legend on each graph.

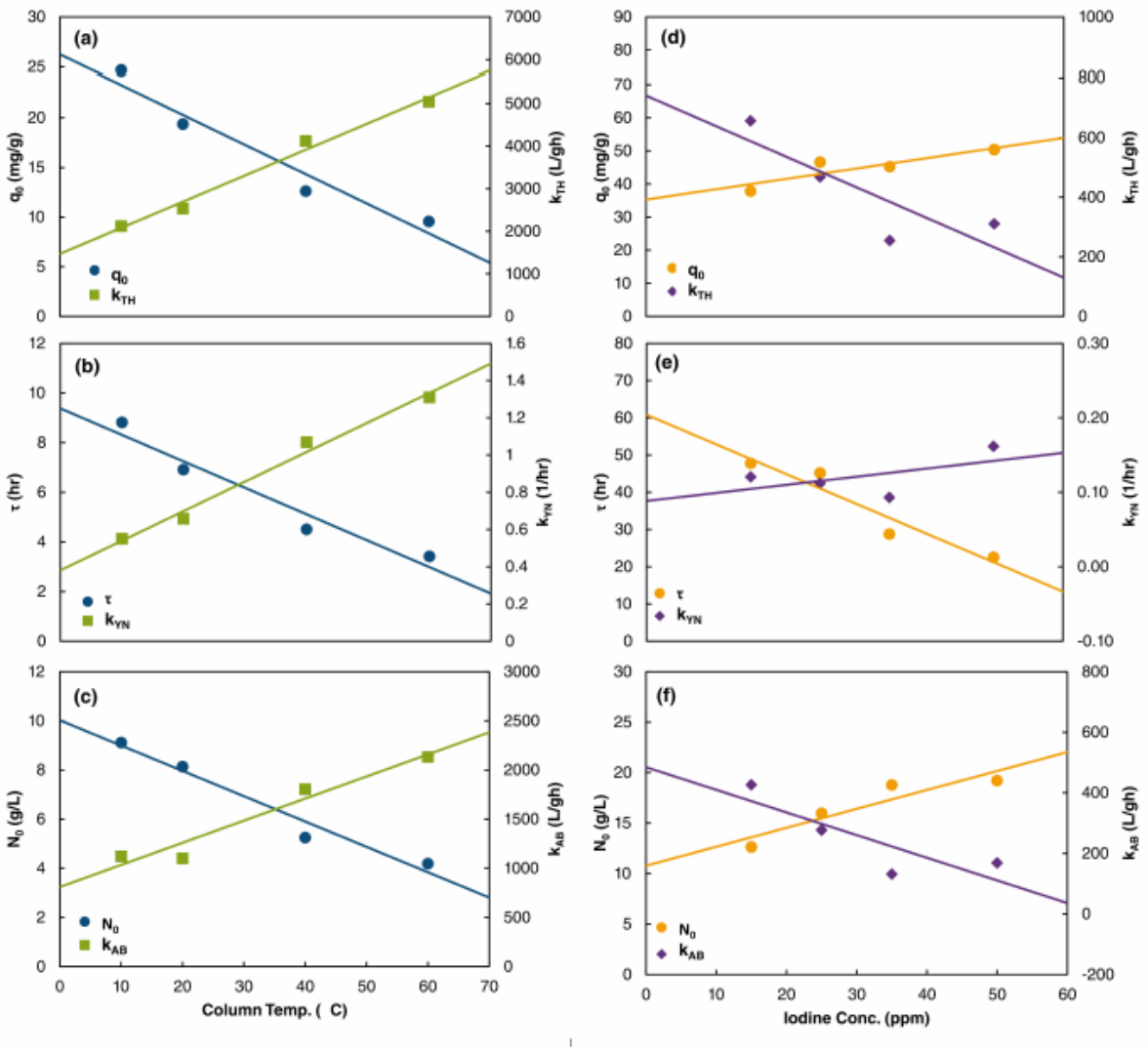

Figure 5.2.5: Thomas, Yoon-Nelson, and Adams-Bohart parameters as functions of (a-c) temperature for single component iodine experiments, and (d-f) inlet iodine concentrations for multicomponent experiments

5.2.2.3 Mass Transfer Model Results

Figure 5.2.6 shows a comparison of the numerically solved mass-transfer model and experimental breakthrough curves for single component and multicomponent iodine experiments. As with the Thomas and Yoon-Nelson models, the mass-transfer model fits single component data better than the multicomponent data. Each example in Figure 5.2.6 is representative of the mass-transfer model fit for all iodine experiments; the mass-transfer model fits single component experiments well, but does not fit the top and bottom of the 'S' curve for multicomponent experiments as closely. Some of the misfit is corrected by inputting inlet

concentration as a function of time into the mass-transfer model—accounting for inlet concentration drift—but some discrepancies remain. A parametric study to investigate these discrepancies was performed and the results are discussed below.

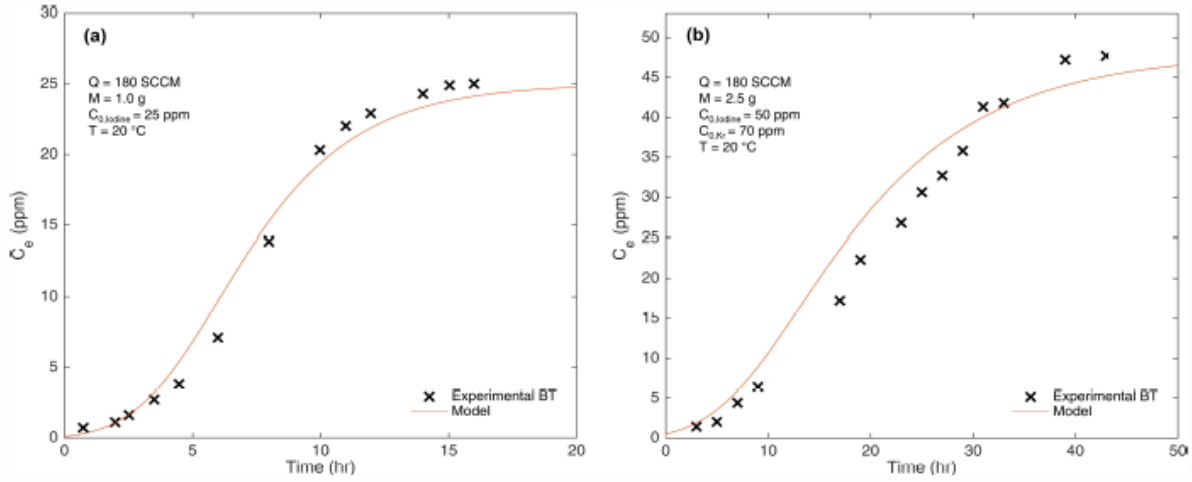

Figure 5.2.6: Mass-transfer model fit of experimental iodine breakthrough curves

5.2.2.3.1 Parametric Sensitivity Study of Mass Transfer Model

The sensitivity of results to the parmeters k_0, E_a, q_m, and K_L was studied by varying their values and the results are shown in Figure 5.2.7. As expected, higher values of the rate constant increase the slope of the breakthrough curve. Increasing the rate constant through both parameters increases the overall rate of adsorption and the sorbent reaches equilibrium faster. The mass-transfer model shows a similar response to changes in pre-exponential factor and activation energy, though is much more sensitive to activation energy changes due to the exponential term.

Changes in the isotherm parameters q_m and K_L did not change the breakthrough curve significantly, but rather, shifted it. Increasing q_m by 50% maintained the curve shape, but the exhaustion time increased, lowering it by lowered the exhaustion time by the same amount. Varying the Langmuir equilibrium constant, K_L, shifted the curve similarly—higher values increased exhaustion time. However, the main effect of changing K_L was on the shape of the bottom of the 'S' curve. This occurs because K_L is related to the rate of sorption, not the capacity. Higher values of the Langmuir equilibrium constant translate to a higher rate of sorption—primarily during the beginning of the experiment when the driving force for adsorption is

greatest. The higher sorption rate keeps the effluent concentration lower for longer, but the outlet concentration increases at a higher rate overall.

The effect of these parameters divulges why experimental data deviates from the model. There are two likely explanations for the deviation of the model from experimental results seen in Figure 5.2.6. Firstly, the pseudo-first order kinetic model may not approximate this adsorption accurately; Secondly, inaccurate representation of the equilibrium constant. In our model we use the Langmuir equilibrium constant which relates the equilibrium concentration of the bulk to the adsorbed phase. However, the Langmuir equilibrium constant is idealized from the original definition of the equilibrium constant as shown below by Eq. (5.2.1).

$$K = \prod_i (a_i)^{\nu_i} \tag{5.2.1}$$

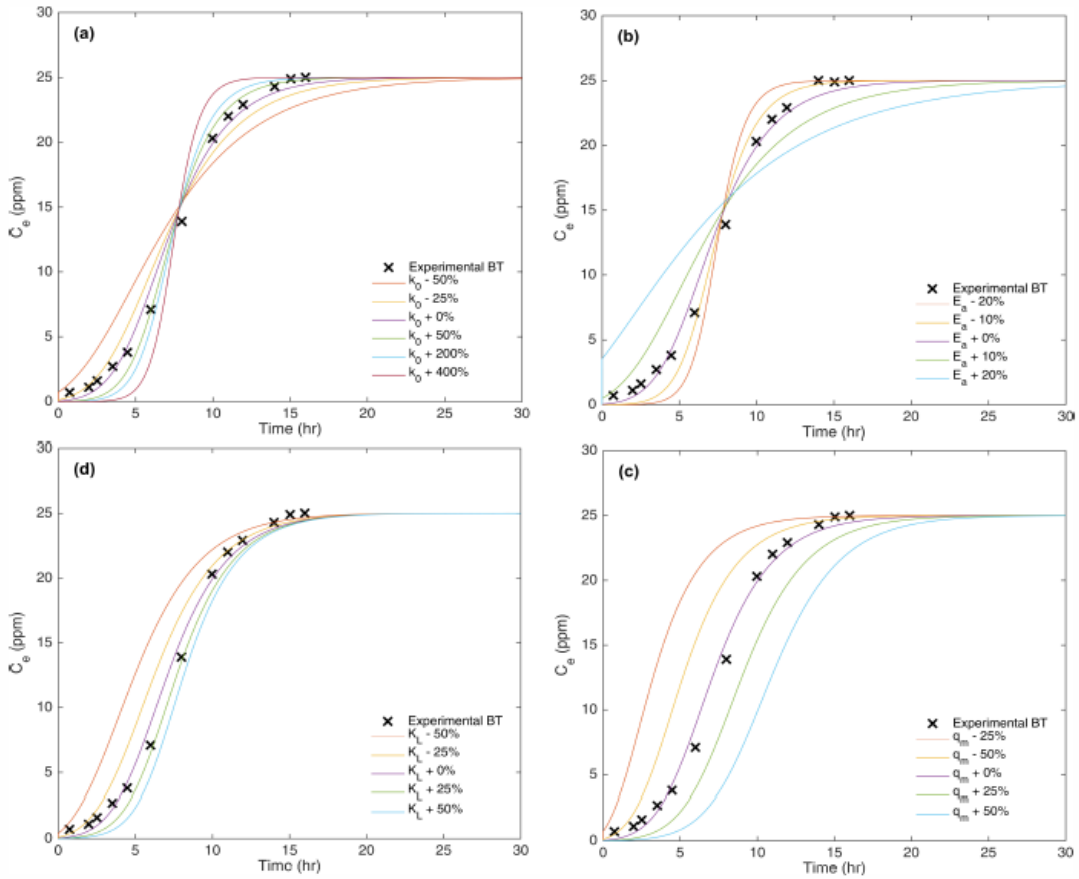

Figure 5.2.7: Parametric study showing the effect of parameter variation on the shape of the mass-transfer based breakthrough curve

(a) pre-exponential factor, (b) activation energy, (c) maximum adsorption capacity, and (d) the Langmuir equilibrium constant

Eq. (5.2.1) defines the equilibrium constant on an activity basis, where K is the equilibrium constant, a_i is the activity of component i, and ν_i is the stoichiometric coefficient of component i.

Many researchers have commented on the fallacy in using the Langmuir equilibrium constant to predict isotherms (Diagboya et al, 2014; Dikmen et al, 2015; Liu, 2009; Salvestrini et al, 2014; Tran et al, 2016; Trinh et al, 2015). However, modification of the Langmuir equation—such as to the extended Langmuir equation shown in Eq. (5.2.2) which includes multiple components as part of its derivation—can alter the mass-transfer model to fit experimental BT suitably for industrial modeling application.

$$q_{e,i} = \frac{q_{m,i} K_{L,i} C_i}{1 + \sum_{i=1}^{n} K_{L,i} C_i} \qquad (5.2.2)$$

where, the subscript i denotes a specific contaminant, and n is the number of contaminants.

Temperature dependence is included in through the dependence of equilibrium constant on the heat of adsorption.

The unknowns in above equations can be determined by performing experiments over a wide range of temperatures and bulk gas concentrations, allowing the use of the mass-transfer model on a more rigorous thermodynamic and kinetic basis.

5.3 Integrated System Design

Continuous processes offer the advantages of increased productivity, reduced costs, and adaptability over batch processes. Adsorption is no different, and the control and capture of the contaminants will be based on a fixed bed column adsorber through which a continuous off-gas stream is flowing. The sorbent packed in the column will adsorb the contaminants and exhaust its capacity. This situation is more complex than batch operation because the flow dynamics and transfer rate of the sorbate between fluid and sorbent have a significant impact on the removal in addition to the equilibrium driven batch processes. The principles of design of such systems is presented below:

5.3.1 Mass Transfer Zone

In fixed-bed adsorption system, contaminant concentrations in the bulk and adsorbed phases change with position in the sorbent bed and time creating concentration profiles. Figure 5.3.1illustrates the concentration profile of the fluid phase in a fixed-bed column. The bottom half of the figure shows the effluent concentration of the column. The effluent concentration is related to the saturation level of the sorbent, which is pictured in the upper half of Figure 5.3.1.

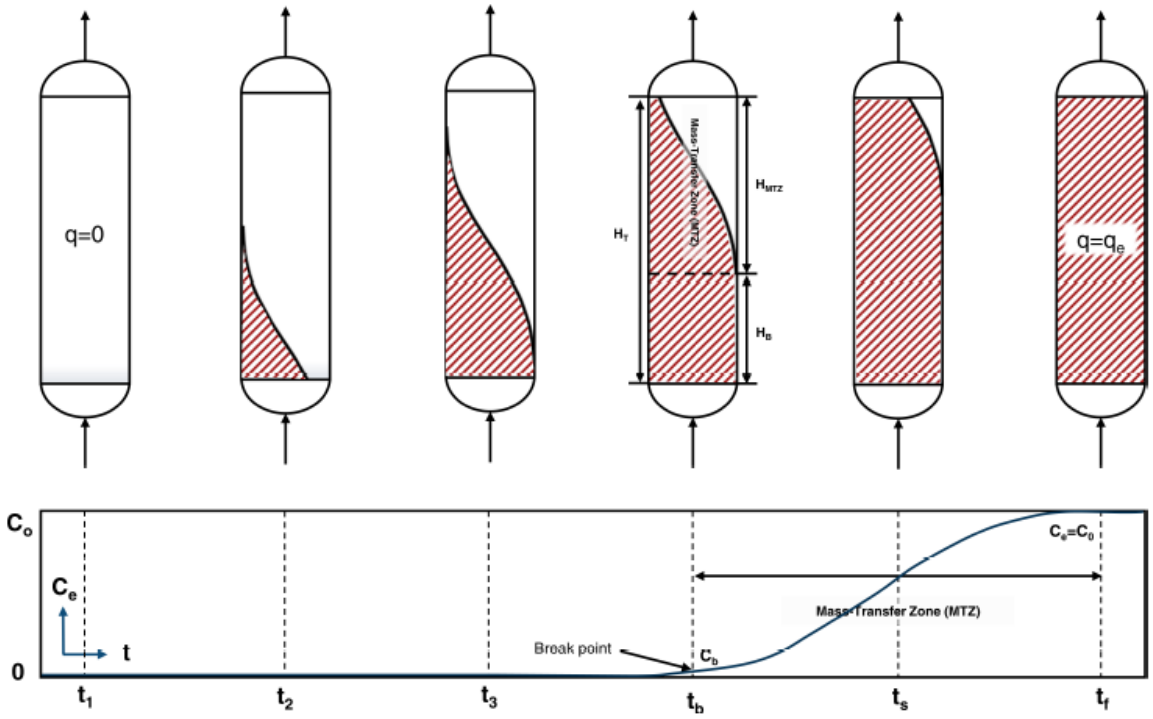

Figure 5.3.1: Bulk fluid concentration profile in a fixed-bed adsorption column as a function of height in the sorbent bed and time

When adsorption begins at time t_1, the sorbent contains no contaminant. The rate of adsorption is highest when the fluid containing the contaminant contacts the bed. As the contaminant is adsorbed along the bed, its concentration in the bulk fluid drops until none is left in the bulk.This length of bed where adsorption occurs is known as the mass-transfer zone (MTZ), and it is depicted in Figure 5.3.1 at time t_b. The length of the MTZ depends on the rate of adsorption, and is elongated by mass-transfer resistances which slow adsorption rate. The mass-transfer resistances and axial dispersion in the bed also create the 'S' shape of the MTZ. Once the section of the sorbent bed closest to the inlet is saturated, the MTZ shifts toward the end of the bed until time t_b, the break point, when the outlet concentration of the column is C_b, the

maximum allowed concentration of contaminant in the outlet stream. After tb, the outlet concentration continues to increase until the exhaustion time, t_f , when the sorbent is completely saturated.

5.3.2 Scale-up Design of Fixed Bed Adsorbers

Knowledge of the MTZ properties is critical because in industrial applications adsorption may only be carried out until the break point, since no effluent concentration greater than C_b is allowed. Column design requires that the height of the bed must be much larger than the MTZ to maximize effective use of the sorbent and avoid having to recharge the adsorption column frequently. Because of the C_b limit, adsorption can not be carried out to equilibrium, or saturation of the sorbent, and the sorbent capacity calculated through Eq. (5.2.2) at equilibrium is not representative of the sorbent's usefulness; only a portion of this capacity may be utilized.

$$q_i = Q \int_0^{t_f} \frac{(C_{i0} - C_{ie})}{M} dt \tag{5.3.1}$$

While Eq. (5.3.1) represents the total sorbent capacity, Eq. (5.3.2) provides for the estimation of the useful or effective operational capacity.

$$q_{iu} = Q \int_0^{t_b} \frac{(C_{i0} - C_{ie})}{M} dt \tag{5.3.2}$$

q_{iu}, or the usable sorbent capacity, is the loading of contaminant on the sorbent at the time at which the effluent concentration of the column is at the maximum permissible level, C_b. The ratio q_{iu}/q_i is then the fraction of the total bed capacity completely saturated at t_b. If the sorbent bed is assumed to have uniform density and adsorptive properties, then the ratio q_{iu}/q_i is also proportional to the length of the bed saturated, H_B, at t_b. H_B is found by Eq. (5.3.3) and illustrated in Figure 5.3.1.

$$H_B = \frac{q_{iu}}{q_i} H_T \tag{5.3.3}$$

Where H_T is the total height of the sorbent bed. The length of the MTZ, H_{MTZ}, can then be found by the difference of the total height of the bed and the length of bed that is saturated. Once the height of the MTZ is known, it can be used in conjunction with removal requirements to design an adsorption column. The caveat of extending this method to other operating conditions is that the height of the MTZ changes with temperature, inlet concentration, and other parameters.

5.3.3 Application to the Current System and Recommendations for Future Work

Considerable experimentation was conducted in this project to obtain data as function of inlet concentration of contaminants, operating temperature, presence of individual or both components, relative humidity, as well as sorbent characteristics. The resulting data proved to be useful for obtaining the thermodynamics and kinetics of the process as described above. These experimental data allowed the project team to determine the utility and limitations of the models reported in the literature, as well as simulate and verify the mass transport based model. However, the constraints of the experimentations including time limitations did not permit obtaining sufficient data for the application of the integrated system model.

The research conducted for the project has proved the effectiveness of the nanostructured ETS-10 supported nanostructured carbon for the removal of iodine and krypton present in the off-gas streams. It is recommended that future experimentation be conducted with scaled-up systems on a progressively larger scale to observe the effect of system size. The first scale up parameters proposed are the doubling of the column diameter and a five-fold increase in the column height. These sets of experiments will yield information that can be used to confirm/refine the equilibrium and mass transport model parameters, as well as provide sufficient data for verification of the integrated system model.

5.4 Summary of Results

The results of the modeling activities can be summarized as follows:

1. The equilibrium relationships for the contaminants can be expressed by the Langmuir adsorption isotherm. Dynamic continuous column sorption experiments yielded data from which model parameters could be obtained.
2. The literature-reported Thomas, Yoon-Nelson, and Adams-Bohart models were used to describe the kinetics of sorption in the columns. These models had some utility, however, lack of physical significance of the parameters limits their application to the system.
3. A more fundamental mass-transport based model was developed for the system, and numerical solution of the model obtained by developing a custom program using MATLAB. This approach holds a greater promise for developing the mathematical description of the process. Possible refinements of the fundamental equilibrium relationships were also presented.
4. An integrated system model was presented based on the mass transfer zone approach. Further experimental work is needed for obtaining the model parameters and verification/validation.

6 Conclusions

Reprocessing of UNF is expected to play an important role for sustainable development of nuclear energy by increasing the energy extracted from the fuel and reducing the generation of the high level waste (HLW). However, aqueous reprocessing of UNF is accompanied by emission of off-gas streams containing radioactive nuclides including iodine, krypton, xenon, carbon, and tritium. Volatile iodine (^{129}I), and krypton (^{85}Kr) are long lived-isotopes which have adverse effects on the environment as well as human health. Development of methods for the capture and long-term storage of radioactive gases is of crucial importance in order to manage their emissions that are anticipated to increase significantly with the growth of nuclear energy.

For more than 70 years, porous solid sorbents have been in the forefront of radioactive contaminant removal due to promising results and their advantages such as high removal efficiency, low maintenance cost, simple equipment design and operation over other techniques. The research conducted in this project has focused on development of a novel nanostructured sorbent and its application for the capture of the above two contaminants of interest.

Nanostructured carbon polyhedrons supported on Engelhard Titanosilicate-10 sorbent was synthesized using hydrothermal methods and subjected to structural and compositional characterization using various techniques including electron microscopy, Raman, x-ray diffraction and BET surface area analysis. Dynamic sorption experiments conducted using a flow-through column setup yielded information on the thermodynamics and kinetics of sorption in single-contaminant and multi-contaminant streams. Parameters varied in the study included carbon loading, temperature, contact time, contaminant concentration and humidity. The behavior of the system was modeled using models available in literature as well as development of a mass-transfer model from fundamental principles. Experimental investigations were also conducted for developing matrix for immobilization and isolation of contaminants.

The results of the research have been presented at several national and international meetings of various professional societies, and published in refereed technical publications. The project has also resulted in mentoring of several individuals including a post-doctoral research associate, and graduate and undergraduate students. The project has thus also served to address the need for qualified, technical workforce for the nuclear field.

References

Anderson M W, O Terasaki, T Ohsuna, A Phillippou, S P MacKay, A Ferreira, J Rocha, S Lidin. 1994. Structure of the microporous titanosilicate. ETS-10. *Nature*, 367: 347.

Bazan R E, M Bastos-Neto, A Moeller, F Dreisbach, R Staudt. 2011. Adsorption equilibria of O_2, Ar, Kr and Xe on activated carbon and zeolites: single component and mixture data. *Adsorption*, 17: 371–383.

Biswas S, U Mishra. 2015. Continuous fixed-bed column study and adsorption modeling: removal of lead ion from aqueous solution by charcoal originated from chemical carbonization of rubber wood sawdust. *Journal of chemistry*, 2015: 1-9, http://dx.doi.org/10.1155/2015/907379.

Bohart G, E Q Adams. 1920. Some aspects of the behavior of charcoal with respect to chlorine. *Journal of the American Chemical Society*, 42: 523–529.

Chowdhury Z Z, S M Zain, A K Rashid, R F Rafique, K Khalid. 2013. Breakthrough curve analysis for column dynamics sorption of Mn(II) ions from wastewater by using Mangostana garcinia peel-based granular-activated carbon. *Journal of chemistry*, 2013.Ii: 1-8, http://dx.doi.org/10.1155/2013/959761.

Das T K, A J Chadwadkar, A P Budhkar, A A Belhekar, S Sivasanker. 1995. Studies on the synthesis of ETS-10 I. Influence of synthesis parameters and seed content. *Microporous Materials*, 4: 195-203.

Datsyuk V, M Kalyva, K Papagelis, J Parthenios, D Tasis, A Siokou, I Kallitsis, C Galiotis. 2008. Chemical oxidation of multiwalled carbon nanotubes. *Carbon*, 46: 833-840.

Diagboya P N, B I Olu-Owolabi, D, B-H Han. 2014. Graphene oxide–tripolyphosphate hybrid used as a potent sorbent for cationic dyes. *Carbon*, 79: 174–182.

Dikmen S, A Gunay, B Ersoy, I Erol. 2015. Determination of equilibrium, kinetic and thermodynamic parameters of acid red 88 adsorption onto montmorillonitic clay. *Environmental Engineering and Management Journal (eemj)*, 14.5: 1097-1110.

Dong X C, Y Ma, G Zhu, Y Huang, J Wang, M B Chan-Park, L Wang, W Huang, P Chen. 2012. Synthesis of graphene–carbon nanotube hybrid foam and its use as a novel three-dimensional electrode for electrochemical sensing, *Journal of Materials Chemistry*, 22: 17044-17048.

Ghribi A, M Chlendi. 2011. Modeling of fixed bed adsorption: application to the adsorption of an organic dye. *Asian journal of textile*, 1.4: 161–171.

Haibo O, H Li, L Qi, Z Li, J Wei, J Wei. 2008. Synthesis of a silicon carbide coating on carbon fibers by deposition of a layer of pyrolytic carbon and reacting it with silicon monoxide. *Carbon*, 46: 1339-1344.

Hong S B, S J Kim, Y S Uh. 1996. Vibrational spectroscopic evidence for the presence of TiO_6 structural units in titanosilicate molecular sieve ETS-10. *Korean Journal of Chemical Engineering*, 13: 419-421.

Karpowicz F, J Hearn, M C Wilkinson. 1995. The quantitative use of the Bohart-Adams equation to describe effluent vapour profiles from filter beds. *Carbon*, 33.11: 1573–1583.

Lagergren S. 1898. Zur theorie der sogenannten adsorption gelöster stoffe. *Handlingar*, 24: 1-39.

Langmuir I. 1918. The adsorption of gases on plane surfaces of glass, mica and platinum. *Journal of the American Chemical Society*, 40: 1361–1403.

Liu Y. 2009. Is the free energy change of adsorption correctly calculated? *Journal of Chemical & Engineering Data*, 54.7: 1981–1985.

Lv L, F Y Lee, J Zhou, F Su, X S Zhao. 2006. XPS study on microporous titanosilicate ETS-10 upon acid treatment. *Microporous and Mesoporous Materials*, 96: 270-275.

Mustafa Y A, S E Ebrahim. 2010. Utilization of Thomas model to predict the breakthrough curves for adsorption and ion exchange. *Journal of Engineering*, 16.4 (2010): 6206–6223.

Prasanth K P, M C Raj, H C Bajaj, T H Kim, R V Jasra. 2010. Hydrogen sorption in transition metal modified mesoporous materials, *International Journal of Hydrogen Energy*, 35: 2351–2360.

Robertson J. 2002. Diamond like amorphous carbon. *Materials Science and Engineering R*, 37: 129-281.

Rocha J, A Ferreira, Z Lin, M W Anderson. 1998. Synthesis of microporous titanosilicate ETS-10 from $TiCl_3$ and TiO_2: a comprehensive study. *Microporous and Mesoporous Materials*, 23: 253 – 263.

Ruthven D M. 1984. Principles of Adsorption and Adsorption Processes. Wiley, New York.

Salvestrini S, V Leone, P Iovino, S Canzano, S Capasso. 2014. Considerations about the correct evaluation of sorption thermodynamic parameters from equilibrium isotherms. *Journal of Chemical Thermodynamics*, 68: 310–316.

Scott S M, T Hu, T Yao, G Xin, J Lian. 2015. Graphene-based sorbents for iodine-129 capture and sequestration. *Carbon*, 90: 1-8.

Song G, X Zhu, R Chen, Q Liao, Y-D Ding, L Chen. 2016. An investigation of CO2 adsorption kinetics on porous magnesium oxide. *Chemical Engineering Journal*, 283: 175–183.

Southon P D, R F Howe. 2002. Spectroscopic studies of disorder in the microporous titanosilicate ETS-10. *Chemistry of Materials*, 14: 4209-4218.

Su Y, M L Balmer, B C Bunker 2000. Raman spectroscopic studies of silicotitanates. *Journal of Physical Chemistry B*, 104: 8160-8169.

Thomas H C. 1944. Heterogeneous ion exchange in a flowing system. *Journal of the American Chemical Society*, 66.2: 1664–1666.

Tran H N, S J You, H P Chao. 2016. Thermodynamic parameters of cadmium adsorption onto orange peel calculated from various methods: A comparison study. *Journal of Environmental Chemical Engineering*, 4.3: 2671–2682.

Trinh T T, T S van Erp, D Bedeaux, S Kjelstrup, C A Grande. 2015. A procedure to find thermodynamic equilibrium constants for CO_2 and CH_4 adsorption on activated carbon. *Physical Chemistry Chemical Physics*, 17.12: 8223–8230.

Xu Z, J-G Cai, B-C Pan. 2013. Mathematically modeling fixed-bed adsorption in aqueous systems. *Journal of Zhejiang University-Science A (Applied Physics {&} Engineering)*, 14.3: 155–176.

Yang X, J-L Paillaud, H F W J van Breukelen, H Kessler, E Duprey. 2001. Synthesis of microporous titanosilicate ETS-10 with TiF_4 or TiO_2. *Microporous and Mesoporous Materials*, 46: 1– 11.

Yang X, R E Truitt. 1996. ^{129}Xe NMR investigation of ETS-10 titanosilicate molecular sieves. *Journal of Physical Chemistry*, 100: 3713-3718.

Zhu Y, Y-J Bai, N Lun, Y-X Qi, R Liu, H-L Zhu. 2012. Low temperature preparation of hollow carbon nano-polyhedrons with uniform size, high yield and graphitization. *Materials Chemistry and Physics*, 134: 639-645.

Quad Chart

U.S. DEPARTMENT OF ENERGY
Nuclear Energy

Off-Gas Treatment: Evaluation of Nano-structured Sorbents for Selective Removal of Contaminants

OVERVIEW

Purpose: Present research is aimed at developing an effective adsorption based process for the separation and immobilization of radionuclides from UNF recycling off-gases using nano-structured sorbents. The project scope includes synthesis, characterization, and evaluation of the sorbents with respect to sorption equilibria. Immobilization techniques will also be investigated and process models will be developed for the design of the treatment system.

Objectives:

1. To synthesize and characterize the surface and structure of various nanosorbents for the removal of the radioactive contaminants
2. To determine the adsorption isotherms for contaminants of interest (I, Kr) on selected sorbents
3. To investigate the immobilization of the contaminants in a durable form
4. To develop a process model that can be used for the design of the capture and immobilization system for the radionuclides in the off-gas.

IMPACT

Logical Path: Various sorbents will be synthesized (1) and their surface/structural properties characterized (2). Sorption experiments with single components (3) will be followed by multicomponent sorption (4) and immobilization experiments (5). Information from the experiments will be combined with the system modeling effort (6) leading to the design of the treatment system(7).

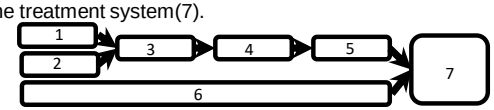

Outcomes: The research will yield information on the sorption characteristics of various materials that can be used for the treatment of radionuclides from the UNF recycling operations. Experiments conducted during the project will provide data on the capture and immobilization of the contaminants. The experiments will also allow us to determine the characteristic values of the parameters in the system models developed in the project. This information will be useful in designing the treatment system, and the development of advanced fuel cycle. The project will also help mentor students who can potentially join the nation's technical nuclear workforce.

DETAILS

Principal Investigator: Vivek Utgikar

Institution: University of Idaho (UI)

Collaborators: D. Eric Aston (UI), Piyush Sabharwall (INL)

Duration: 01/01/2014-12/31/2017 **Total Funding Level:** $625,437

TPOC: Bob Jubin

Federal Manager: Jim Bresee

Workscope: FC-6.5

PICSNE Workpackage #:
NU-13-ID-UI__-0201-05

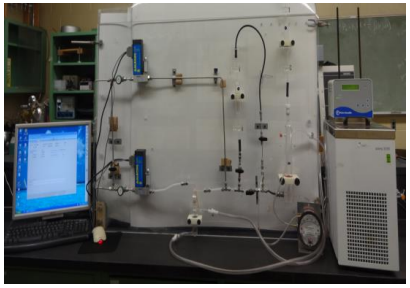

RESULTS

Activities:
1. Engelhard Titanosilicate-10 (ETS-10) supported nanostructured carbon material synthesized for application as the sorbent for capture of Kr and I. 2. Dynamic sorption experiments conducted under varying parameters such as temperature, contact time, compositions, humidity and sorbent composition to obtain experimental sorption data. Virgin and used sorbents characterized using various techniques. 3. Experiments conducted to develop matrix for immobilization and isolation of captured contaminants. 4. Mathematical models developed form quantifying the thermodynamics and kinetics of sorption, and validated on the basis of the experimental data.

Accomplishments:
Refereed Journal Publications: 5
Nandanwar et al, *Chem. Eng. J.*, 2017, 320: 222-231; Nandanwar et al, *Chem. Eng. J.*, 2016, 306: 369-381; Nandanwar et al, *Chem. Eng. J*, 2016, 287: 593-601; Nandanwar et al, *Adsorption*, 2016, 22: 129-137; Nandanwar et al, *Adsorption*, 2016, 22: 335-345.

Presentations at National Meetings of Professional Societies: 9

Personel Mentored:
Post-Doctoral Associate: 1; Graduate Students: 1 (MS Chemical Engineering, graduated); 1 (MS Materials Engineering); Undergraduate Students: 3